

LEABHARLANN CHOLÁISTE NA TRÍONÓIDE, BAILE ÁTHA CLIATH | TRINITY COLLEGE LIBRARY DUBLIN
Ollscoil Átha Cliath | The University of Dublin

Terms and Conditions of Use of Digitised Theses from Trinity College Library Dublin

Copyright statement

All material supplied by Trinity College Library is protected by copyright (under the Copyright and Related Rights Act, 2000 as amended) and other relevant Intellectual Property Rights. By accessing and using a Digitised Thesis from Trinity College Library you acknowledge that all Intellectual Property Rights in any Works supplied are the sole and exclusive property of the copyright and/or other IPR holder. Specific copyright holders may not be explicitly identified. Use of materials from other sources within a thesis should not be construed as a claim over them.

A non-exclusive, non-transferable licence is hereby granted to those using or reproducing, in whole or in part, the material for valid purposes, providing the copyright owners are acknowledged using the normal conventions. Where specific permission to use material is required, this is identified and such permission must be sought from the copyright holder or agency cited.

Liability statement

By using a Digitised Thesis, I accept that Trinity College Dublin bears no legal responsibility for the accuracy, legality or comprehensiveness of materials contained within the thesis, and that Trinity College Dublin accepts no liability for indirect, consequential, or incidental, damages or losses arising from use of the thesis for whatever reason. Information located in a thesis may be subject to specific use constraints, details of which may not be explicitly described. It is the responsibility of potential and actual users to be aware of such constraints and to abide by them. By making use of material from a digitised thesis, you accept these copyright and disclaimer provisions. Where it is brought to the attention of Trinity College Library that there may be a breach of copyright or other restraint, it is the policy to withdraw or take down access to a thesis while the issue is being resolved.

Access Agreement

By using a Digitised Thesis from Trinity College Library you are bound by the following Terms & Conditions. Please read them carefully.

I have read and I understand the following statement: All material supplied via a Digitised Thesis from Trinity College Library is protected by copyright and other intellectual property rights, and duplication or sale of all or part of any of a thesis is not permitted, except that material may be duplicated by you for your research use or for educational purposes in electronic or print form providing the copyright owners are acknowledged using the normal conventions. You must obtain permission for any other use. Electronic or print copies may not be offered, whether for sale or otherwise to anyone. This copy has been supplied on the understanding that it is copyright material and that no quotation from the thesis may be published without proper acknowledgement.

Preparation, characterisation and technological applications of half-metallic ferromagnetic oxides in ceramic and thin film form

by

Rui Pedro Nogueiro Gomes Morais Borges

A thesis submitted for the degree of
Doctor of Philosophy
in the University of Dublin

Department of Physics
Trinity College Dublin

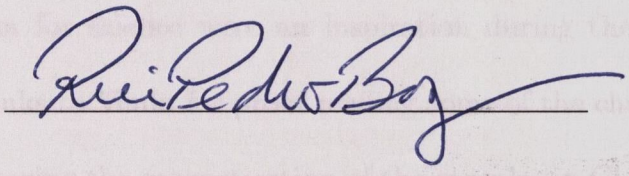
October 2000

DECLARATION

This thesis is submitted by the undersigned for examination for the degree of Doctor of Philosophy at the University of Dublin. It has not been submitted as an exercise for a degree at any other university.

This thesis, apart from the advice, assistance and joint effort mentioned in the acknowledgements and in the text, is entirely my own work.

I agree that the library may lend or copy this thesis freely on request.



ACKNOWLEDGMENTS

Firstly I would like to thank my supervisor Prof. J. M. D. Coey for his guidance and for giving me the opportunity and means to work in his laboratory for the last four years.

During the course of this work I also benefited from the advise and knowledge of James Lunney, Jim Cullen and Vassil Skumriev.

This work would have not been the same without the help of Munuswamy Venkatesan, Frederic Ott and Laurent Ranno. Their patience for my endless questions, dedication and enthusiasm for science were an inspiration during the years of my postgraduate studies. Extra thanks to Venki for proof reading some of the chapters of this thesis and Fred for the help measuring the magnetisation of the samples in Chapter 3.

Thanks to past and present postgrads in the Physics Department who have in some way helped me finishing this thesis,especially Eduardo de Posada, Massimo Cazzanelli, Wiebke Hasch, Nora Dempsey, Juan Castro, Janko Versluijs, Gareth Hinds, Tue Hansen, Jiang Chengbao, Treasa Ní Mhíocháin, Cora O'Reilly, Katie Gallagher, Cian Cullinan, Sandrine Llostis, Laurent Clochard, Mazhar Bari, Donagh O'Mahony, Ciara Fitzgerald and Duncan Cole. The course of my research was made much smoother by the assitance of the technical staff in the Physics Department: Jacqueline Armstrong, Dave Grouse, Gunilla Nordstrom, James Egan, Liz Gray, Jim Cavanagh, Tom Burke, John Kelly, Joe McCauley and Ken Concannon.

Thanks to Michael Besse at Thompson and Ramanathan Suryanarayanan at LPC Orsay for their precious help with the magnetisation measurements of Chapter 4.

A special word of thanks is due to John Gregg and Martin Thornton for welcoming me

at the Clarendon Laboratory, Oxford and for trying so hard to teach me some electronics.

E claro, um obrigado muito especial para toda a minha família por toda a paciência e apoio que me deram durante os últimos quatro anos, pelos telefonemas e as constantes remessas de víveres !

And finally my dear Alison for all the wonderful times and for trying to convince me that this was all worthwhile.

Table of Contents

Summary **7**

1 Introduction **10**

1.1 Spin electronics 10

1.2 Manganese perovskites 15

1.2.1 Structural properties 15

1.2.2 Electronic and magnetic properties 17

1.3 Double perovskites 20

1.3.1 Structural properties 21

1.3.2 Electronic and magnetic properties 22

1.4 Magnetoresistance 23

1.4.1 Intrinsic magnetoresistance 24

1.4.2 Extrinsic magnetoresistance 27

1.5 Pulsed Laser Deposition 31

1.6 Devices 36

References **41**

2 Experimental Methods **43**

2.1 Sample Preparation 43

2.1.1 Ceramics 43

2.1.2 Thin films 43

2.2 Structural characterisation 49

2.2.1 X-ray diffraction 49

2.2.2 Morphology 50

2.3 Transport Properties 51

2.3.1 Resistance versus temperature 51

2.3.2 Magnetoresistance 51

2.4 Magnetic properties 52

2.4.1 Transverse magnetooptic Kerr effect 52

2.4.2 SQUID measurements 53

2.5 Microlithography 53

2.5.1 Mask design 53

2.5.2 Resist spinning 54

2.5.3 Ultra-Violet lithography 54

2.5.4 Ion beam milling 58

References **63**

3 Manganese Perovskites **64**

3.1 Introduction 64

3.2 Film deposition 68
3.3 Search for the optimum deposition conditions 70
3.4 Influence of substrate temperature 76
3.5 Influence of film thickness 83
3.6 Discussion 88

References 95

4 Double Perovskites 97

4.1 Introduction 97
4.2 Study of A_2FeMoO_6 for A = Ca, Sr, Ba 103
4.2.1 Ceramics 103
4.2.2 Thin films 110
4.3 Discussion 128
4.3.1 Bulk ceramics and powders 128
4.3.2 Thin films 133

References 138

5 Devices 140

5.1 Introduction 140
5.1.1 Hall sensors 142
5.1.2 GMR sensors 145
5.1.3 Manganite based devices 145
5.2 A versatile microwave sensor 147
5.2.1 The sensor circuit 148
5.2.2 The control circuit 156
5.3 Results and applications 158
5.3.1 Detection of mechanical parts 161
5.3.2 Discontinuous fluid flow 166
5.3.3 Continuous fluid flow 169
5.4 Discussion 173

References 178

A Proof that $\delta\left(\frac{1}{Q}\right) = \eta\chi'' = \eta\chi''_e$ 179

B Electromagnetic losses in a continuous medium 183

C Tuning the circuit 186

6 Conclusions and further work 187

6.1 Conclusions 187
6.2 Suggestions for further work 191

Summary

The aims of this study were: (i) to study the structural, magnetic and transport properties of ferromagnetic oxides $(La_{0.7}Sr_{0.3})MnO_3$ and A_2FeMoO_6 (A=Ca, Sr, Ba) in polycrystalline and thin film form, (ii) to optimise the physical, magnetic and transport properties of these materials and study the feasibility of their use in the fabrication of electronic devices and (iii) fabricate a device based on one of these materials.

The compound $(La_{0.7}Sr_{0.3})MnO_3$ is half-metallic with the highest Curie temperature (T_C=370 K) of the manganese perovskite series. The first part of the present work deals with thin films of this compound prepared by Pulsed Laser Deposition (PLD). The deposition conditions were optimised by studying the influence of oxygen pressure and substrate temperature on the structural, magnetic and transport properties of the films. It was found that as deposited thin films with T_C greater than 350 K and metallic conduction can be obtained by using a laser fluence of 2 Jcm^{-2}, a background oxygen pressure of 0.3 mbar and a substrate temperature of 680°C. The substrate temperature during deposition plays a major role in determining the microstructure of the films, with deviations from the optimum temperature leading to the formation of granular films. Granular films show a large low field magnetoresistance due to intergrain spin dependent tunneling of electrons which can be useful for device applications such as magnetic field sensors.

Another series of LSMO films of different thicknesses was deposited using the optimal deposition conditions. Film thickness ranges from 1 to 60 nm. It was found that there are electric and magnetic dead layers at the two film interfaces (air and substrate) while the bulk of the film is ferromagnetic and metallic. The electric dead layer has a total thickness of 4 nm and works as a barrier for spin dependent tunnelling across grain boundaries. The magnetic

dead layer has a total thickness of approximately 20 nm and consists of non-colinear spins that are responsible for the disappearence of MR in magnetic tunnel junctions above 150 K. The total thickness of the dead layers is constant and as the total film thickness decreases, there is a decrease in the thickness of the ferromagnetic centre.

Most device applications require operating temperatures in the range -20 to 140°C which has lead to a search for half metallic compounds with a higher Curie temperature than that of LSMO. Among the double perovskite family, some compounds have similar properties to the manganese perovskites and a higher T_C. This has been shown in a recent study by Kobayashi et al. where the double perovskite Sr_2FeMoO_6 is shown to have a T_C=415 K and half-metallic behaviour is predicted from band structure calculations. In the present work, a detailed study of A_2FeMoO_6 (A= Ca, Sr and Ba) compounds is presented. Sr_2FeMoO_6 shows the highest T_C value of 425 K and a magnetoresistance of 1 % at room temperature in 20 mT. The room temperature resistivity of the ceramics varies by more than five orders of magnitude from 1 mΩ cm for Ca_2FeMoO_6 to 4.5×10^5 mΩ cm for Sr_2FeMoO_6. This large variation can be ascribed to the different sample microstructure. Furthermore, all ceramics fail to reach the full saturation magnetisation value of 4 μ_B/f.u at 5 K, which is explained by cation disorder at the B site.

Sr_2FeMoO_6 was chosen as the material for fabrication of thin films due to its high T_C. Thin films deposited on $SrTiO_3$ (100) and MgO (100) substrates by PLD were studied. All film grow with (220) planes parallel to the substrate plane in order to minimise the lattice mismatch. Good quality films can be deposited on $SrTiO_3$ substrates with a saturation magnetisation of 3.5 μ_B/f.u at 20 K. Films deposited on MgO have lower saturation magnetisation ($\sim$2 μ_B/f.u.) and the surface shows the existence of large L shaped holes. Film

deposition in an oxygen atmosphere leads to the formation of a yellow semiconducting phase consisting mainly of $SrMoO_4$.

In Chapter 5, a device for position and motion sensing is described. The device was designed to combine microwave electronics and a ferromagnetic oxide for enhanced sensitivity. The operation is based on the change in susceptibility of a ferromagnetic oxide (LSMO) which in turn changes the quality factor of a coil when in the presence of an object. Two designs were developed, one using a multiturn coil filled with LSMO (by Thornton et al. at Oxford University) and the other, presented in this study, using a thin film of LSMO where a single turn coil is patterned. Single turn coils of permalloy and copper were also prepared and tested. While in the multiturn coil device there is a significant enhancement of the signal when the coil is filled with LSMO, in the single turn device there is no visible improvement when the LSMO coil is used due to the small amount of ferromagnetic material used in the coil ($\sim 10^{-7}$ g). However, the virtues of the electronics are enough to make this device a very attractive new concept in sensor applications.

The detection dependence on the magnetic and electric susceptibility makes the device very versatile and it is shown that it can detect a variety of materials. Here we show the signal output when monitoring the angular velocity and position of mild steel and plastic gearwheels. The device is also able to detect liquids and the signal output for a variety of liquids including water, solvents, milk and blood is shown. Two patents have been filed covering different aspects of device applications.

Chapter 1

Introduction

1.1 Spin electronics

Probably no other branch of science and technology could claim to have the same influence in shaping modern daily life as electronics. Thousands of routine operations are based on devices whose working depends on controling in some way the flow of electrons by acting on their charge with an electric field. Until very recently, electronic devices that make use of magnetic fields have been restricted to Hall sensors, solenoids and relays. Silicon based electronics only takes account of the charge of the electron making no practical use of the fact that the electrons possess a magnetic moment; some are spin up and others spin down. The recognition of this distinction can lead to a whole new generation of electronic devices whose operation relies on the manipulation of different families of current carriers with opposite spin polarisation [1] [2] [3]. This growing area of scientific and technological research has been called spin electronics. Its theoretical basis lies on Mott's finding that electric conduction in a ferromagnet may be modelled by assuming that the current is carried in two distinct channels (Figure 1.1b), one consisting of the electrons with spin parallel to the magnetisation and the other with spins antiparallel [32]. The independence of the two channels is not complete, electrons can be moved between the two channels by spin flip processes. This two channel model has been experimentally confirmed [5] [6] by measurements of electrical transport on selectively doped ferromagnets. The experiment reveals that electrons of one spin orientation are more heavily scattered than the others.

The idea of making use of the spin of the electron for practical applications is not a new

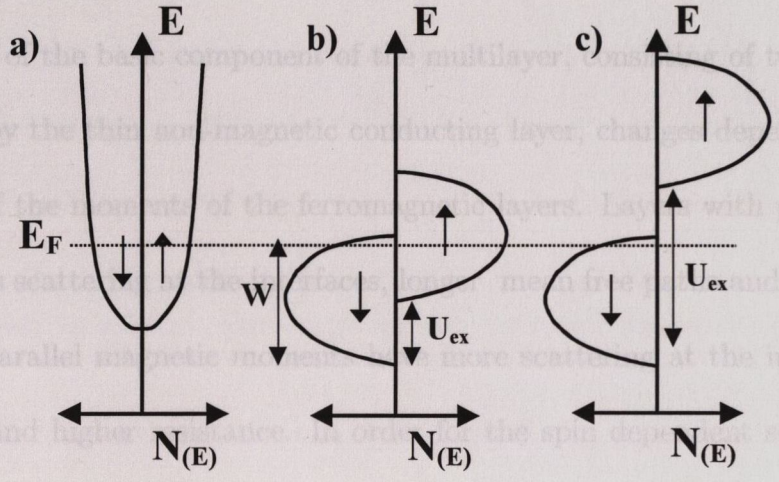


Figure 1.1. Schematic band structure of: a) non magnetic metal; b) ferromagnetic metal with U_{ex}<W; c) half-metallic ferromagnet with U_{ex}>W. W is the bandwidth and U_{ex}, the on-site Hund's exchange interaction which is the energy required to flip a d-electron spin.

one. Meservey et al [7] were the first to produce a spin polarized current using a $Al/Al_2O_3/Ni$ tunnel junction at low temperatures when the Al film is in the superconducting state. The process depends on the fact that for thin superconducting Al films, the quasi-particle density of states is split by a magnetic field into spin-up and spin-down parts. The resulting densities of states are similar but displaced by $\pm\mu_0 mH$, where m is the magnetic moment of the electron. This displacement allows electrons of either spin direction to be selected from the electrons tunnelling from the ferromagnetic electrode.

The breakthrough for spin electronics arrived with the measurement of the first magnetic field dependent change in the resistance of metallic multilayers of Fe/Cr in 1988 [8]. The effect was named giant magnetoresistance (GMR). The authors found that when the thickness of the non-magnetic Cr layers is decreased below 20 Å, the Fe layers are coupled antiferromagnetically. As the applied magnetic field increases, the magnetisation of the Fe layers gets progressively more aligned and the resistance of the structure decreases. GMR multi-

layers with around 30 Fe/Cr layers showed changes of resistance of up to 50% at 4.2 K in a magnetic field of 2 Tesla. The value decreases with increasing temperature to 20% at 300 K. The resistance of the basic component of the multilayer, consisting of two ferromagnetic layers separated by the thin non-magnetic conducting layer, changes depending on the relative alignment of the moments of the ferromagnetic layers. Layers with parallel magnetic moments have less scattering at the interfaces, longer mean free paths and lower resistance. Layers with antiparallel magnetic moments have more scattering at the interfaces, shorter mean free paths and higher resistance. In order for the spin dependent scattering to be a significant part of the total resistance, the layers must be thinner than the spin diffusion length (the average distance travelled by a carrier spin before flipping) of electrons in the bulk material. The magnetoresistance of metallic multilayers is measured in a current in plane (CIP) configuration.

The behaviour of this giant magnetoresistor illustrates an important point: spin electronic devices operate by transferring spin information from one part of the device to another. The information is mediated by the charge carriers and it decays on a characteristic length scale (spin diffusion length). An essential criterion for the creation of spin electronics is therefore, the ability to engineer structures whose physical dimensions are of this order of magnitude. GMR technology is now available commercially in a variety of magnetic field and motion sensors [3] [9]. The introduction of GMR in hard-disk read-write heads by IBM in 1997 shows the huge potential of this kind of technology. The new GMR heads are two to three times more sensitive than their predecessors, the magnetoresistive heads based on anisotropic magnetoresistance, allowing for a larger data storage density in the hard drive ($\sim$ 100 Gb per square inch) [10]. This type of device could also be very important where information storage

is concerned given that it would allow the fabrication of non-volatile memory elements where the information could remain stored without the presence of an electrical current.

In 1993 von Helmholt et al [11] used Pulsed Laser Deposition (PLD) to grow thin films of the manganese perovskite $(La_{2/3}Ba_{1/3})MnO_3$ showing a very large change in resistance near the Curie temperature (T_C). The effect has been since called Colossal Magnetoresistance (CMR). A larger, extrinsic magnetoresistance can be obtained if the material is in polycrystalline form due to transport across grain boundaries. The discovery of CMR in manganites triggered a search for the composition and stoichiometry that gives rise to the higher value of T_C and magnetoresistance. More important than CMR from the point of view of device fabrication is the fact that these materials conduct a fully polarised current, i.e., all the conduction electrons have the same spin (see Figure 1.1). These materials are referred to as half metals.

New perspectives arise in spin physics and devices with the ability to manipulate conduction in two independent spin channels. In this respect, the magnetic tunnel junctions (MTJ) are the most researched type of device using half metallic materials. The idea is similar to that of GMR multilayers with the device consisting of only three layers: a non magnetic insulator sandwiched between two half metallic electrodes with different sizes and therefore different coercive fields. When the magnetisations of the two layers are parallel, there will be states available for the polarized electrons on the conduction bands of both electrodes and tunnelling can occur. In this case, the device is in its low resistance configuration. When a small applied field switches the magnetisation of one of the electrodes, the polarized electrons will not find available states and therefore the tunnelling process becomes more difficult. This corresponds to a high resistance configuration. Values as high

as 450 % magnetoresistance have been measured at low temperatures in devices made of $(La_{0.7}Sr_{0.3})MnO_3/SrTiO_3/(La_{0.7}Sr_{0.3})MnO_3$ [6].

Much interest is also focused on three terminal devices after the fabrication of a metal base transistor by Monsma et al [14] which uses a metallic GMR multilayer as the base. This multilayer is sandwitched between two silicon layers (emitter and collector) forming two Schottky barriers. Changing the magnetic configuration of the base multilayer changes the mean free path of the electrons and, hence the fraction of the emitter current that reaches the collector. Another three terminal device is a superconducting transistor consisting of a trilayer of $(La_{0.7}Sr_{0.3})MnO_3/La_2CuO_4/DyBa_2Cu_3O_7$ [15]. The critical current of the superconductor seems to be greatly reduced by injection of a spin polarised current, allowing the control of the current flowing in the superconducting strip with a small polarised current injected from the manganite.

The exploitation of spin polarised currents represents not only a departure for the fields of magnetism and magnetic materials but also a new direction for electronics. The ability to make increasingly smaller structures incorporating dissimilar materials is the base for this new area of research. With the development of half metallic materials exhibiting 100 % polarised currents (Figure 1.1 c)) such as $(La_{0.7}Sr_{0.3})MnO_3$, CrO_2 [16] and and Sr_2FeMoO_6 [10], many of the existing electronic devices could be replaced with much smaller, more robust devices that have the advantage of possessing intrinsic memory. These devices should allow true ON/OFF operation with an essentially infinite ratio of impedance between the two states due to the 100% spin polarised currents. There are also other applications such as robotics and precision engineering where fast and accurate position and motion sensing of mechanical components is required. In particular there is a growing need of such technology

in the development of improved fuel handling systems and electronic engine control in the automotive industry [1] in order to decrease environmental damage by fuel emissions.

1.2 Manganese perovskites

Mixed valence manganites with the perovskite structure have been studied for the last 50 years [18]. The complexity of these materials was early revealed, with a strong dependence of the magnetic and transport properties on chemical composition, stoichiometry and preparation procedure [19] [20][21]. They show very large variations of resistivity with applied magnetic field near T_C which makes them attractive for possible device fabrication. A detailed description of their structural, electronic and magnetic properties is given in the following sections.

1.2.1 Structural properties

The perovskite $CaTiO_3$ has body centred cubic lattice with $a = 3.88$ Å. Ca occupies the A site and Ti the B site of the perovskite unit cell. The structure can be regarded as a cubic close packed array formed of O^{2-} anions and A cations, with the small B cations occupying the octahedral interstitial sites [18]. In the case of the manganese perovskites studied in this work the B site is occupied by a manganese atom while the A site can be occupied by either a rare earth of valence 3^+ or an alkaline earth metal of valence 2^+ (Figure 1.2). The manganese compounds often have an orthorhombically or rhombohedrally distorted version of the basic structure with a larger unit cell. Compounds with this type of structure are generally called perovskites.

For example, $LaMnO_3$ has an orthorhombic structure related to the cubic perovskite structure. This kind of material can be doped with a divalent ion like Ca^{2+} leading to

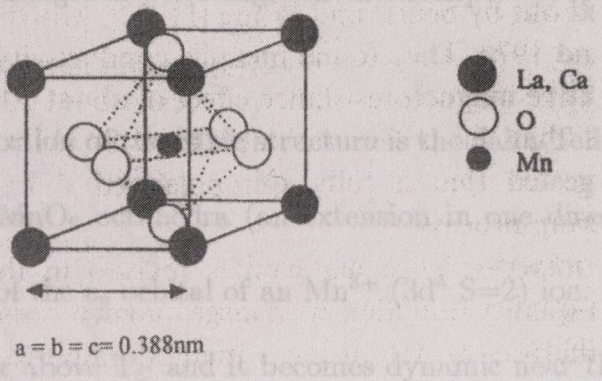


Figure 1.2. The manganese perovskite unit cell.

compounds with general formula

$$R_{1-x}A_xMnO_3 \tag{1}$$

where R is a rare-earth ion such as La, Pr, Nd, Sm, Eu, Gd, Ho, Tb or Y and A is an alkaline earth ion such as Sr, Ca or Ba. Interestingly, the different possible combinations of composition and stoichiometry can lead to a wide variety of crystal structures such as tetragonal, rhombohedral, hexagonal, orthorhombic and monoclinic[18][22][23].

One source of such lattice distortion is the cation size mismatch. Such a distortion is governed by a tolerance factor f [24] defined as

$$f = \frac{r_A + r_O}{\sqrt{2}(r_B + r_O)}. \tag{2}$$

where r_A, r_B and r_O are the radii of the A site, B site and oxygen ions respectively. The tolerance factor measures the lattice mismatch between adjacent AB and BO_2 planes. When f is close to 1 a cubic structure is obtained. As f decreases (by decreasing r_A or increasing r_B) the structure becomes rhombohedral as in $(La_{0.7}Ba_{0.3})MnO_3$ ($0.96<f<1$) and then orthorhombic ($f<0.96$) for compounds such as $(Pr_{0.7}Ca_{0.3})MnO_3$ and $(Sm_{0.7}Sr_{0.3})MnO_3$ [32] [22]. Deviations from the cubic structure correspond to a change in the Mn-O-Mn bond angle

from 180°. The effect of changes in bond angle on the transport properties will be discussed in section 1.2.2.

Another source of distortion of the cubic structure is the Jahn-Teller effect. This consists of a deformation of the MnO_6 octahedra (an extension in one direction in the *ab* plane) giving rise to a splitting of the e_g orbital of an Mn^{3+} ($3d^4$ S=2) ion. The Jahn-Teller effect is static for low doping or above T_C and it becomes dynamic near the Curie point of solid solutions with $0.2<x<0.5$ [18].

1.2.2 Electronic and magnetic properties

Manganese perovskites such as $LaMnO_3$ and $CaMnO_3$ are antiferromagnetic insulators with valence states $La^{3+}Mn^{3+}O_3^{2-}$ and $Ca^{2+}Mn^{4+}O_3^{2-}$ respectively. The solid solutions of these compounds lead to the formation of mixed-valence oxides with valence states given by

$$R_{1-x}^{3+}A_x^{2+}Mn_{1-x}^{3+}Mn_x^{4+}O_3^{2-} \tag{3}$$

where R is a rare-earth and A an alkaline earth metal. The interesting observation is that there are two types of magnetic ion, Mn^{3+} and Mn^{4+}, with electronic configurations $3d^4$ and $3d^3$ respectively. Each Mn ion is surrounded by an oxygen octhedra. In the Mn^{4+} ($3d^3$) ion, the electrons are in the low energy t_{2g} orbitals forming the S=3/2 local spins (Figure 1.3). For the Mn^{3+} ($3d^4$) ion, the extra electron is located in the higher energy e_g orbitals. The t_{2g} and e_g orbitals are split by the local crystal field ($\Delta_{CF} \sim 2$ eV) as shown in Figure 1.3. Extra orbital splitting occurs at the e_g orbitals due to the Jahn-Teller effect. This consists of an extension of the oxygen octahedra in the ab plane leading to a lowering of the energy ($\delta_{JT} \sim 0.5$ eV) of the $d_{x^2-y^2}$ orbital relative to the d_{z^2} orbital. The e_g orbital is strongly hybridized with the oxygen 2p orbitals allowing for a high mobility of the electron.

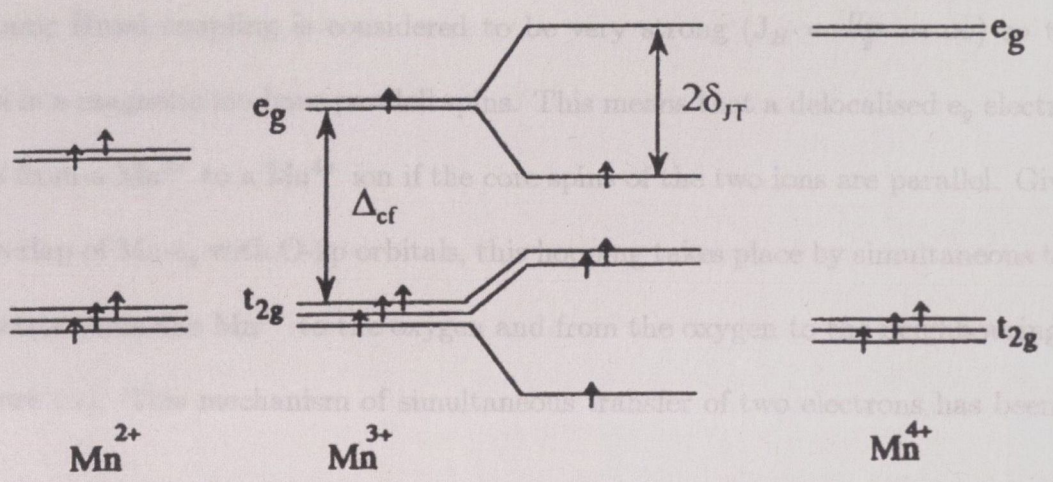


Figure 1.3. The energy levels of the different manganese ions in octahedral coordination.

For values of $x \approx 0.3$ in expression (3) the material becomes a ferromagnetic metal below T_C. For $T>T_C$ a paramagnetic insulating behaviour is observed. An early study on $(La_{0.8}Sr_{0.2})MnO_3$ found that there is a substantial decrease in the resistance near T_C under a magnetic field of 0.3 Tesla [26]. This negative magnetoresistance has since been observed in all compounds in the ferromagnetic range ($0.1 \leqslant x \leqslant 0.5$) and has been termed colossal magnetoresistance (CMR) to distinguish it from the giant magnetoresistance observed in multilayer or granular systems.

Jonker and van Santen in a study of $(La_{1-x}A_x)MnO_3$ with A=Ca, Ba, Sr and $0<x<0.9$ [19] found that for $x \approx 0.3$ the saturation magnetisation of the material approaches the spin only moment of $(4\text{-}x)\mu_B$. This suggests that all the electrons in the material, including the conduction electrons, have parallel spins, further reinforcing the idea of a coupling between transport and magnetism.

An explanation of the simultaneous occurrence of ferromagnetism and metallicity as well

as the CMR effect near T_C has been provided by Zener in 1952 [12]. In this model, the intra-atomic Hund coupling is considered to be very strong ($J_H = \frac{U_{ex}}{2} \sim \infty$) so that all electrons in a magnetic ion have paralell spins. This means that a delocalised e_g electron can only hop from a Mn^{3+} to a Mn^{4+} ion if the core spins of the two ions are parallel. Given the direct overlap of Mn-e_g with O-2p orbitals, this hopping takes place by simultaneous transfer of an electron from the Mn^{3+} to the oxygen and from the oxygen to the neighbouring Mn^{4+} ion (Figure 1.4). This mechanism of simultaneous transfer of two electrons has been called

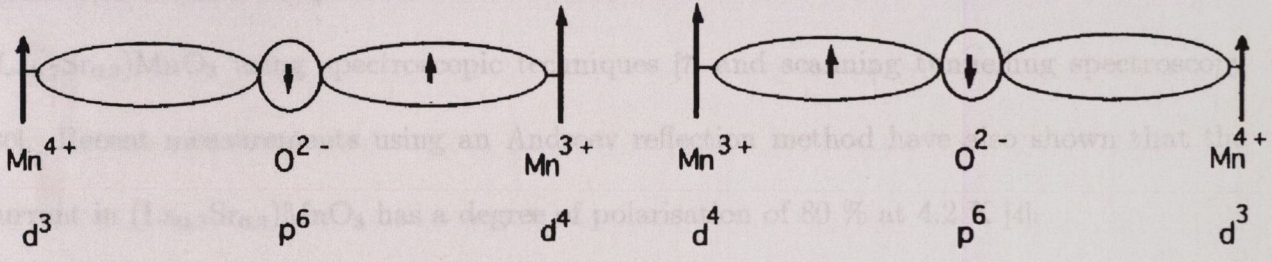


Figure 1.4.The simultaneous transfer of electrons from Mn^{3+} to O^{2-} and from O^{2-} to Mn^{4+}.

Double-Exchange (DE). It is clear from this that the conductivity of the material is strongly dependent on the relative orientation of the core spins. Considering the case of the interaction of two magnetic ions with general spin directions, Anderson and Hasegawa [27] obtained the expression

$$t = t_0 \cos\left(\frac{\theta}{2}\right) \tag{4}$$

for the transfer integral. Here t_0 is the normal transfer integral depending on the spatial wavefunctions and θ is the angle between the two spin directions. This transfer is maximized when the local spins have parallel alignment. It also determines the d electron bandwidth W. The conductivity can be decreased by magnetic disorder or by a tilting of the Mn-O-Mn bond caused by cation size mismatch. Furthermore, in this model, the mobile electrons are

responsible for both conduction and mediators of ferromagnetic exchange. However, double-exchange alone does not explain the magnitude of the CMR observed near T_C [28] and a model has been proposed that couples the transport with lattice distortions through the Jahn-Teller distortion.

The d-d exchange gives rise to a conduction band with a large split between spin-up ($e_g^{\uparrow}$)and spin-down ($e_g^{\downarrow}$)bands as shown schematicaly in Figure 1.1c). Materials with this kind of band structure where the mobile electrons have only one spin direction are called half-metals. Experimental evidence for such band structure has been found for $(La_{0.7}Sr_{0.3})MnO_3$ using spectroscopic techniques [7] and scanning tunnelling spectroscopy [30]. Recent measurements using an Andreev reflection method have also shown that the current in $(La_{0.7}Sr_{0.3})MnO_3$ has a degree of polarisation of 80 % at 4.2 K [4].

In conclusion $(La_{0.7}Sr_{0.3})MnO_3$ (LSMO), with the highest T_C of the manganite series (370 K) and a high degree of spin polarisation, is the most suitable material of the manganite series for use as a source or filter of spin polarised electrons.

1.3 Double perovskites

Much of the interest in double perovskites arises from the prospects of finding half-metallic oxides with higher Curie temperatures. It is well established that Curie temperature of mixed-valence manganites of the type $(R_{1-x}A_x)MnO_3$ cannot be increased above 400 K by any manipulation of the composition or stoichiometry. The Curie temperature of CrO_2, another half-metal, is also 400 K. Substantially higher Curie temperatures are required if devices which rely on spin-polarized transport in half-metallic oxides are to operate in a useful temperature range around room temperature.

1.3.1 Structural properties

Double perovskites, of general formula

$$A_2B'B''O_6 \tag{5}$$

where A is an alkaline-earth or rare-earth (Ca, Sr, Ba) and B' and B" are occupied by different transition metals (Fe, Cr, Mo), have been studied for the last 30 years. Early studies established the crystal structure and magnetic properties of these materials with a large variety of properties found for different compositions and stoichiometries [7] [6]. These compounds have a unit cell which is double the perovskite cell in the three space directions as ilustrated in Figure 1.5 for the case of Ba_2FeMoO_6 which has the ideal structure. For other compounds the cell can be slightly distorted from cubic simmetry. The unit cell of Sr_2FeMoO_6 is tetragonal with a=b=5.573 Å and c=7.905 Å.

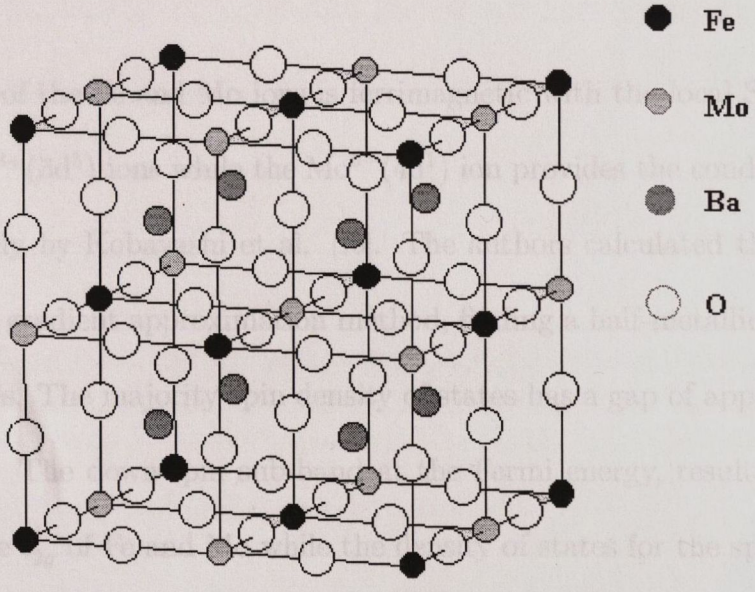


Figure 1.5. The unit cell of the double perovskite Ba_2FeMoO_6.

Many physical and magnetic properties of the double perovskites are greatly influenced

by the B site cation and therefore they are classified according to the B-cation sublattice arrangement. There are three possible arrangements: random, layered and rocksalt. For the random structure there is no ordering of the B-site cations. For the layered structure the different B-site ions arrange themselves into planes while in the rock salt structure the different ions occupy alternate B-site positions. The compounds studied in the present work, Sr_2FeMoO_6, Ca_2FeMoO_6 and Ba_2FeMoO_6 all have the rocksalt superstructure.

1.3.2 Electronic and magnetic properties

For compound with the form A_2FeMoO_6 and A=Ca, Sr or Ba, the formal valences are given by

$$A_2^{2+}Fe^{3+}Mo^{5+}O_6^{2-} \tag{6}$$

as shown by different authors through Mössbauer [6] [34] and polarised neutron diffraction measurements [35].

The alignement of the Fe and Mo ions is ferrimagnetic with the local S=5/2 spins being provided by the $Fe^{3+}(3d^5)$ ions while the $Mo^{5+}(4d^1)$ ion provides the conduction electron as suggested in a study by Kobayashi et al. [10]. The authors calculated the band structure using a generalised gradient approximation method, finding a half-metallic configuration for the density of states. The majority spin density of states has a gap of approximately 0.8 eV at the Fermi level. The down-spin sub-band at the Fermi energy, results from the strong hybridization of the $t_{2g}^{\downarrow}$ of Fe and Mo while the density of states for the spin-up sub-band is zero. The local up spins are in the low energy Fe $t_{2g}^{\uparrow}$ orbitals (strongly hybridized with the O-2p orbitals) plus a Fe $e_g^{\uparrow}$ orbital just below the Fermi energy. A more detailed calculation by Sarma et al. [36] also based on the GGA method obtained essentialy the same results.

The authors observed a significant mixing between the Fe $t_{2g}^{\downarrow}$ and Mo $t_{2g}^{\downarrow}$ bands with some small admixture of oxygen p states.

Like in the double-exchange model, the mobile electron is both responsible for conduction and is the mediator of magnetic exchange. However, in the double perovskites the conduction electron has its spin antiparallel to the local moments.

The theoretical value of magnetisation resulting from the ferrimagnetic exchange is $4\mu_B$/ f. u., but this value is rarely achieved in ceramic materials [26]. This has been explained as the effect of B-site disorder (or anti-site defects), local misplacements of the B-site ions that hinder the ferrimagnetic exchange [34]. The presence of antiphase boundaries has also been suggested to explain the low magnetisation values [38] [27]. The interest in these materials comes from a combination of half metallicity with values of Curie temperature above the limit of 400 K found in LSMO and CrO_2 (e.g. T_C=425K for Sr_2FeMoO_6 [14]). This could open the way for effective room temperature devices and has lead to a surge of interest in these materials by many groups who studied the manganese perovskites over the last number of years.

1.4 Magnetoresistance

Off all transport and magnetotransport properties, magnetoresistance is the most important for device applications. Magnetoresistance is the change in resistance of a given material under an applied magnetic field and is normally defined as

$$MR = \frac{R(H) - R(0)}{R(0)} \times 100\% \tag{7}$$

where $R(H)$ is the value of resistance under a magnetic field H and $R(0)$ is the value of resistance in zero field. Magnetoresistance is positive if the resistance of the material increases

with applied field and negative if it decreases. Much effort has been spent, particularly for oxides, trying to understand the mechanisms that give rise to magnetoresistance [41][18]. It is now accepted that the low field magnetoresistance observed in ceramic materials is due to intergrain transport and therefore, an extrinsic contribution to the measured magnetoresistance. Another example of the interplay between intrinsic and extrinsic effects arises from a practical application of MR: the oxide magnetic tunnel junction. To obtain a value of 10% MR in a colossal magnetoresistive film (e.g. $(La_{0.7}Sr_{0.3})MnO_3$) a field of the order of 5 Tesla is required, which represents a serious drawback where technological applications are concerned. However, by using these films in a tunnel junction one can make use of the half metallic properties to obtain large values of magnetoresistance in fields of the order of 1 mT. This effect has so far been observed below 150 K, and its absence at room temperature is due to the same magnetic disorder at the film interfaces found in grain boundaries. A detailed discussion of this topic will be presented in Chapter 3.

The different magnetoresistance effects are shown in Figure 1.6 [41] and discussed below.

1.4.1 Intrinsic magnetoresistance

1.4.1.1 Classical magnetoresistance

Ordinary magnetoresistance, an increase in the resistance of non-magnetic metals, has its origin on the Lorentz force ($\vec{F} = -e\vec{v} \times \vec{B}$) that acts on the electrons as a result of the applied magnetic field. This effect can be seen in most metals (e.g. copper, silver and gold [43]) except if the magnetic field is applied in the direction of the current. The carriers move in cyclotron orbits where $\omega_c\tau$ is the angle travelled between colisions. $\omega_c = eB/m^*$ is the cyclotron frequency and τ is the scattering time [43]. The carriers make an increasing number of turns with increasing field which reduces their mean free path and therefore

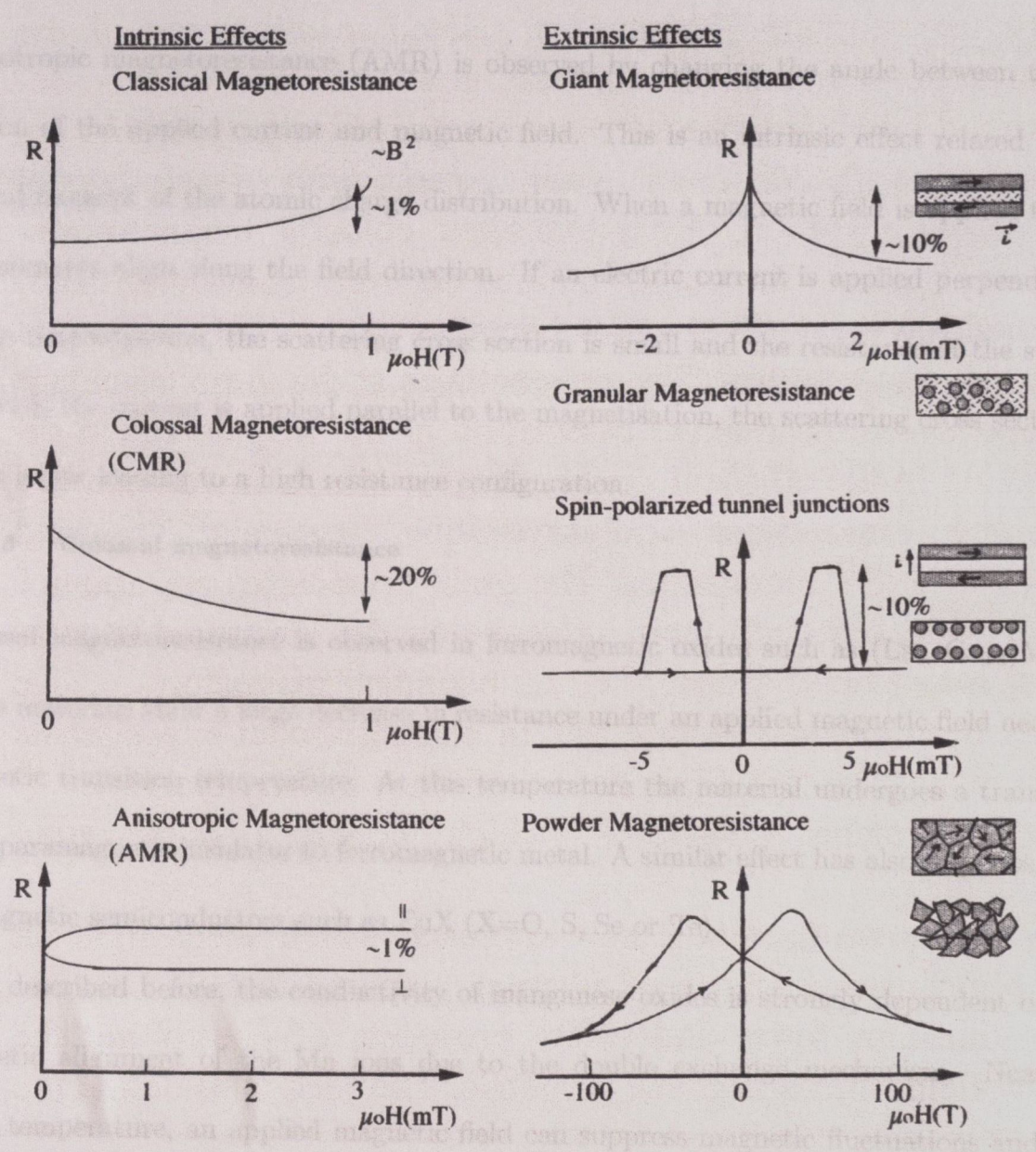


Figure 1.6.The different magnetoresistance effects.

increase the resistance. This increase in resistance is proportional to B^2, which can be obtained theoretically by solving the Boltzman equation.

1.4.1.2 Anisotropic magnetoresistance

Anisotropic magnetoresistance (AMR) is observed by changing the angle between the direction of the applied current and magnetic field. This is an intrinsic effect related to the orbital moment of the atomic charge distribution. When a magnetic field is applied the local moments align along the field direction. If an electric current is applied perpendicular to the magnetisation, the scattering cross section is small and the resistance of the system is low. If the current is applied parallel to the magnetisation, the scattering cross section is much larger leading to a high resistance configuration.

1.4.1.3 Colossal magnetoresistance

Colossal magnetoresistance is observed in ferromagnetic oxides such as $(La_{0.7}Ca_{0.3})MnO_3$. These materials show a large decrease in resistance under an applied magnetic field near the magnetic transition temperature. At this temperature the material undergoes a transition from paramagnetic insulator to ferromagnetic metal. A similar effect has also been observed in magnetic semiconductors such as EuX (X=O, S, Se or Te).

As described before, the conductivity of manganese oxides is strongly dependent on the magnetic alignment of the Mn ions due to the double exchange mechanism. Near the Curie temperature, an applied magnetic field can suppress magnetic fluctuations and give rise to a negative magnetoresistance. CMR is best measured in single crystal or epitaxial thin films where extrinsic contributions are minimized, and is only observed in a narrow range of temperatures near T_C. A decrease of two orders of magnitude in the resistance of $(Nd_{0.5}Pb_{0.5})MnO_3$ near T_C=180 K has been observed but under a field of 11 T [44]. From

the point of view of device applications, it is desirable to have materials with T_C above room temperature. The only compounds of the manganite series that satisfy this condition are $(La_{0.7}Ba_{0.3})MnO_3$ with T_C=330 K and $(La_{0.7}Sr_{0.3})MnO_3$ with T_C=370 K. However these temperatures are still not high enough given that most device applications require working temperatures between -40°C and 120°C.

Double perovskites are a class of materials that could be considered as part of the CMR family. Although the coupling between the magnetic ions is by ↓ electrons, the transport seems to be dependent on the relative orientation of the moments of these ions. Maignan et al [17] have measured the magnetoresistance of Ba_2FeMoO_6 as a function of temperature and observed the same features found in the manganese perovskites, namely a peak around the Curie temperature and an increase in the MR ratio at low temperatures due to intergrain spin dependent tunnelling.

1.4.2 Extrinsic magnetoresistance

1.4.2.1 Giant magnetoresistance

Giant magnetoresistance (GMR) is an extrinsic effect that occurs on metallic multilayers of alternate magnetic and non magnetic layers such as n(Cr/Fe) [8] [46]. The thickness of the non magnetic layers is chosen so that the ferromagnetic layers are coupled antiferromagnetically. The application of a magnetic field aligns the magnetisation of these layers reducing the resistance of the system.

The same effect can be observed in granular alloy systems such as Co-Ag, Fe-Ag, Fe-Cu and Fe-Au [47] by alignement of randomly oriented ferromagnetic spins in a metallic matrix. In order for the spin dependent scattering to be a significant part of the total resistance, the layers must be thinner than the spin diffusion length of electrons in the bulk material. This

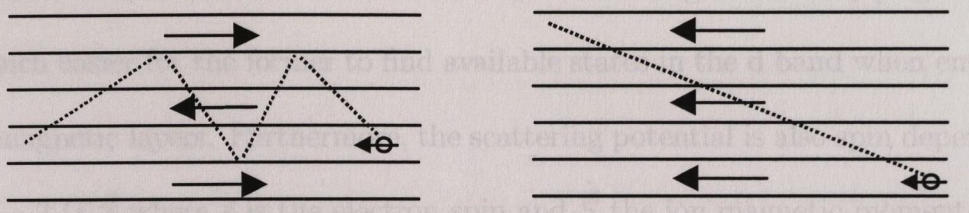


Figure 1.7. Spin dependent scattering in a giant magnetoresistance multilayer for antiparallel and parallel alignement of the moments in the ferromagnetic layers.

can be understood if the problem of spin diffusion is approached as a random walk problem [1]. The lateral displacement of the spin, the spin diffusion length, is given by

$$l_{SD} = \sqrt{N}\lambda \tag{8}$$

where N is the number of momentum scattering events and λ the mean free path. The total path travelled by the spin before flipping is

$$N\lambda = v_F \tau_{\uparrow\downarrow} \tag{9}$$

where v_F is the Fermi velocity and $\tau_{\uparrow\downarrow}$ is the spin relaxation time. Therefore, the spin diffusion length is given by

$$l_{SD} = \sqrt{\lambda v_F \tau_{\uparrow\downarrow}} \tag{10}$$

Equation (10) suggests that the efficiency of the GMR multilayer can be increased by using non-magnetic materials having large λ. Alternatively, the efficiency may also be improved by reducing the thickness of the non-magnetic layers so that the electrons travel between two electrodes without loosing spin information.

The change in resistance is attributed to the conduction of electrons in two separate spin channels resulting in spin dependent scattering. Electrons with spin parallel to the magnetisation ($\uparrow$) have larger mean free paths than those with spin antiparallel ($\downarrow$). The

density of states at the Fermi level for ↑ d electrons is much larger that for ↓ (Figure 1.1). It is therefore much easier for the former to find available states in the d band when entering one of the ferromagnetic layers. Furthermore, the scattering potential is also spin dependent and given by $V - 2J\vec{s}.\vec{S}$ where $\vec{s}$ is the electron spin and $\vec{S}$ the ion magnetic moment [47]. This scattering potential is minimised or maximised depending on whether $\vec{s}$ and $\vec{S}$ are parallel or antiparallel.

In conclusion, the magnitude GMR could be improved by introducing magnetic materials with high spin polarisation. In particular, the use of half-metallic ferromagnets like manganese perovskites, where one can expect the current to be effectively blocked for antiparallel spin alignement, should produce very high magnetoresistance effects.

1.4.2.2 Tunneling magnetoresistance

Tunneling magnetoresistance (TMR) refers to the tunneling of a spin polarised current between two ferromagnetic electrodes separated by a thin insulating layer. The insulating layer should be thick enough to allow magnetic decoupling of the ferromagnetic layers. The two electrodes should also have different sizes so that their magnetisation can switch at different coercive fields. Tunneling magnetoresistance is also obtained in magnetic grains imbedded in an insulating matrix.

The basic theory for TMR effect was introduced by Julière [48] by extending the theory of Meservey and Tedrow [7] to the case of tunneling between two ferromagnetic metals. The conductance of each spin channel is proportional to the product of the densities of states of that channel in both electrodes and is written as

$$G_{\uparrow\uparrow} \propto aa' + (1-a)(1-a') \tag{11}$$

when the magnetisation of the two electrodes is parallel, and

$$G_{\uparrow\downarrow} \propto a(1-a') + a'(1-a) \tag{12a}$$

for antiparallel magnetisation. In this notation a and a' are the fraction of spins parallel to the magnetisation in each magnetic layer and are given by $a = \frac{n_\uparrow}{n_\uparrow + n_\downarrow}$ where $n_\uparrow$ is the number of electrons in the conduction band with spin parallel to the magnetisation and $n_\uparrow + n_\downarrow$ is the total number of electrons in the conduction band. If the electrodes are made of the same material $a = a'$. The change in conductance with magnetic field is $\frac{\Delta G}{G} = \frac{G_{\uparrow\uparrow} - G_{\uparrow\downarrow}}{G_{\uparrow\uparrow}} = \frac{2PP'}{1+2PP'}$. P and P' represent the polarisation of the current in each magnetic layer and where $P = \frac{n_\uparrow - n_\downarrow}{n_\uparrow + n_\downarrow} = 2a - 1$. The value of polarisation can be easily calculated from this expressions once the conductance (or resistance) of the junction is measured as a function of the applied magnetic field.

It is obvious from the equations (11) and (12a) that the highest values of tunneling magnetoresistance are expected for materials with a high spin polarisation. Previous studies concentrated on Ni, Fe and Co electrodes finding values of 11%, 44% and 34% respectively for the current polarisation [49]. Manganese perovskites, with their strongly polarised currents are thought to significantly improve the performance of magnetic tunnel junctions. In recent years some groups have presented results on all-oxide magnetic tunnel junctions such as the LSMO/STO/LSMO structure by Lu et al [6] with a TMR value of 83 % (P=54%) at 4.2 K. Viret et al [6] have reported the highest value so far for an LSMO/STO/LSMO junction with 450% TMR obtained at 4.2 K in a field of 5 mT. This corresponds to a current polarisation of 83% which is in good agreement with the Andreev reflection value of 80 % presented by Soulen et al [4]. However, no manganite based tunnel junction shows a TMR effect above 200 K. This is possibly due to the existence of non-colinear spins on the surface layers of the

LSMO films which decrease the current polarisation and destroy the magnetoresistance.

1.4.2.3 Powder magnetoresistance

Powder magnetoresistance (PMR) is seen in cold pressed powders of materials such as $(La_{0.7}Sr_{0.3})MnO_3$, CrO_2 [41] and Sr_2FeMoO_6 [14]. This phenomenon is essentially similar to tunneling magnetoresistance although there is no exchange coupling between the different particles. The typical MR butterfly loops obtained in powders ressemble those of tunnel junctions although with much broader peaks. This could be due to the distribution of particle sizes, and therefore coercivities, in the ceramic powders.

1.5 Pulsed Laser Deposition

The fabrication of thin films is of paramount importance in order to produce devices that can be incorporated in electronic circuits as well as obtaining a material with well controlled characteristics. Pulsed laser deposition (PLD) is a very versatile research tool that allows for fast and reliable production of thin films of various materials. The concept of PLD is a simple one. It consists of the use of high power lasers to vaporise a target material with the plasma being deposited on a suitable substrate. This deposition can take place in vacuum or using an appropriate reactive gas. This process was pioneered by Smith and Turner [51] who used a ruby laser to deposit single element thin films. But this technique attracted the attention of the scientific community when Dijkamp [52] successfully deposited superconducting films of $YBa_2Cu_3O_7$. Subsequently, a very wide range of materials has been successfully produced using this technique. They include metals such as Co and Cu, insulators like $SrTiO_3$ or Al_2O_3, semiconductors like GaN, the manganese perovskites and double perovskites. Although PLD is not used at an industrial level it is a very valuable research tool since the stoichiometry is maintained in the process of transferring the material

from the target to the substrate.

The laser ablation process takes place in three stages: vaporization of a target material, transport of the vapour plume and the film growth on a substrate [28].

The interaction between laser light and a target material is a complex one involving several mechanisms such as energy absorption by the electrons and phonons in the lattice or free carrier absorption at the material surface. A basic evaluation of the effect of a laser pulse on a material can be obtained by the expression

$$E = \sqrt{\frac{2\Phi}{c\epsilon n}} \tag{13}$$

where E is the electric field of the electromagnetic wave, Φ is the power density, n the refractive index of the material, ϵ the material electric permittivity and c the speed of light. A typical value of $\Phi = 5 \times 10^9$ Wcm^{-2} is obtained in most experimental set-ups. Considering a material such as $SrTiO_3$ with n=2.41 and $\epsilon_r = 310$, the electric field inside the material will be $\sim 5 \times 10^4$ Vcm^{-1} which is sufficiently high to cause dielectric breakdown. Therefore, any material that absorbs a high enough laser power density will be transformed into a plasma. These high power densities can be obtained by using very short laser pulses typically of the order of 10 ns. The use of short laser pulses also provides congruent evaporation of material which allows stoichiometric transfer of the target material onto the substrate. This is possible if the heated volume is equal or smaller than the volume ablated per pulse. The heated volume is characterized by the thermal diffusion length during the laser-target interaction L=$2\sqrt{D\tau}$, where D is the thermal diffusivity and τ is the laser pulse length.

One of the major drawbacks on the use of PLD is the contamination of the deposited film with micron sized droplets [55]. There are three types of particles that can be distinguished by whether the original matter just ejected from the target is in the solid, liquid or vapour state

[28]. The size of the particles originated from the vapour state is generally in the nanometer range. In the other two cases, the particle size is in the micron and submicron range. Several mechanisms have been proposed to explain the formation of these particles: (1) protruding surface features, craters, cracks being mechanically removed from the target due to laser induced thermal and mechanical shock; (2) expansion of gas bubbles trapped beneath the surface during laser irradiation forcing the ejection of surface material; (3) condensation from vapour species due to supersaturation mainly at high gas pressures; (4) splashing of the molten layer caused by the presence of a superheated sublayer or from the laser induced recoil due to rapid surface evaporation [54].

The number of particles deposited can be decreased by reducing the laser power density to values near the ablation threshold. In ceramic materials such as $YBa_2Cu_3O_7$ or the manganites, this can be achieved by using smaller laser wavelengths and introducing a background atmosphere of a reactive gas such as O_2 or N_2[2] [27]. A series of mechanical devices and deposition geometries that reduce the number of particles have been described by several authors [28]. One of them is a curved magnetic solenoid used to guide the plume towards the substrate while the heavy particles get stuck to the inner walls of the solenoid [58].

The plasma emitted from the ablated target consists of highly energetic species ($\sim$ 50 eV) and is highly forward peaked. These energetic species yield a high surface mobility which can significantly improve the crystalline quality of the deposited film [59]. However the arrival energy of the ablated species should not be so high that it would induce defects or possible resputtering [60].

The fact that the plasma is so highly directed is one of the major obstacles in the use of PLD for industrial applications since it leads to poor thickness uniformity. This problem

can be overcome to some extent by either rotating the substrate or by sweeping the laser beam over the target surface. A combination of both techniques has been used to produce $YBa_2Cu_3O_7$ films with very uniform physical and transport properties on $SrTiO_3$ substrates with 75 mm diameter [61]. Metallic films of elements like Cu or Fe are normally deposited in vacuum while oxides such as $YBa_2Cu_3O_7$ or $(La_{0.7}Sr_{0.3})MnO_3$ normally require an oxygen background atmosphere. The role of the reactive gas is twofold: (i) it attenuates the plume allowing the control of the energy of the plasma species; (ii) it reacts with the metallic species forming oxides that ensure single phase formation with precise composition/stoichiometry.

The film growth on a substrate can occur in three distinct modes: (i) three dimensional cluster nucleation and growth; (ii) two dimensional full monolayer growth and (iii) growth of two dimensional monolayers followed by three dimensional clusters. The processes involved in the formation of atom clusters on a substrate are illustrated in Figure 1.8.

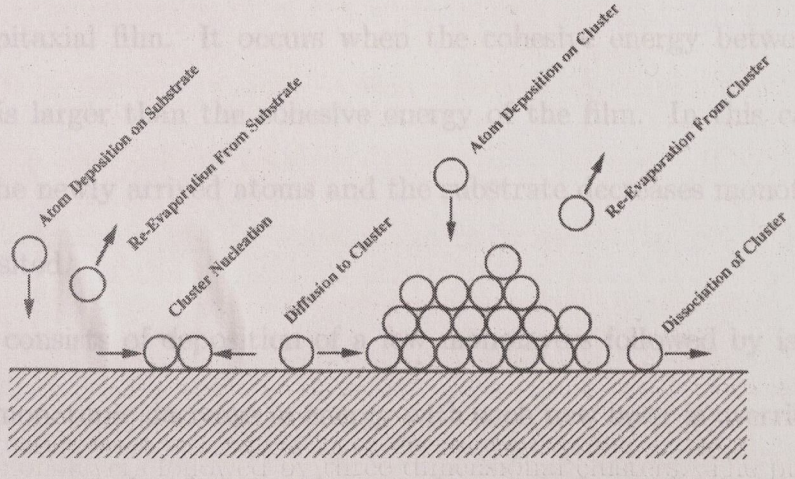


Figure 1.8.The mechanisms envolved in the initial growth of a film on a substrate.

The growth and dissociation processes for a given cluster are governed by the total free

energy of the cluster relative to an assembly of individual atoms [62]. Rearrangement of small clusters can occur by surface diffusion giving rise to a more stable shape. The surface of a real solid is rarely perfect and defects modify the binding energy of an atom to the surface and therefore modify nucleation. Surface rearrangements are possible at high temperature while they are inhibited at low temperature. A low temperature can slow down the formation of an equilibrium compound or crystal structure, so that a metastable microstructure is produced. A common example of this phenomenon is the change from crystalline to amorphous phase of films deposited at low temperatures. The three modes of crystal growth are briefly described below [63].

Island growth results in the formation and growth of isolated three dimensional clusters. This occurs when the cohesive energy of the film atoms is greater than the cohesive binding energy between the film and substrate atoms. This mode can result in an epitaxial film with a rough surface or a polycrystalline film.

Layer by layer growth consists of deposition of one monolayer at a time and results in a very smooth epitaxial film. It occurs when the cohesive energy between the film and substrate atoms is larger than the cohesive energy of the film. In this case the cohesive energy between the newly arrived atoms and the substrate decreases monotonically as each new layer is deposited.

Mixed growth consists of deposition of a few monolayers followed by island growth. It occurs when the monotonic decrease in energy with each new layer is overridden by the film cohesive energy or some other factor such as strain energy due to lattice mismatch.

The deposition conditions vary significantly for different compounds and the main challenge lies in controlling each of the numerous deposition parameters such as laser wavelength,

duration of laser pulse, pulse frequency, distance between target and substrate, gas used, pressure during deposition, substrate used, substrate temperature.

Pulsed laser deposition of manganites was relatively straightforward given the chemical and structural affinities with the superconducting cuprates. A wide range of compositions and stoichiometries have been deposited [18]. This is particularly important if the compounds with higher T_C are to be used in electronic devices with most of the research concentrated on the fabrication of magnetic tunnel junctions using a thin layer of an insulating material sandwiched between two CMR electrodes.

1.6 Devices

Many attempts have been made at producing devices based on manganese perovskites but their operation is still restricted to low temperatures. Mahendiran at al.[64] developed a simple low temperature field sensor based on $(La_{0.7}Sr_{0.3})CoO_3$ ceramic. The magnetoresistance of this material is linear and temperature independent below 60 K and up to fields as high as 7 Tesla but the resolution of such a sensor is very poor for small fields.

Viret et al. [6] have recently produced a spin polarised tunnel junction device that could be used as either a magnetic field sensor or a memory element. The sensitivity to low fields is improved as compared to the previous device by using $(La_{0.7}Sr_{0.3})MnO_3$ in a trilayer structure.

Recently, attempts have been made at fabricating a superconducting transistor [15][65][66] by injecting current into a superconductor from a half metallic oxide (Figure 1.9). The I-V curves of the superconductor show a decrease in the critical current when a current is injected from the LSMO layer. The authors claim that a spin polarised current is more efficient in breaking superconductivity than a normal current with Stroud at al. observing

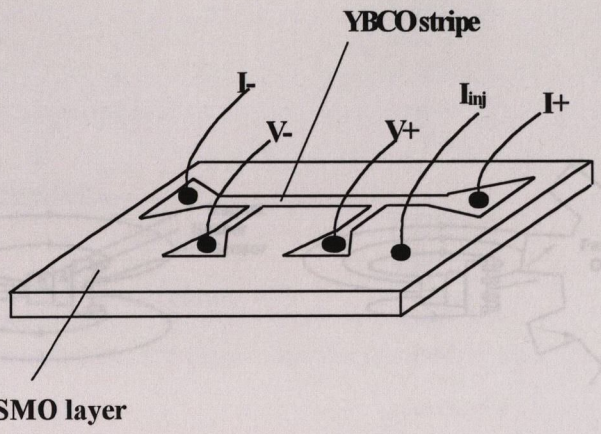


Figure 1.9.The superconducting transistor as an example of a spin electronics three terminal (I+, I-, I_{inj}) device.

a gain as high as 35 for their transistor [66]. However the origins of this effect are not yet well established. It is quite possible that the high resistance of the interface could dissipate enough heat to be responsible for the observed results.

One of the most promising applications of CMR materials is a bolometric sensor. A bolometer is a thermal detector whose operation is based on high temperature coefficient of resistance (TCR) values given by $\frac{dR}{dT}$ [67]. The TCR values for $(La_{0.7}Ca_{0.3})MnO_3$ films are around 10-18%, higher then the 2-4% found in commercial bolometers. It has been found that the optical response to low frequency radiation of $(La_{0.7}Ca_{0.3})MnO_3$ thin films is thermal in nature, demonstrated by its proportionality to $\frac{dR}{dT}$ [68].

GMR technology can be used to produce a variety of sensors. An example is the angular position sensor produced by Non Volatile Electronics to monitor the motion of mechanical components. This sensor is based on a GMR layer placed into a Wheatstone bridge for increased sensitivity. The sensor is coupled to a biasing magnet that keeps a fixed magnetisation orientation in the multilyer. The presence of a ferrous object in the proximity of the sensor leads to a change in the resistance of the multilayer which can be sensed as a change

in the voltage across the bridge (Figure 1.10).The high sensitivity and DC operation of the

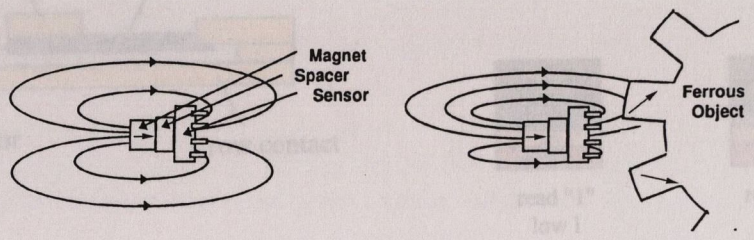


Figure 1.10. The operation of a magnetic sensor (GMR or Hall) for position detection.

GMR bridge offers an advantage over inductive sensors which have low outputs at low frequencies and can generate large noise signals when subjected to high frequency vibrations. GMR sensors are field sensors and do not measure the induced signal from the time rate of change of magnetic fields as induction sensors do [69].

Spin electronics has also been intensively studied in the field of information technology which so far has resulted in the introduction of GMR read heads for magnetic hard disk drives. There is ongoing research to produce non-volatile magnetic computer memories based on GMR materials [70].

Freitas et al. [71] produced a 20×20 (400) bit memory based on this effect. Each bit is formed by a spin-valve of NiFe/Cu/Co with the current flowing in the plane of the multilayer. Figure 1.11a) shows a schematic diagram of a memory element. The bits are arranged in a matrix and each bit is reached by column and row contacts. The write or read current flows in the column line, through the spin valve and then out through the row line. The information is stored as the magnetisation of the pinned Co layer. The write and read mechanisms are shown in Figure 1.11 b).

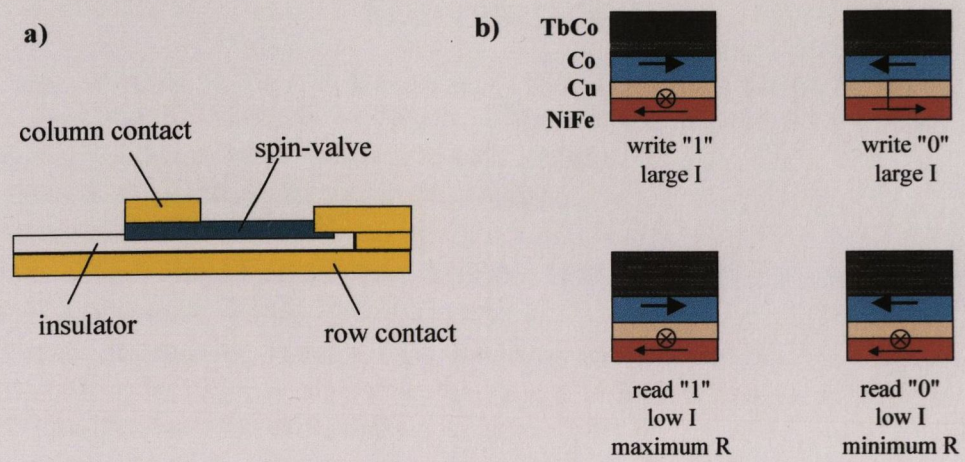


Figure 1.11. a) the spin valve RAM structure, b) the read/write process.

The write current applied on the spin-valve stripe has to be high enough to produce a field capable of reversing the pinned Co layer magnetisation. A "1" or "0" is written depending on the direction of the current. The bit contents are read by flowing a lower current through the spin-valve in a fixed direction. This read current has to be large enough to generate a magnetic field in the free NiFe layer capable of reversing its magnetisation but the field it generates in the pinned layers must leave its magnetisation unchanged. The voltage signal between the two bit states in the matrix is 2 mV which could be largely improved by using half-metallic ferromagnets as the spin-valve components. A schematic configuration of the spin valve grid is shown in Figure 1.12.

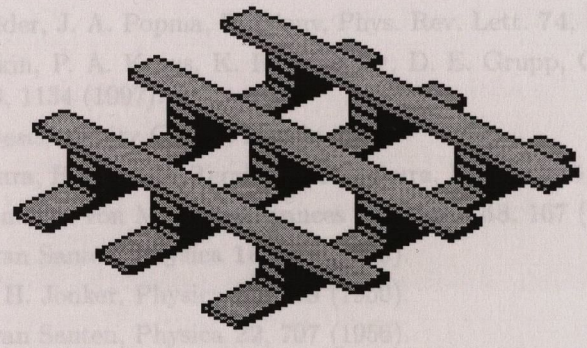


Figure 1.12.The architecture of a non-volatile RAM system.

References

[1] J. F. Gregg, W. Allen, N. Viart, R. Kirschman, C. Sirisathitkul, J. P. Schille, M. Gester, S. Thompson, P. Sparks, V. Da Costa, K. Ounadjela, M. Skvarla, J. Magn. Magn. Materials **175**, 1 (1997).

[2] J. M. D. Coey, J. Magn. Magn. Mater. **196-197**, 1 (1999).

[3] G. A. Prinz, J. Magn. Magn. Materials **200**, 57 (1999).

[4] N. F. Mott, *Proc. R. Soc.* **153**, 699 (1953).

[5] A. Fert, I. A. Campbell, Phys. Rev. Lett. **21**, 1190 (1968).

[6] A. Fert, I. A. Campbell, J. Phys. F **6**, 849 (1975).

[7] P. M. Tedrow, R. Meservey, P. Fulde, Phys. Rev. Lett. **25**, 1270 (1970).

[8] M. N. Baibich, J. M. Broto, A. Fert, F. N. Van Dau, F. Petroff, P. Eitenne, G. Creuzet, A. Friederich, J. Chazelas, Phys. Rev. Lett. **61**, 2472 (1988).

[9] See the website of Non Volatile Electronics, http://www.nve.com/.

[10] J. W. Toigo, *Scientific American*, May 2000.

[11] R. von Helmholt, J. Wecker, B. Holzapfel, L. Schultz, K. Samwer, Phys. Rev. Lett. **71**, 2331 (1993).

[12] C. Zener, Phys. Rev. **82**, 403 (1952).

[13] M. Viret, M. Drouet, J. Nassar, J. P. Contour, C. Fermon, A. Fert, Europhys. Lett. **39**, 545 (1997).

[14] D. J. Monsma, J. C. Lodder, J. A. Popma, B. Dieny, Phys. Rev. Lett. **74**, 5260 (1995).

[15] V. A. Vas'ko, V. A. Larkin, P. A. Kraus, K. R. Nikolaev, D. E. Grupp, C. A. Nordman, A. M. Goldman, Phys. Rev. Lett. **78**, 1134 (1997).

[16] Amanda Barry, *PhD. Thesis*, Trinity College Dublin 1999.

[17] K.-I. Kobayashi, T. Kimura, H. Sawada, Terakura, Y. Tokura, Nature **395**, 677 (1998).

[18] J. M. D. Coey, M. Viret and S. von Molnár, Advances in Physics **48**, 167 (1999).

[19] G. H. Jonker and J. H. van Santen, Physica **16**, 337 (1950).

[20] J. H. van Santen and G. H. Jonker, Physica **16**, 599 (1950).

[21] G. H. Jonker and J. H. van Santen, Physica **22**, 707 (1956).

[22] Y. Tokura and Y. Tomioka, J. Magn. Magn. Materials **200**, 1 (1999).

[23] A. P. Ramirez, J. Phys.: Condens. Matter **9**, 8171 (1997).

[24] Goldschmidt V., 1958, *Geochemestry* (Oxford University Press).

[25] R.-M. Thomas, PhD Thesis, Trinity College Dublin 1999.

[26] J. Volger, Physica **20**, 49 (1954).

[27] P. W. Anderson and H. Hasegawa, Phys. Rev. **100**, 675 (1955).

[28] A. J. Millis, P. B. Littlewood, B. I. Shraiman, Phys. Rev. Lett. **74**, 5144 (1995).

[29] J.-H. Park, E. Vescovo et al., Nature **392**, 794 (1998).

[30] J. Y. T. Wei, N.-C. Yeh, R. P. Vasquez, A. Gupta, J. Appl. Phys. **83**, 7366 (1998).

[31] R. J. Soulen et al., Science **282**, 85 (1998).

[32] F. K. Patterson, C. W. Moeller, R. Ward, Inorganic Chemistry **2**, 196 (1963).

[33] A. W. Sleight and J. F. Weicher, J. Phys. Chem. Solids **33**, 679 (1972).

[34] L. Pinsard-Gaudart , R. Surynarayanan, A. Revcolevschi, J. Rodriguez-Carvajal, J.-M. Greneche, P. A. I. Smith, R. M. Thomas,R. P. Borges, J. M. D. Coey, J. Appl. Phys. **87**, 7118 (2000).

[35] B. Garcia Landa, C. Ritter, M. R. Ibarra, J. Blasco, P. A. Algarabel, R. Mahendiran, J. Garcia, Solid State Communications **110**, 435 (1999).

[36] D. D. Sarma, P. Mahadevan, T. Saha-Dasgupta, S. Ray, A. Kumar, to be published in Phys. Rev. Lett.

[37] J. B. Goodenough and R. I. Dass, International Journal of Inorganic Materials **2**, 3 (2000).

[38] J. M. Greneche, M. Venkatesan, R. Suryanarayanan, J. M. D. Coey, unpublished.

[39] H. Q. Yin, J. S. Zhou, R. Dass, J. P. Zhou, J. T. McDevitt, J. B. Goodenough, J. Appl. Phys **87**, 6761 (2000).

[40] R. P. Borges, R. M. Thomas, C. Cullinan, J. M. D. Coey, R. Suryanarayanan, L. Ben-Dor, L. Pinsard-Gaudart, A. Revcolevschi, J. Phys.: Condens. Matter **11**, L445 (1999).

[41] J. M. D. Coey, Appl. Phys. Lett. **85**, 5576 (1999).

[42] J.Z. Sun and Gupta, J. Magn. Magn. Materials **200**, 24 (1999).

[43] Ashcroft and Mermin, *Solid State Physics,* Saunders College Publishing 1976.

[44] R.M.Kusters, J. Singleton, D.A. Keen, R. McGreevy, W. Hayes, Physica B **155**, 362 (1989).

[45] A. Maignan, B. Raveau, C. Martin, M. Hervieu, J. Solid State Chem. **144**, 224 (1999).

[46] G. Binasch et al, Phys. Rev. B **39**, 4824 (1989).

[47] J.-Q. Wang and G. Xiao, Phys. Rev. Lett. **49**, 3982 (1994).

[48] M. Julliere, Phys. Rev. **54A**, 225 (1975).

[49] P. M. Tedrow, R. Meservey, Phys. Rev. B **7**, 318 (1973).

[50] Y. Lu, X. W. Li, G. Q. Gong, G. Xiao, A. Gupta, P. Lecoeur, J. Z. Sun, Y. Y. Wang, V. P. Dravid, Phys. Rev. B 54, R8357 (1996).

[51] H. M. Smith, A. F. Turner, Appl. Opt. **4**, 147 (1965).

[52] D. Dijkamp, T. Venkatesan, X. D. Wu, S. A. Shaheen, N. Jisrawi, Y. H. Min-Lee, W. L. Mclean, M. Croft, Appl. Phys. Lett. **51**, 619 (1987).

[53] Douglas B. Chrisey and Graham K. Hubler, *Pulsed Laser Deposition of Thin Films*, John Wiley & Sons, Inc. (1994).

[54] A. Miotello and R. Kelly, Appl. Phys. Lett. **67**, 3535 (1995).

[55] M. Kawasaki, M. Izumi, Y. Konishi, T. Manako, Y. Tokura, *Materials Science & Engineering B-Solid State Material for Advanced Technology* **63**, 49 (1999).

[56] Duncan Cole, *PhD. Thesis*, Trinity College Dublin 1998.

[57] Justin Lawler, *PhD. Thesis*, Trinity College Dublin 1993.

[58] Rory Jordan, *PhD. Thesis*, Trinity College Dublin 1997.

[59] S. Metev and K. Meteva, Appl. Surf. Sci. **43**, 402 (1989).

[60] C. S. Ma, S. K. Hau, K. H. Wong, P. W. Chan, C. L. Choy, Appl. Phys. Lett. **69**, 2030 (1996).

[61] J. A. Greer, J. Vac. Sci. Technol. **A10**, 1821 (1992).

[62] J. E. Greene, NATO/ASI Series E **234**, 39 (1993).

[63] M. Rogalski, *Pulsed Laser Deposition of Magnetic Thin Films - Intensive Course*, Universidade do Porto (1996).

[64] R. Mahendiran, A. K. Raychaudhuri et al., Rev. Sci. Instrum. **66**, 3071 (1995).

[65] Z. W. Dong, R. Ramesh et al., Appl. Phys. Lett. **71**, 1718 (1997).

[66] D. Koller, M. S. Osofsky, D. B. Chrisey, J. S. Horwitz, R. J. Soulen, R. M. Stroud, C. R. Eddy, J. Kim, R. C. Y. Auyeung, J. M. Byers, B. F. Woodfield, G. M. Daly, T. W. Clinton, M. Johnson, J. Appl. Phys. **83**, 6774 (1998).

[67] T. Venkatesan, M. Rajeswari, Zi-Wen Dong, S. B. Ogale and R. Ramesh, *Phil. Trans. R. Soc. Lond. A* **356**, 1661 (1998).

[68] M. Rajeswari, C. H. Chen, A. Goyal, C. Kwon, M. C. Robson, R. Ramesh, T. Venkatesan, S. Lakeou, Appl. Phys. Lett. **68**, 3555 (1996).

[69] C. H. Smith, Proceedings MTEC'97 vol. **4** (1997).

[70] G. A. Prinz, *Science* **282**, 1660 (1998).

[71] L. V. Melo, L. M. Rodrigues, P. P. Freitas, IEEE Trans. Magn. **33**, 3295 (1997).

Chapter 2

Experimental Methods

This chapter gives a description of the experimental techniques employed for preparing and characterizing polycrystalline oxide ceramics. In addition, the working principles of the equipment used for thin film deposition and the patterning of thin films for device fabrication are also described.

2.1 Sample Preparation

2.1.1 Ceramics

Polycrystalline ceramic samples of manganese perovskites with general formula $(La_{0.7}Sr_{0.3})MnO_3$ were synthesized by the conventional solid state reaction of oxides and carbonates. Stoichiometric quantities of reactants were mixed, ground and fired at temperatures between 900 and 1200°C in air. The resulting powder is ground again, pressed in a pellet form and fired at 1200°C for 24 hours.

Polycrystalline ceramic samples of the double perovskites $A_2B'B''O_6$ where A=Sr, Ca, Ba and B'=Fe and B"=Mo, were prepared by solid state reaction of oxides and carbonates. Stoichiometric quantities of reactants were mixed, ground and fired at 900°C in vacuum for 3 hours. The resulting powder is ground again, pressed in a pellet form and fired at 1200°C in a continuous flow 5 % H_2 / Ar mixture for 2 hours.

2.1.2 Thin films

The thin films studied in this work were deposited by Pulsed Laser Deposition (PLD). A detailed description of PLD of manganese perovskites has been provided by Justin Lawler

[27]. The experimental system shown in figure 2.2, consists of three basic parts: the excimer laser, the vacuum chamber and the optics that guide the beam into the vacuum chamber. The description of each of these units is given below.

KrF and XeCl excimer lasers have been extensively used for PLD. KrF is the highest gain system for electrically discharged pumped excimer lasers and is the most widely used among the PLD community.

The light output from an excimer laser is derived from a molecular gain medium in which the lasing action takes place between a bound upper electronic state and a repulsive or weakly bound ground electronic state. Because the ground state is repulsive, the excimer molecule can dissociate rapidly (on the order of a vibrational period $\sim 10^{-13}$ s) as it emits a photon during transition from upper state to ground state. The high ratio of upper state lifetime to lower state lifetime makes the excimer a highly efficient system. Figure 2.1 shows a typical molecular potential energy diagram of an excimer system.

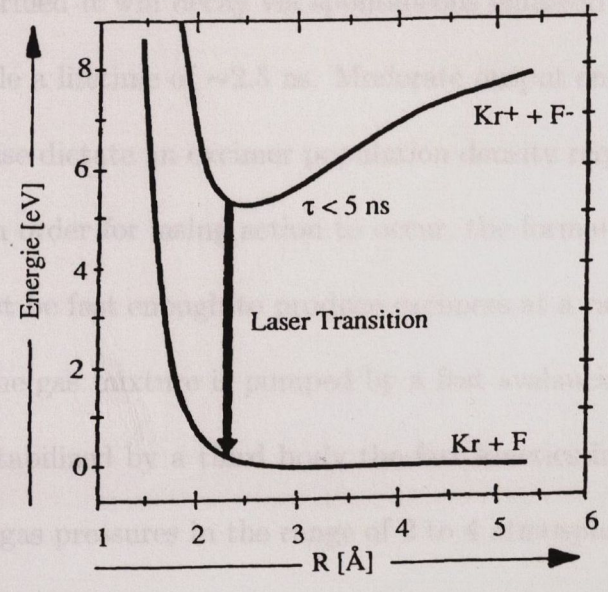


Figure 2.1.The electric potential of an excimer molecule.

The excimer molecules are formed in a gaseous mixture of their component gases, such as Kr, F_2, and He in the case of the KrF laser. Energy is pumped into the gas mixture through avalanche electric discharge excitation. The pumping creates ionic and electronically excited species that react chemically and produce the excimer molecules.

The details of the kinetics and chemical reactions leading to the formation of the excimer molecules are quite complex and can consist of many steps. Some of the more important reactions for the case of KrF are listed below where the * denotes an electronically excited species.

$Kr + e^- \rightarrow Kr^+, Kr^*, Kr_2^+$

$F_2 + e^- \rightarrow F + F^-$

$Kr^+ + F^- + He \rightarrow KrF^* + He$

$Kr_2^+ + F^- \rightarrow KrF^* + Kr$

$Kr^* + F_2 \rightarrow KrF^* + F$

Once the excimer is formed it will decay via spontaneous emission and collisional deactivation giving the molecule a lifetime of ~2.5 ns. Moderate output energies of several hundred milijoules per laser pulse dictate an excimer population density requirement on the order of $10^{15}/cm^3$. Therefore in order for lasing action to occur, the formation rate of the ionic and excited precursors must be fast enough to produce excimers at a rate of several $10^{23}/cm^3/s$. As discussed earlier, the gas mixture is pumped by a fast avalanche electric discharge. Because the excimer is stabilized by a third body the fast kinetics involved in producing the excimers require total gas pressures in the range of 2 to 4 atmospheres within the discharge volume.

Other discharge parameters are electron densities of the order of $10^{15}/cm^3$, current densities

of $10^3 A/cm^2$ and electron temperatures of approximately 1200 K. These requirements are met with electric discharge field strengths of 10-15 kV/cm and therefore the discharge voltages can be in the range of 20-45 kV for an electrode spacing of 2-3 cm. Larger electrode spacing can provide higher laser output energies.

The laser beam is guided onto the target surface by an optical system consisting of two lenses, an aperture and a mirror as shown in figure 2.2. The first lens is used to focus the beam on the aperture. The purpose of this aperture is twofold: it selects a homogeneous part of the beam and gives the beam a well defined shape. A mirror placed after the aperture deflects the beam by 90^o directing it onto an optical port on the chamber. A second lens is positioned in such a way that a demagnified image of the aperture is formed at the target surface. By using this system one can maximize the spatial homogeneity of the laser beam and make an accurate estimate of the fluence delivered to the target. By moving the first lens with respect to the aperture, the fluence can be changed keeping the spot size constant. The second lens is mounted on a rotating stage sweeping the beam on the target surface and therefore minimizing target degradation.

The deposition takes place in the vacuum chamber. It is a home made system with several ports for visualization of the interior, vacuum connections and laser beam access. A pumping station consisting of a turbo pump backed by a rotary pump can produce a vacuum of 10^{-6} mbar. A needle valve is used to introduce a background gas for deposition. Typical deposition pressures for ceramics using O_2 or N_2 are in the range 0.1-0.5 mbar. The ceramic target is mounted on a rotating carrousel that can accommodate four targets allowing the in-situ deposition of multilayers. The chosen substrate is mounted on a metal plate and it can be heated to a maximum temperature of 1200°C by two GaAs heaters placed at the back of the

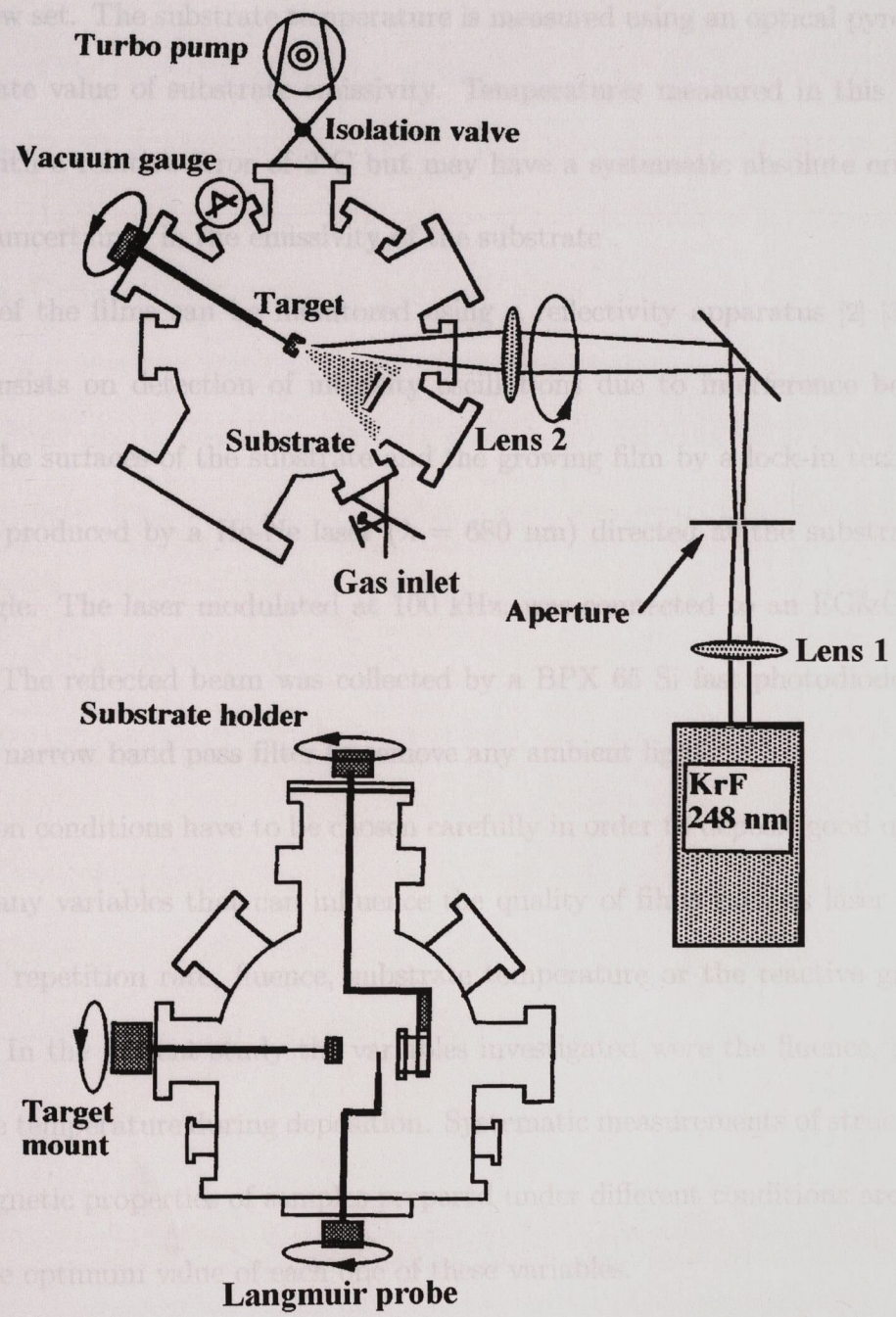


Figure 2.2.Schematic representation of the pulsed laser deposition apparatus used in this study.

substrate holder. The maximum voltage that can be supplied to the terminals of each heater is 110 V and care should be taken not to exceed this value at the cost of having to replace them by a new set. The substrate temperature is measured using an optical pyrometer with the appropriate value of substrate emissivity. Temperatures measured in this way will be consistent, with a relative error of 2^oC but may have a systematic absolute error of up to 40^oC due to uncertainty in the emissivity of the substrate .

The growth of the films can be monitored using a reflectivity apparatus [2] [3]. Its basic operation consists on detection of intensity oscillations due to interference between light reflected at the surfaces of the substrate and the growing film by a lock-in technique. The light used is produced by a He-Ne laser (λ = 680 nm) directed at the substrate at a 30^o incidence angle. The laser modulated at 100 kHz, was connected to an EG&G 5101 lock-in detector. The reflected beam was collected by a BPX 65 Si fast photodiode which was covered by a narrow band pass filter to remove any ambient light.

The deposition conditions have to be chosen carefully in order to deposit good quality films. There are many variables that can influence the quality of films such as laser wavelength, pulse length, repetition rate, fluence, substrate temperature or the reactive gas used and its pressure. In the present study the variables investigated were the fluence, gas pressure and substrate temperature during deposition. Systematic measurements of structural, transport and magnetic properties of samples prepared under different conditions are required to determine the optimum value of each one of these variables.

2.2 Structural characterisation

2.2.1 X-ray diffraction

The structure of the compounds was characterized by X-ray diffraction (XRD). This technique enables the precise determination of the phase produced and the degree of orientation of thin films. The X-ray radiation has a wavelength of the order of 1Å which is the order of magnitude of separation of atoms in a crystal lattice. This radiation is diffracted by a regular array of atoms producing a pattern of intensity peaks.

The X-ray diffractometer used in the present study was a Siemens D500 with Cu $K_{\alpha 1}$ radiation of wavelength λ =1.54056 Å. The lattice parameters were calculated from the X-ray diffraction data by least-squares refinement. In this work the θ-2θ geometry is used to characterise both ceramic and thin film samples.

The θ-2θ geometry is most commonly employed for the identification of randomly oriented powders, but can also be used for the analysis of oriented thin films. The sample, mounted at the centre of the diffractometer, is rotated by an angle θ through an axis in the sample plane, while the detector rotates about the same axis through a corresponding angle 2θ. Under such circumstances, diffraction from a set of [hkl] lattice planes occurs when the Bragg law

$$n\lambda = 2d \sin\theta \tag{14}$$

is satisfied. In this expression, λ is the X-rays wavelength, and d is the distance between crystal planes. Therefore, only [hkl] planes coplanar with the sample plane contribute to the diffraction intensity. So in the case of ceramics where the measurement is performed on a randomly oriented powder one can expect to observe all the [hkl] sets of planes while in thin films a diffracted signal is only detected if the film growth is along a crystallographic

direction normal to the film surface.

2.2.2 Morphology

Surface morphology of thin film and ceramic samples was studied using a Hitachi S-3500N variable pressure scanning electron microscope (SEM). In addition, thin film samples were also studied by atomic force microscopy (AFM). SEM involves the detection of secondary or back-scattered electrons after bombarding the sample with 20 keV electrons. The electron beam is focused by a magnetic field produced by a set of coils. The electrons, which possess a much greater energy than optical photons, give rise to a much higher magnification and image resolution than any optical microscope. This unit is also equipped with an EDAX (energy dispersive analysis of x-rays) facility. This facility performs an analysis of the resulting primary x-rays, characteristic of the elements present, emitted when a sample is bombarded with 20 keV electrons. The data is calibrated with a known specimen and the relative concentration of the elements may then be concluded. Although the elements with atomic number smaller than 13 can not be detected by this method , the technique is very useful to determine the chemical composition of compounds and to identify the impurities present in a crystal lattice.

AFM images of thin films were taken using a Digital Instruments MultiMode AFM. These images are acquired by monitoring the deflection of a cantilever positioned close to the film surface. The acquisition can be made in either contact or tapping modes. In contact mode, the topography is measured by sliding the probe's tip across the sample surface. In tapping mode, the topography is measured by tapping the surface with an oscillating tip. Tapping mode has the advantage of eliminating shear forces that can cause damage to soft samples.

2.3 Transport Properties

2.3.1 Resistance versus temperature

Resistance measurements as a function of temperature were carried out on both ceramics and films using a four point probe technique. The equipment used was built in Trinity College, Dublin and it can measure the resistance of a sample as a function of temperature in the range 12-300 K. Four equidistant in line electrical contacts (Montgomery geometry) were made by gluing 100 μm diameter silver wire with silver paint to the sample surface. The sample is then placed on the copper head using heat sink and the silver wires are connected to the voltage and current probes. Temperature control is made via a diode placed near the sample. A DC current is applied using a Keithley 224 constant current source and the output voltage was measured using a Keithley 195A voltmeter.

To deduce the value of resistivity the formula

$$\rho = \frac{RS}{l} \tag{15}$$

is used were ρ is the resistivity, R the measured resistance, S the cross section of the sample and l the distance between the two voltage contacts. To obtain an accurate value of resistivity it is important that the samples have a regular shape so that the error in measuring S and l can be minimised.

2.3.2 Magnetoresistance

Resistance as a function of applied magnetic field can be measured at room temperature and 77 K. The procedure to measure the sample resistance is the same as described in the previous section. However the sample is introduced in the bore of a MULTIMAG consisting of two concentric Halbach cylinders that can generate a homogeneous magnetic field of up

to 1.2 Tesla. The direction of the magnetic field can be varied in the plane of the sample. As a standard procedure the magnetic field is varied between -1.2 Tesla and 1.2 Tesla in the direction of the applied current. Anisotropic magnetoresistance (AMR) can be measured by rotating a field of chosen amplitude in the plane of the sample.

2.4 Magnetic properties

2.4.1 Transverse magnetooptic Kerr effect

Room temperature hysteresis loops of thin film samples were measured by Magneto Optic Kerr Effect (MOKE). The facility available in our laboratory allows the user to measure transverse Kerr effect. A detailed description of the equipment and its operation has been given elsewhere [4]. The basic feature of Kerr effect is the change of polarization of light reflected from the surface of a magnetic material. The light source is a 1 kHz modulated laser diode operating at 670 nm. In the transverse geometry, measuring the Kerr effect is equivalent to measuring a change in reflectivity of a magnetic surface for light polarized in the plane of incidence and the magnetisation perpendicular to the plane of incidence. The magnitude of the effect is quite small making it extremely sensitive to optical noise. In order to make the measurement more efficient the light is polarized at 45^o to the plane of incidence by a Glan-Thompson polariser and split in two components (parallel and perpendicular to the plane of incidence) after reflection from the sample surface. The two components are detected by a set of photodiodes and the difference in intensity between them is measured by a differential amplifier. This signal is sent to a lock-in amplifier operating at the modulating frequency of the laser and the output of the lock-in is plotted as a function of applied magnetic field. This magnetic field is supplied by a set of Helmholtz coils that can produce

a maximum field μ_0H=10 mT and the field sweep is provided by a computer controlled current.

Since what we measure is a change in reflectivity, this technique does not allow a direct measurement of the magnetisation of the sample. However one can make a quantitative measurement of the coercivity and a qualitative analysis of the shape of the hysteresis loop.

2.4.2 SQUID measurements

Magnetisation as a function of temperature and field was measured on both ceramic and thin film samples using a SQUID magnetometer. The magnetisation of the thin films described in Chapter 3 was measured in Laboratoire Léon Brillouin CEA/CNRS, CEA Saclay. The magnetisation of the samples in Chapter 4 was measured in Laboratoire de Physicochimie des Solides du CNRS, Université Paris-Sud (ceramics) and Unité mixte de recherche n°137 CNRS-THOMSON, Orsay (thin films).

2.5 Microlithography

2.5.1 Mask design

The most important step in determining the structure of a chip (in this case the chip is a ceramic thin film) is the step of lithography. Masks are made in a certain patterns so as to let light through where desired: light is passed through these masks and reacts with the photoresist film, and the wafer undergoes a chemical process that removes the light-stimulated photoresist from the chip. In order to fabricate the desired microstructures a lithography mask was designed. This was done trough a software package called KIC supplied by Photronics and available from the Internet in a UNIX terminal. The program presents the user with a grid of a chosen size over which the different features are placed. The program

allows the user to create the desired features from a set geometric figures. The final design is sent to the producer and the features are transferred via electron beam lithography onto a chromium film deposited on a quartz plate (2x2 inches in this case).

2.5.2 Resist spinning

The material used to mask the films is a ultra violet sensitive polymer. A few drops are put on top of a thin film. The sample is then spun at high speed in a resist spinner to remove the excess polymer leaving the film covered with a homogeneous layer approximately 1 mm thick. The resist spinner consists of a rotary stage with adjustable angular velocity to a maximum value of 8000 rpm. A chuck with vacuum connections on top of the rotary stage is used as a sample holder, the vacuum being enough to hold the sample in place during rotation. A careful choice of speed has to be made for each material in order to assure a homogenous covering of the films.

2.5.3 Ultra-Violet lithography

The mask patterns were transferred onto the resist using a SUSS MJB 3 UV200 Mask Aligner. This equipment is designed for high resolution photolithography in a laboratory or pilot production environment. Brief description of the system and its operation are summarized below.

The SUSS MJB 3 UV200 (figure 2.3) incorporates a high precision alignment stage and performs exposures in vacuum contact, hard contact and soft contact. The MJB 3 UV200 uses a diffraction reducing optical system optimized for exposure wavelengths between 210-230 nm. A cadmium-xenon lamp is used and the entire light path is flushed with nitrogen to eliminate the production of ozone and consequently reduce attenuation of the exposure radiation. Resolution of the MJB 3 UV200 is 0.2 microns under optimum conditions.

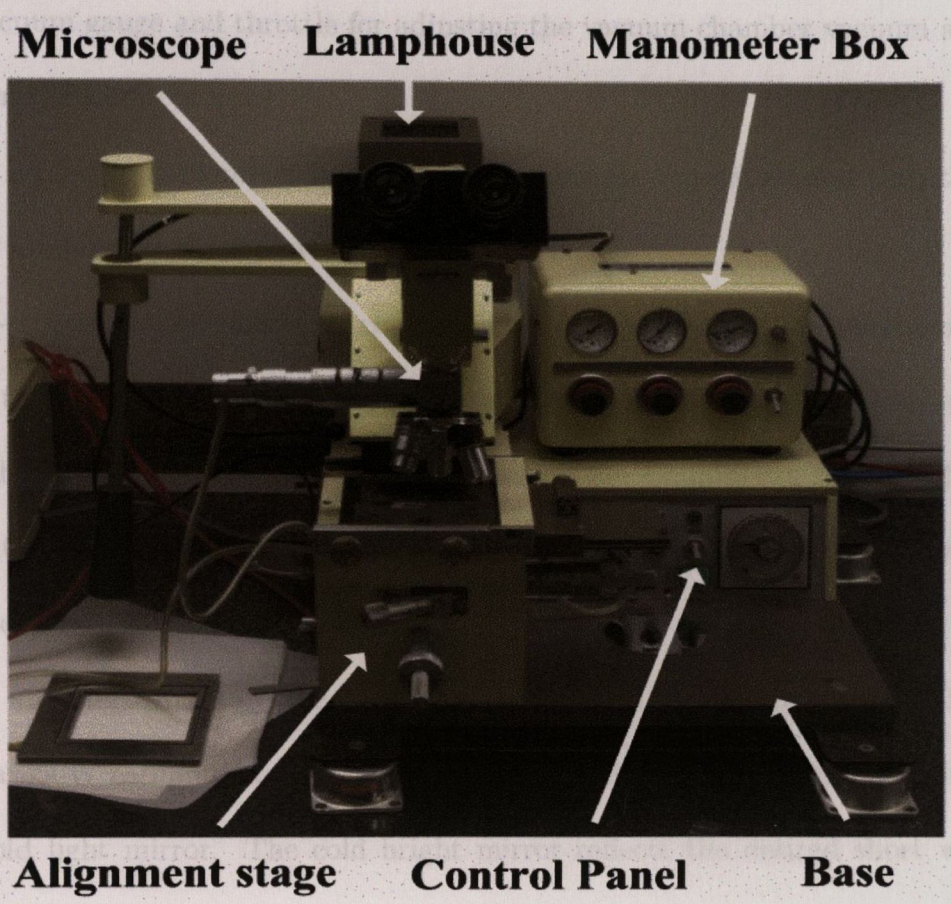


Figure 2.3.The components of the SUSS mask aligner.

The MJB 3 is made up of discrete subassemblies. They are as follows.

Alignment stage - the alignment stage is the heart of the MJB 3 consists of the pneumatics and mechanics for mask/substrate parallelity compensation, mask and substrate vacuum, maskholder (and maskholder clamping mechanism), Z-axis movement, alignment separation mechanism, X, Y and Theta alignment micrometers, and variable thickness adjustment.

Machine base - the base contains the relays, pneumatics, valves and throttles which control the various machine functions.

Front control panel - the front control panel contains the indicators and operating controls, including the CONTACT indicator light, HP/ST exposure mode selection button, MASK VACUUM button, EXPOSURE button, VACUUM CHAMBER button, and the exposure

timer. A vacuum gauge and throttle for adjusting the vacuum chamber vacuum are located at the left end of the front panel.

Manometer box - the manometer box contains the gauges, regulators and throttles for adjustment of compressed air and nitrogen to the machine.

Microscope - the microscope assembly consists of the microscope adapter, microscope manipulator, and the microscope itself. The microscope manipulator is equipped with pneumatic brakes which are unlocked by pressing the buttons on the manipulator handle. By pressing only one button, one can select an X-only or Y-only scan. If both buttons are pressed the microscope can be scanned in any direction.

Lamphouse and mirrorhouse - the MJB 3 UV200 model is equipped with a lamphouse containing a 350W cadmium-xenon vapour exposure lamp, an ellipsoidal collecting mirror, and a 45°cold light mirror. The cold bright mirror reflects the desired short wavelength ultraviolet light through a lens and transmits the longer wavelengths to a heat sink located in the bottom of the lamphouse. Adjustment knobs for moving the lamp in X, Y and Z are located on the upper section of the lamphouse. The mirrorhouse contains two condenser lenses, a diffraction lens plate, a 45°surface mirror and a collimation lens. In addition, the entire light path is flushed with nitrogen to eliminate the production of ozone. The SUSS diffraction reducing exposure system provides very high resolution over the entire exposure area, resulting in steep resist edges and small diffraction effects.

The operation of the SUSS MJB 3 is straightforward. First, a mask is loaded into the machine. Then the substrate is placed on the chuck and the chuck is inserted into the alignment stage.

At this point, the substrate is brought into contact with the mask by turning the contact

lever counterclockwise. The CONTACT light on the front panel illuminates. This operation also accomplishes wedge error (parallelity) compensation.

By pulling the separation lever towards the front of the machine, sufficient separation will be obtained for alignment, and the CONTACT light will go out. The substrate can now be aligned to the mask using the X, Y, and Theta micrometers. By using the precision microscope manipulator, the microscope can be scanned over the substrate in either the X or Y direction, or both simultaneously.

When satisfactory alignment has been obtained, the substrate should be moved back into contact with the mask by pushing the separation lever all the way to its rearmost position until the CONTACT light re-illuminates. The substrate is now ready for exposure.

Exposure is initiated by setting the exposure time on the timer and pressing the EXPOSURE button. The microscope will then elevate a sufficient distance to allow the objective to clear the maskholder (this lifting is not necessary in all cases). The mirrorhouse now moves forward over the mask. When the mirrorhouse reaches its foremost position the shutter opens and exposure takes place for the specified amount of time. After exposure is complete, the shutter closes, the mirrorhouse retracts, and the microscope moves back down to its original position. The substrate can now be unloaded by rotating the contact lever fully towards the front of the machine, releasing the substrate from the mask. The transport slide should be carefully pulled to the right and the substrate removed from the chuck.

Exposure Modes

This model offers two exposure modes which you may select using the HP/ST and SOFT CONTACT buttons on the front panel of the machine. These buttons control what takes place at the interface of the substrate and the mask when the EXPOSURE button is pressed.

A brief description of the exposure modes follows.

Vacuum Contact (HP) Mode - In the HP mode, a vacuum is pulled between the mask and the substrate immediately prior to exposure. The highest possible resolution is obtained in this mode, since the gap between substrate and mask due to flatness variations, dust particles, etc., is as small as possible. Chucks equipped with vacuum gaskets must be used in this mode in order to obtain a vacuum between the substrate and the mask.

Standard (ST) Mode - In the ST Mode, nitrogen is used to press the substrate against the mask during exposure (hard contact), or the substrate is pressed against the mask only by mechanical pressure while vacuum under the substrate is retained (soft contact). Chucks with or without vacuum gaskets may be used in this mode.

2.5.4 Ion beam milling

In simple terms ion beam milling can be viewed as an atomic sand blaster. The grains of sand are actually submicron ion particles accelerated to bombard the surface of the work mounted on a rotating table inside a vacuum chamber. The work is typically a wafer, substrate or element that requires material removal by atomic sandblasting or dry etching. A selectively applied protectant photo sensitive resist, is applied to the work element prior to introduction into the ion miller. The resist protects the underlying material during the etching process which may be up to eight hours or longer, depending upon the amount to be removed and the etch rate of the materials. Everything that is exposed to the collimated ion beam etches during the process cycle, even the resist. In most micromaching applications the desired material to be removed etches at a rate 3 to 10 times faster than the resist protectant thus preserving the material and features underneath the resist.

Thin films were etched using a Commonwealth Scientific Corporation Model 3226 ion beam

miller (Figure 2.4). This model is designed for industrial applications and can produce a highly uniform ion beam. The description of the main components of the equipment is given below.

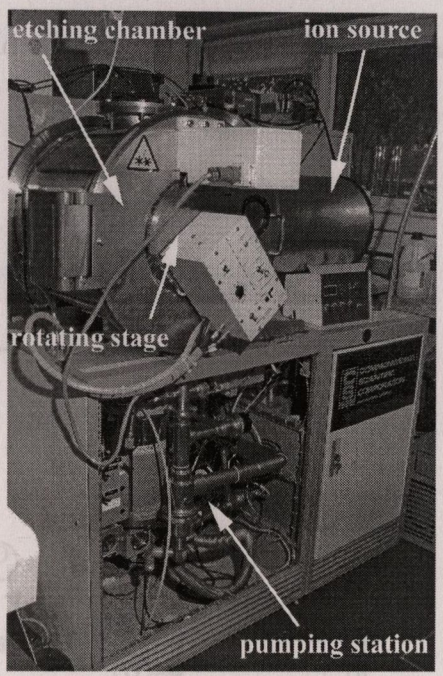


Figure 2.4. The CSC 3226 ion beam miller.

The etching takes place in the **etching chamber** which is a horizontal stainless steel cylinder with high vacuum compatible fabricating techniques used throughout. The outer wall of the chamber is water cooled with a continuous stainless steel tubing welded to the wall surface to provide a cool radiation sink. Inside the chamber there is a **rotating stage** where samples can be mounted. This stage is driven by a motor and it allows a choice of angle of incidence of the plasma on the sample surface between 10^o and 90^o. A **pumping station,** consisting of a cryogenic pump backed up by a mechanical pump, is mounted directly below the chamber. The operation of these pumps can be controlled either manually or by the computer installed in the control unit. Thermocouple vacuum gauges are located in the chamber and the cryopump. A Millatron VIII Kaufman type **ion source** is mounted

horizontally and connected by a port to the etching chamber. This ion source provides a neutralized and unidirectional 20 cm diameter beam. This beam is ionized by electrons emitted by a hot tungsten filament which are focused by a magnetic field produced by a solenoid. A local electric field at the optics (or grids) extracts the ionized gas into the etching chamber.

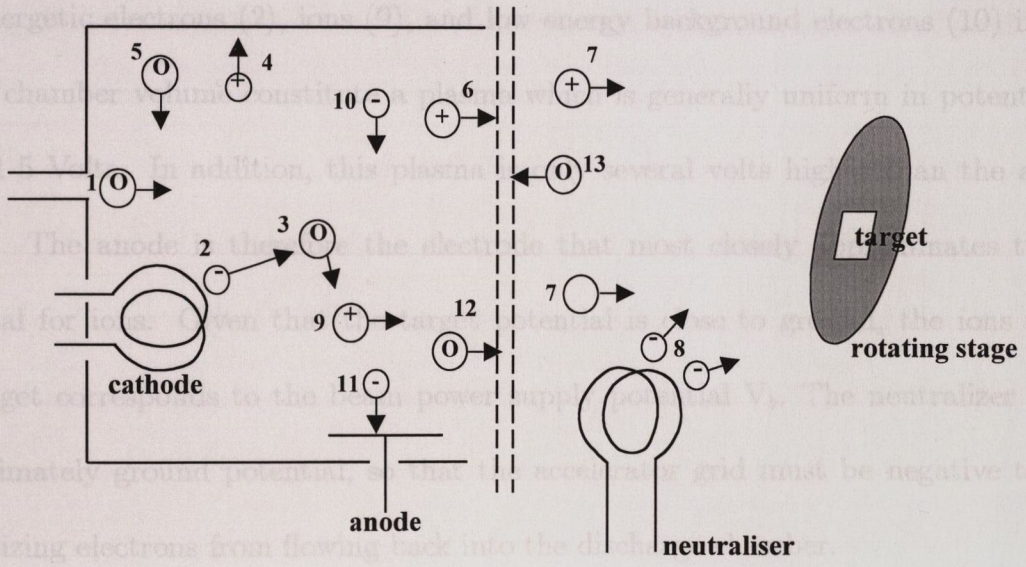


Figure 2.5. Schematic representation of the ion source.

Figure 2.5 describes the basic operation of the ion-source. The neutral Ar atoms (1) are introduced in the discharge chamber through a port on the chamber wall. Energetic electrons (2) from the cathode (also called main or discharge chamber cathode) strike the Ar atoms (3) within the **discharge chamber**. Some of the ions (4) produced by this collision reach various surfaces within the discharge chamber, recombine with electrons at these surfaces and return to the discharge chamber volume as neutral atoms (5). The other ions (6) form small

beamlets by passing through the holes in the **screen grid**. The ions in these beamlets are attracted to the negatively polarized **accelerator grid**, but in normal operation they pass through the grid without hitting it due to the alignment of the holes in the two grids. The ion beam (7) is formed by the sum of individual beamlets after they leave the accelerator grid. The ion beam is neutralized by electrons (8) from the neutralizer (or neutralizer cathode). The neutralized beam has equal densities of electrons and ions within the beam volume, and in some cases equal arrival rates of electrons and ions at the target surface.

The energetic electrons (2), ions (9), and low energy background electrons (10) in the discharge chamber volume constitute a plasma which is generally uniform in potential in the range 1-5 Volts. In addition, this plasma is only several volts higher than the anode potential. The anode is therefore the electrode that most closely approximates the source potential for ions. Given that the target potential is close to ground, the ions energy at the target corresponds to the beam power supply potential V_b. The neutralizer is also at approximately ground potential, so that the accelerator grid must be negative to prevent neutralizing electrons from flowing back into the discharge chamber.

The pressure in the discharge chamber is normally low enough so that the path length between collisions for an atom is much larger than the discharge chamber dimensions. To increase the probability of ionization by an energetic electron (2) from the cathode before it escapes to the anode, a magnetic field (not shown in Figure 2.5) is applied between the cathode and the anode. In this case the magnetic field is produced with an electromagnet although other experimental set-ups would use a permanent magnet.

Although the magnetic field is effective in containing energetic electrons (2), the low energy background electrons (10) can diffuse across the magnetic field relatively easily. The electron

current between the cathode and the anode is therefore completed by low energy electrons (11) reaching the anode. The low operating pressure also results in a gas flow from the etching chamber into the discharge chamber. The gas flow is normally from the inlet port to the ion source and then through the two grids into the etching chamber. Because the path length between collisions is large, the outgoing atoms or molecules (12) seldom collide with incoming atoms or molecules (13). It should therefore be taken into account that if different gases are used in the etching chamber and ion source there will always be a mixture of the two gases in the ion source. Even if the gas pressure in the ion source is higher than that of the etching chamber, this mixing should be taken into account.

Ion milling uses this energetic beam of charged atoms or ions emitted from the ion gun to remove material from the surface of a film one atom at a time. The energy of the beam ranges from 100 to 1000 eV. The removal process, called sputtering, is a physical phenomena in which the ions strike the surface of the film with sufficient energy to remove atoms from near the surface. The amount of material removed from the surface of the film depends on the amount of time that the ion beam dwells at one location on the surface.

References

[1] Justin Lawler, PhD thesis, Trinity College, Dublin, 1994.

[2] Duncan Cole, PhD thesis, Trinity College, Dublin, 1998.

[3] P. M. Dodd, M.Sc. Thesis, Trinity College Dublin, 1993.

[4] Orphee Cugat, PhD thesis, Université Joseph Fourier - Grenoble, 1991.

Chapter 3

Manganese Perovskites

3.1 Introduction

There has been much interest in manganese perovskites since the discovery of colossal magnetoresistance (CMR) on $(La_{0.7}Ba_{0.3})MnO_3$ thin films [1]. The transport of a spin polarised current via the double-exchange mechanism makes these materials attractive for applications in spin electronics. Thin films have been used in the fabrication of prototype devices with a special interest in $(La_{0.7}Sr_{0.3})MnO_3$ (LSMO) because it has the lowest resistivity and the highest Curie temperature (T_C) of the ferromagnetic manganite series [2]. Recent measurements which have indicated complete or near complete spin polarisation of the 3d band in this material (half metallic ferromagnetism) include studies of spin-polarised tunnel junctions (88% polarisation) [6], Andreev reflection (80%) [4] and spin resolved photoemission ($\approx$100%) [7]. Related materials with calcium (LCMO) and barium (LBMO) have higher resistivity and lower T_C. The CMR observed near T_C opens a wide range of possibilities for electronic applications of these materials and it is hoped that it will be possible to operate devices based on this type of material at room temperature. Another possibility is to fabricate devices that make use of the half metallic properties of these materials. One such device is a magnetic tunnel junction consisting of a layer of $SrTiO_3$ sandwiched between two LSMO layers [6] [6] [7]. Magnetoresistance values of more than 400% are obtained at 4 K but the effect disappointingly vanishes at around 150 K [6]. It is important to understand whether the loss of spin polarisation with increasing temperature is an intrinsic effect related, for example, to spin wave excitations or magnetic surface reconstruction, or an extrinsic effect related

to impurities or imperfect device fabrication.

At temperatures below T_C a small magnetoresistance should arise only from the reduction of spin fluctuations by an applied magnetic field. However, early low temperature measurements of magnetoresistance in different manganese perovskites did not confirm this expectation. Ju et al. [8] in a study of $(La_{0.7}Ba_{0.3})MnO_3$ polycrystalline ceramic found that the MR ratio at temperatures well below $T_C = 340K$ is similar to that found near T_C ($\sim$40%). The MR loops show a sharp decrease of resistance at low fields and above a field of 0.3 Tesla the resistance decreases linearly with applied field. The authors explain these features of the low field MR with the double exchange mechanism. A small applied field aligns the different magnetic domains within the sample and as a result electrons are transferred more easily across the domain wall boundaries and there is a sharp drop in resistivity. The high field effect is explained by the suppression of a small canting of the moments of manganese ions that makes the electron transfer between Mn^{3+} and Mn^{4+} ions easier. Schiffer et al. [9] found the same features for the low temperature MR as Ju et al. However, they consider the possibility of the low field MR arising from ordering of spins in the domain walls.

The origin of the low temperature MR was finally clarified in a paper by Hwang et al. [10]. The authors studied the temperature dependence of magnetisation, magnetoresistance and resistivity of two ceramic samples and a single crystal of $(La_{2/3}Sr_{1/3})MnO_3$. All samples show the same temperature and magnetic field dependence of magnetisation but the value of resistivity of the ceramics is 1 to 2 orders of magnitude greater than that of the single crystal. Furthermore the single crystal sample exhibits the expected behaviour of a double exchange system, namely a large negative magnetoresistance near T_C that progressively vanishes with decreasing temperature. On the other hand, the magnetoresistance of the

polycrystalline samples shows the large low temperature drop observed by previous authors. This clearly establishes the origin of the low temperature effect in the transport through grain boundaries. The previous assumption of transport through domain walls [9] is disproved by the fact that the resistivity decreases smoothly in the low applied field region of magnetic domain rotation. The authors also propose a model for the transport based on spin-polarised intergrain tunnelling.

Since the finding of Hwang et al. much effort has been made by scientists to isolate and understand the contribution of grain boundaries to the transport properties of manganese perovskites. These attempts can be divided in two main approaches to the problem: the study of natural and artificial grain boundaries. Natural grain boundaries are found in polycrystalline films, ceramics and pressed powders. Gupta et al. [11] studied epitaxial and polycrystalline films of $(La_{0.67}Ca_{0.33})MnO_3$ deposited on $SrTiO_3$ substrates by pulsed laser deposition. Polycrystalline films were obtained by deposition on polycrystalline substrates prepared by cutting and polishing sintered pellets of $SrTiO_3$. The time and temperature of sintering were varied to obtain substrates with average grain sizes of 24, 14 and 3 μm and this grain structure was reproduced on the deposited films. The resistance decreases with an applied magnetic field for all films. However, unlike the epitaxial film were the drop occurs only near T_C, the resistance decreases over a much wider temperature range for the polycrystalline samples and persists at low temperatures. The MR of these films also shows a large low field component followed by a more gradual drop at higher fields. A value of $6\times10^{-5}\Omega cm^2$ was obtained for the grain boundary resistivity. High field magnetoresistance measurements on LSMO ceramics with different grain sizes were performed by Balcells et al. [19] who show that the magnetic properties are dominated by non colinear surface layers

as the grain size decreases.

The above studies on polycrystalline samples average over the range of grain boundary angles present and their relative orientations with respect to the applied field. A much clearer picture of what happens at the interface between grains is provided by the study of artificially induced grain boundaries. Bicrystal substrates consisting of a single grain boundary, with well defined misorientation between the grains, are ideal for the growth of films in order to isolate the contribution of a single grain boundary. One method to enhance the grain boundary contribution to the total resistivity is to increase the number of grain boundary intersections by patterning a meander track along the boundary [13] [14] or using the meander track as one of the arms of a Wheatstone bridge to increase accuracy [15] [16] [17]. Reduction of the grain region that is probed will also lead to further enhancement of the grain boundary signal. The grain boundaries of LSMO films were studied for different misorientations of the bicrystal substrate (θ = 4, 24, 36.8 and 45^o) [16]. The authors found that the resistivity peak is very broad and shifted to lower temperatures and suggested this could be due to a broad distribution of depressed T_C's. The resistance of the grain boundary also increases with increasing θ suggesting more structural disorder with increasing misorientation. The magnetoresistance shows a behaviour qualitatively similar to that for polycrystalline films, with two low field hysteretic peaks at the coercive field of the bulk material. The magnitude of the low field MR was seen to increase linearly with increasing θ and decreasing temperature.

Evidence for non-homogeneity in the transport and magnetic properties of thin films has recently been reported by several authors. Sun et al. inferred the existence of an electric 'dead layer' in LSMO films deposited on NGO and LAO substrates from the thickness de-

pendence of the conductance [18]. Park et al. probed the magnetisation at different depths of an LSMO film using different photoemission techniques and found that the magnetisation of the surface layers decreases much more rapidly than the bulk of the film as the temperature is increased [19]. Recent small angle neutron scattering studies of LSMO films have been interpreted in terms of a surface layer with disordered spins [20]. A recent theoretical study by Filippetti and Pickett [21] predicts magnetic reconstruction at the surface of $CaMnO_3$, with ferromagnetic alignment of the surface manganese ions as opposed to the bulk antiferromagnetic ordering.

3.2 Film deposition

In this study we investigate the structural, magnetic and electric properties of LSMO films deposited on MgO substrates by pulsed laser deposition (PLD) and discuss the existence of magnetic and electric 'dead' layers at the interfaces of the films. The choice of substrate to be used is important in determining the magnetic and transport properties of the films. Rao et al. [22] used PLD to deposit $(La_{0.8}Ca_{0.2})MnO_3$ epitaxial films on $SrTiO_3$ (0.6% lattice mismatch) and $LaAlO_3$ (-2.4% lattice mismatch) substrates. By using normal and grazing incidence x-ray techniques the authors found that strain in both in-plane and out-of-plane lattice parameter persists up to thicknesses of 400 nm. A study of $(La_{0.67}Sr_{0.33})MnO_3$ films deposited on $LaAlO_3$ [23] also shows thickness dependent strain and resistivity. Thinner films (t<30nm) have out-of-plane lattice parameter larger than the bulk material. Furthermore, the resistivity of these film shows an insulator like behaviour. The bulk value lattice parameter together with metallic behaviour is only obtained for films thicker than 50 nm. Other studies have reached the same conclusion that a small lattice mismatch between film and substrate can lead to the accumulation of strain in the lattice up to quite large thick-

nesses [24] [25]. This strain has a strong influence in both magnetic and transport properties. Surprisingly, the best films are obtained on MgO because despite the large lattice mismatch ($\sim 9\%$) the films grown on this substrate have lattice parameter and physical properties similar to bulk samples. Gommert et al [34] have shown that the strain is released within 2 nm of the interface by additional lattice planes, and after that the film grows with few defects and little strain.

All films are deposited by pulsed laser deposition using a KrF Excimer laser. The magnetic and transport properties of the films are strongly dependent on the deposition procedure. In order to make a consistent study of the film properties we chose three variables, the substrate temperature during deposition, the background pressure and the laser fluence. All other experimental variables were kept constant for all samples studied and their values are given in the table below.

Pulse length	laser wavelength	Repetition rate	target-substrate distance
22 ns	248 nm	10 Hz	3.5 cm

(16)

The substrates are MgO (001) single crystals polished on one side only. Before deposition the substrate is washed with acetone and dried using a nitrogen gun making sure that there are no spots left on the surface. The substrate is then glued to the heating plate using a small drop of silver paste which should be allowed to dry until solid. At this stage the chamber can be closed and pumped. Once a pressure of 10^{-5} mbar is reached the chamber can be prepared for deposition. A needle valve allows the introduction and pressure control of a background gas that in the present study is high purity O_2. The substrate temperature can be adjusted by passing and AC current through the heating elements that can be monitored with an ampmeter. Care should be taken in order not to exceed the maximum recommended voltage of 110 V for each heater. For the present configuration, with two heaters connected

in series, this corresponds to a maximum current of 0.6 A. The substrate temperature is measured using an infrared pyrometer with $\varepsilon = 0.4$ for the emissivity of MgO. The substrate temperature measured in this way will be consistent, with a relative error of 2^oC but may have a systematic absolute error of up to 40^oC due to uncertainty in the emissivity of MgO. Once the pressure and substrate temperature have stabilised in the desired values, deposition is started by switching on the laser. The growth of the films is monitored using a reflectivity apparatus with a He-Ne laser ($\lambda = 680$ nm) directed at the substrate at a 30^o incidence angle. The periodic curve obtained this way can be fitted to obtain the film thickness. Here, this system is used to ensure all films have the same thickness by stopping the deposition once the first reflectivity peak is reached. After deposition the connection to the pumping system is closed, the O_2 pressure is increased to 1 bar while the sample is slowly cooled to room temperature.

3.3 Search for the optimum deposition conditions

The values shown in table (16) have been previously used for the deposition of superconducting $YBa_2Cu_3O_7$ and the manganite $(La_{0.7}Ca_{0.3})MnO_3$ [27]. In order to find the optimum deposition conditions we vary the laser fluence, background oxygen pressure and substrate temperature. The structural properties of films deposited under different conditions are studied using x-ray diffraction. Further characterisation is provided by measuring resistivity as a function of temperature and MOKE at room temperature.

The target used here is a single phase, stoichiometric $(La_{0.7}Sr_{0.3})MnO_3$ ceramic with a lattice parameter $c = 3.875$ Å an pressed into a pellet of 13 mm diameter. In-situ growth of ferromagnetic oxide thin films by PLD requires the presence of a background oxygen pressure during deposition. The effect of this reactive gas is to scatter and attenuate the plume of

material ejected from the target; thus reforming oxides, and thermalising the ions and atoms present in the plume [28]. The deposition of films requires delicate adjustment of gas pressure and laser fluence to ensure formation of the correct phase, provide an adequate deposition rate and limit the incident kinetic energies. To this end, a biased Langmuir probe is used for a pre-deposition check of the kinetic energy of the species present in the plume. The temporal variation of the ion current in vacuum is shown in Figure 3.1 a) for a fluence of 2 Jcm^{-2} and a distance between target and probe of 3.5 cm. The ion dose arriving at the

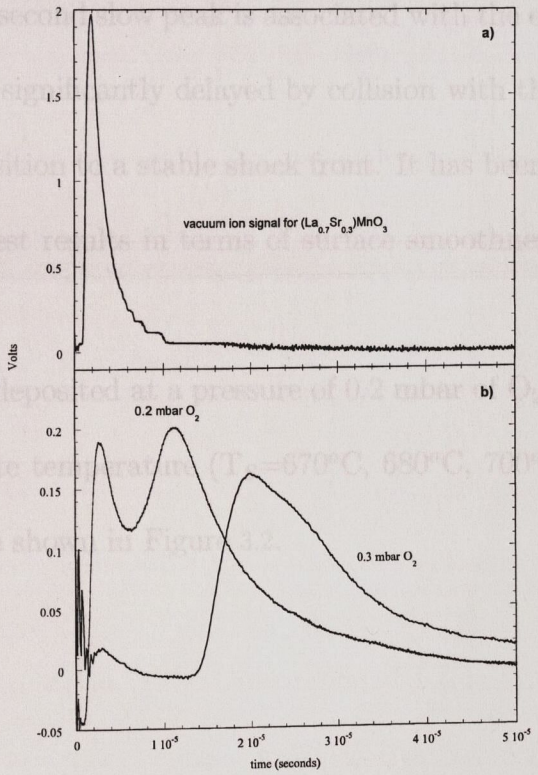


Figure 3.1.Ion signal of $(La_{0.7}Sr_{0.3})MnO_3$ in a) vacuum and b) 0.2 and 0.3 mbar of O_2 background pressure.

Langmuir probe can be calculated using the formula

$$\text{Ions } (\text{cm}^{-2}) = \frac{R}{A(cm^2) \times e} \int V dt \tag{17}$$

where R is the value of the resistor in the probe, A is the area of the probe and e is the charge

of the electron. In this case the ion dose is 2.24×10^{15} cm^{-2}. When the oxygen background pressure is increased it has several visible effects. The plume fluoresces brightly at the edges due to increased collision rates and the reactive gas oxidises the metallic species in the plume [29]. The maximum extent of the plume is attenuated, the amount of material penetrating the background gas is greatly reduced and the ion signal develops a second slower peak. This is shown in figure 3.1b) for a laser fluence of 2 Jcm^{-2} and an oxygen pressure of 0.2 and 0.3 mbar. The first peak is due to ions transmitted through the gas without collisions and so with little delay while the second slow peak is associated with the expansion of a cloud of gas that has been heated and significantly delayed by collision with the primary laser produced plasma undergoing a transition to a stable shock front. It has been shown that this shape of the ion signal gives the best results in terms of surface smoothness and texture of the film [27] [30].

A series of four films was deposited at a pressure of 0.2 mbar of O_2 and a fluence of 2 Jcm^{-2} while varying the substrate temperature (T_S=670°C, 680°C, 700°C and 720°C). The x-ray patterns for this series are shown in Figure 3.2.

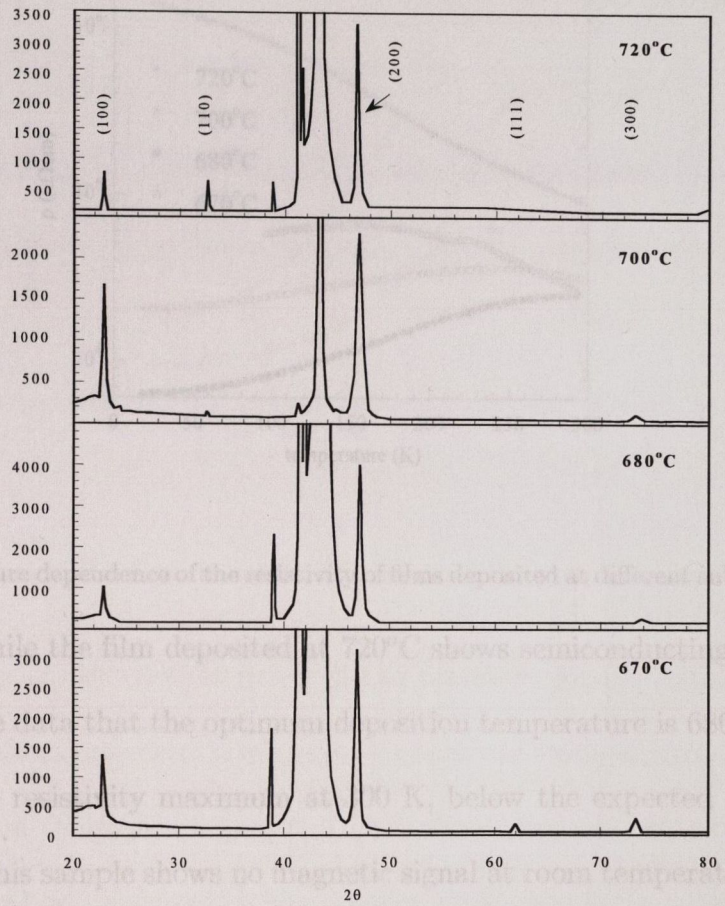


Figure 3.2. X-ray diffraction patterns of LSMO films deposited in 0.2 mbar O_2.

The main feature of these patterns is the appearance of a small fraction of a (110) peak for temperatures above 680°C and a (111) peaks at 670°C. The resistivity measured as a function of temperature for the four films is shown in Figure 3.3. The resistivity of the film deposited at 680°C has a maximum at 300K showing metallic behaviour at lower temperatures with ρ=6mΩcm at 15K, the minimum value obtained in this series. For the film deposited at 670°C there is an increase in the value of resistivity (20 mΩcm at 15 K) and a shifting of the resistivity peak to 240 K. For temperatures above 680°C there is a more dramatic change in the resistivity of the films. The film deposited at 700°C shows a very broad resistivity peak

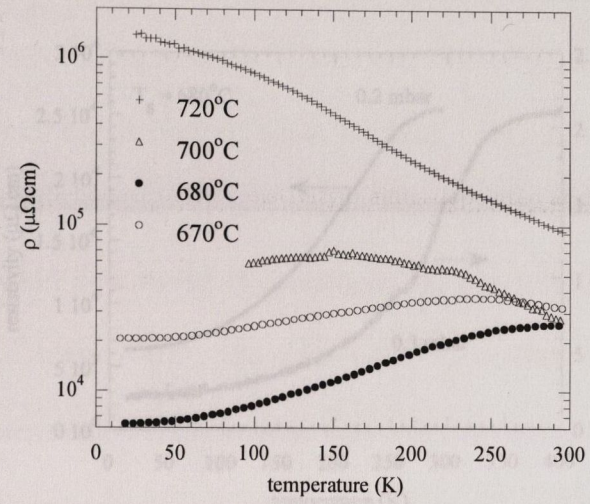


Figure 3.3. Temperature dependence of the resistivity of films deposited at different substrate temperatures.

centred at 150 K while the film deposited at 720°C shows semiconducting behaviour.

It is clear from these data that the optimum deposition temperature is 680°C. However, this film clearly shows a resistivity maximum at 300 K, below the expected 370 K for LSMO. MOKE analysis of this sample shows no magnetic signal at room temperature. A lowering of the resistivity peak has been associated with either the presence of grain boundaries or and oxygen deficient stoichiometry. The formation of grain boundaries depends on the substrate temperature, but also on the rate of arrival of atoms so a possibility to improving film quality could be to reduce the laser fluence or increase the background pressure. An oxygen deficient stoichiometry could be corrected by increasing the background oxygen pressure [28].

A film was deposited using a substrate temperature of 680°C, a fluence of 2 Jcm^{-2} and an increased O_2 pressure of 0.3 mbar. X-ray diffraction data in the $\theta - 2\theta$ mode show only (00l) reflections. The resistivity is plotted together with that of the film deposited at 0.2 mbar and is shown in Figure 3.4. The increased O_2 pressure shifts the resistivity peak to approximately 400 K and decreases the resistivity by one order of magnitude (200 $\mu\Omega cm$ at

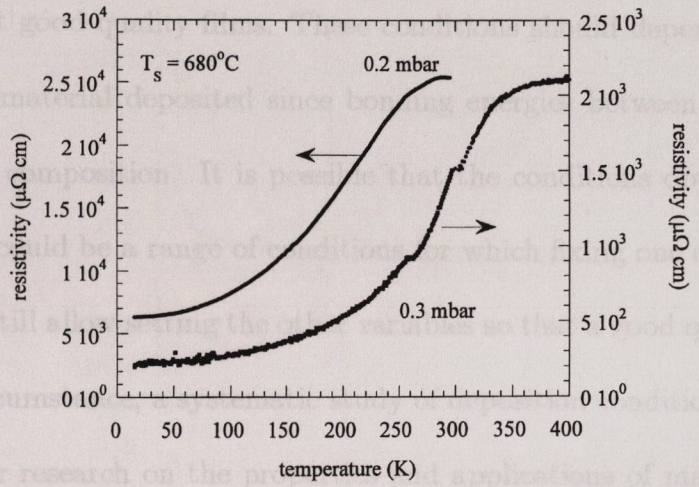


Figure 3.4.Resistivity of LSMO films deposited at the same substrate temperature in 0.2 and 0.3 mbar of O_2.

15 K). This value is similar to that found in the literature for epitaxial thin films of this material [31] [2]. Further confirmation of the good quality of this sample is given by a MOKE measurement at room temperature (figure 3.5) showing a square hysteresis loop typical of magnetisation reversal of a single magnetic domain.

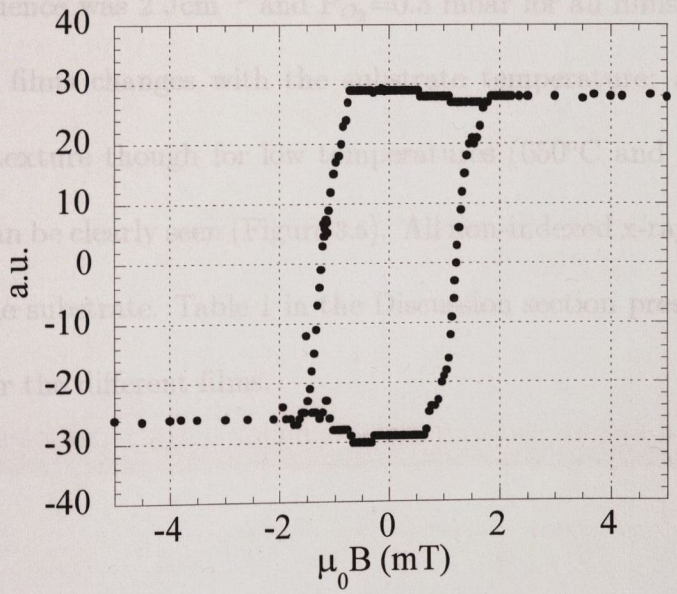


Figure 3.5.MOKE hysteresis loop of film deposited at T_S=680°C and P=0.3mbar of O_2.

The above results show that there is a narrow window of deposition conditions over which it is possible to deposit good quality films. These conditions should depend on the substrate being used and the material deposited since bonding energies between film and substrate depend on chemical composition. It is possible that the conditions obtained here are not absolute i. e., there could be a range of conditions for which fixing one of the variables in a chosen value would still allow setting the other variables so that a good quality film could be obtained. In any circumstance, a systematic study of deposition conditions is needed before proceeding to deeper research on the properties and applications of manganese perovskite thin films.

3.4 Influence of substrate temperature

With the results of the previous section we can proceed to study the properties of $(La_{0.7}Sr_{0.3})MnO_3$ films as a function of substrate temperature. Five films with thickness of 60 nm were deposited at the following five substrate temperatures (T_S): 650^oC, 660^oC, 670^oC, 680^oC and 690^oC. The laser fluence was 2 Jcm^{-2} and P_{O_2}=0.3 mbar for all films.

The texture of the films changes with the substrate temperature; all films grow with a predominant (00l) texture though for low temperatures (650°C and 660°C) the (011) and (111) orientations can be clearly seen (Figure 3.6). All non-indexed x-ray peaks in this chapter are originated by the substrate. Table 1 in the Discussion section presents the values of the lattice parameter for the different films.

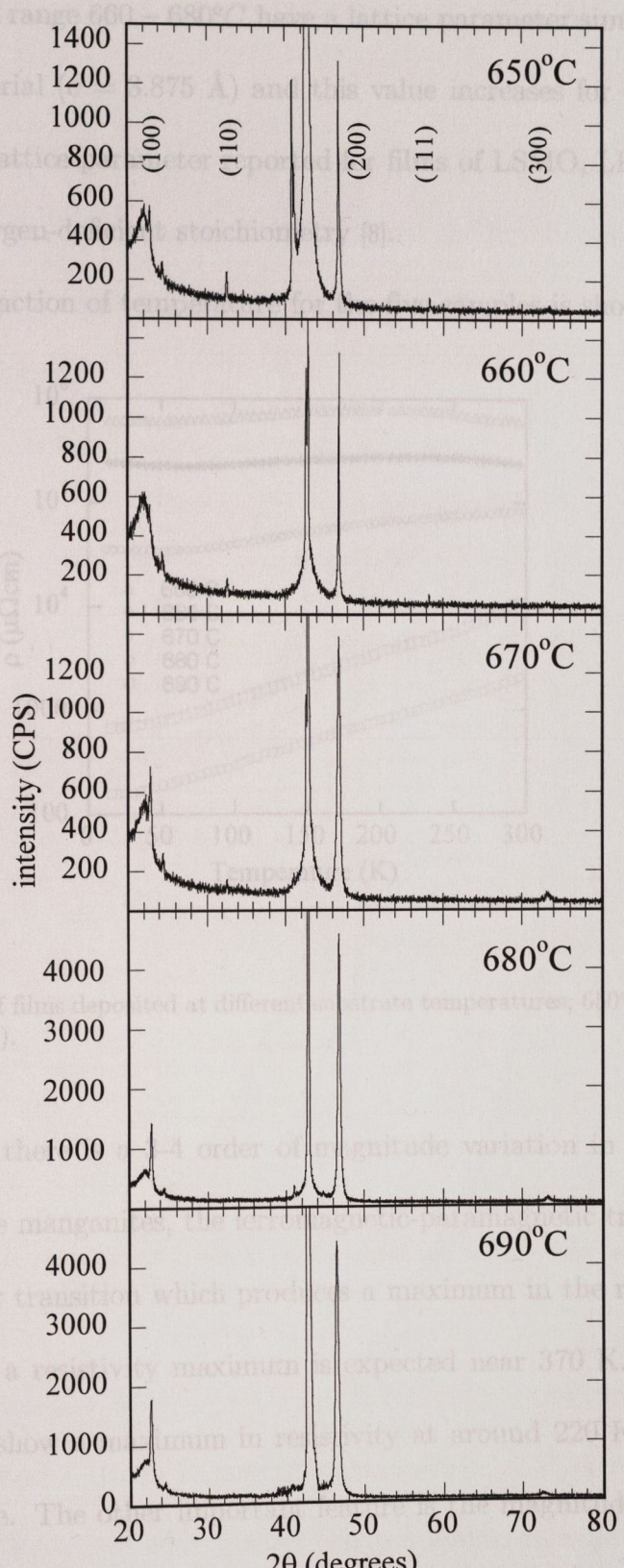


Figure 3.6. X-ray diffraction patterns of films deposited at different substrate temperatures.

Films deposited in the range $660 - 680^oC$ have a lattice parameter similar to that measured for bulk ceramic material ($c = 3.875$ Å) and this value increases for the film deposited at 690°C. An expanded lattice parameter reported for films of LSMO, LBMO and LCMO has been related to an oxygen-deficient stoichiometry [8].

The resistivity as a function of temperature for the five samples is shown in Figure 3.7.

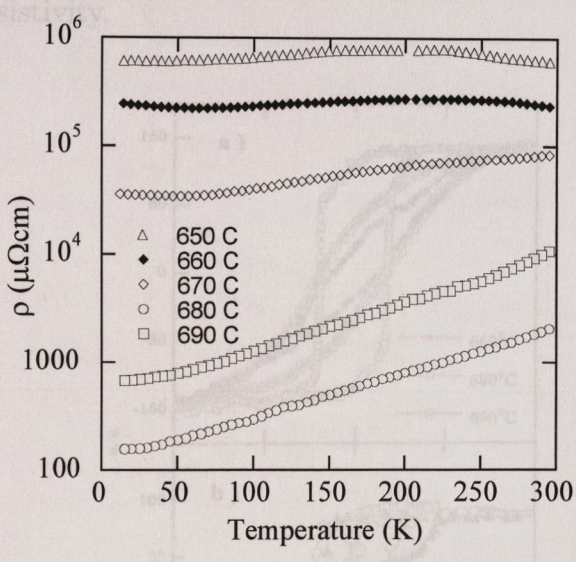


Figure 3.7.Resistivity of films deposited at different substrate temperatures; 650°C (•), 660°C (□), 670°C (■), 680°C (◇), 690°C (♦).

It is remarkable that there is a 3-4 order of magnitude variation in the resistivity of the deposited films. In the manganites, the ferromagnetic-paramagnetic transition is correlated with a metal-insulator transition which produces a maximum in the resistivity near T_C, so in the case of LSMO a resistivity maximum is expected near 370 K. The films deposited at 650^oC and 660^oC show a maximum in resistivity at around 220 K which is well below the Curie temperature. The other important feature is the magnitude of the resistivity at low temperatures. It decreases with increasing substrate temperature reaching a minimum of 200 $\mu\Omega cm$ for the film deposited at 680^oC and increases again for the film deposited at

690^oC. The sample deposited at 680°C is the only one whose resistivity approaches the metallic value of 150 $\mu\Omega cm$ [32].

MOKE measurements at room temperature are shown in Figure 3.8a). All the films present similar values for the coercivity (around 2 mT) but just the film deposited at 680^oC shows a square loop reaching saturation at an applied field of 4 mT. This is also the film that shows the lowest value of resistivity.

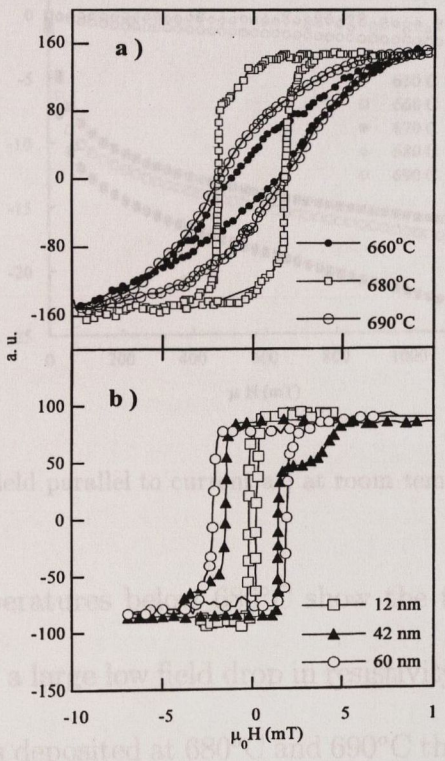


Figure 3.8. a) MOKE at room temperature for films deposited at different substrate temperatures, b) Moke at room temperature for films with different thicknesses.

Magnetoresistance, defined as $MR(\%) = (R_H - R_0)/R_0$, was measured for the five samples at room temperature and 77 K. In Figure 3.9 we present the MR at room temperature and 77 K for the five films measured with applied field parallel to current.

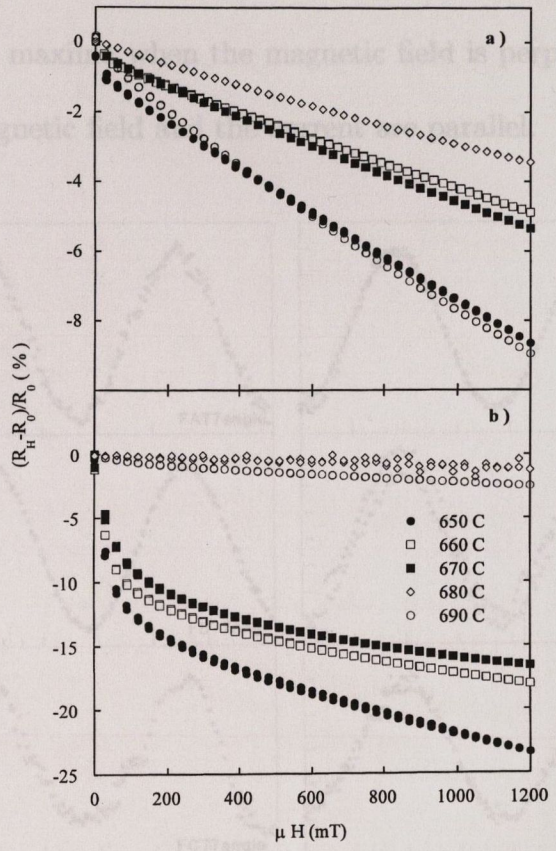


Figure 3.9. MR with field parallel to current a) at room temperature and b) at 77 K.

The films deposited at temperatures below 680°C show the typical MR loop obtained for polycrystalline samples, with a large low field drop in resistivity followed by a linear decrease for fields above 0.2 T. In films deposited at 680°C and 690°C the resistivity decreases linearly with field similar to what happens in a single crystal. The MR dependence on the angle between applied current and magnetic field was also measured in order to determine the anisotropic magnetoresistance. The anisotropic component is defined as $AMR = (R_{\|} - R_{\perp})/R_{ave}$ where $R_{\|}$ and $R_{\perp}$ are the resistance with magnetic field parallel and perpendicular to the current respectively and $R_{ave} = (1/3)R_{\|} + (2/3)R_{\perp}$. $R_{\|}$ and $R_{\perp}$can be obtained by a plot of the film resistance as a function of the field direction as shown in Figure 3.10. The

field is rotated in the plane of the film with a constant amplitude of 1.2 T. The resistance curves of Figure 3.10 have maxima when the magnetic field is perpendicular to the current and minima when the magnetic field and the current are parallel.

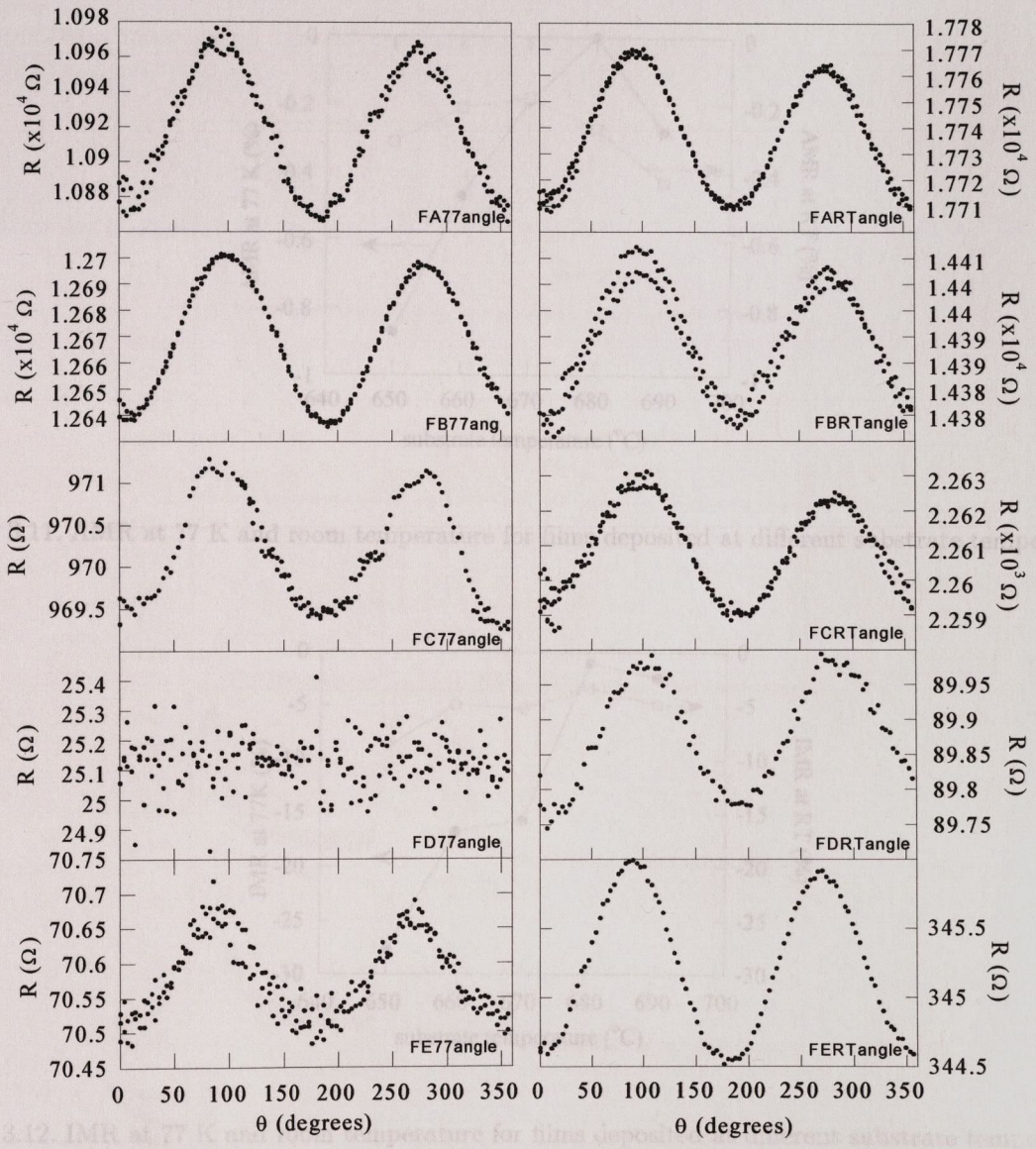


Figure 3.10. Field direction dependence of the resistance of LSMO films at 77 K (left) room temperature (right). The substrate temperature varies from 650°C (top row) to 690°C (bottom row).

The minimum (maximum) value of resistance in that curve corresponds to a configuration with applied field parallel (perpendicular) to the current direction. The MR isotropic com-

ponent is defined as as $IMR = (1/3)MR_{\parallel} + (2/3)MR_{\perp}$. The maximum AMR and IMR ratios (for $\mu_0 H = 1.2$ T) at room temperature and 77 K are shown in Figures 3.11 and 3.12 respectively.

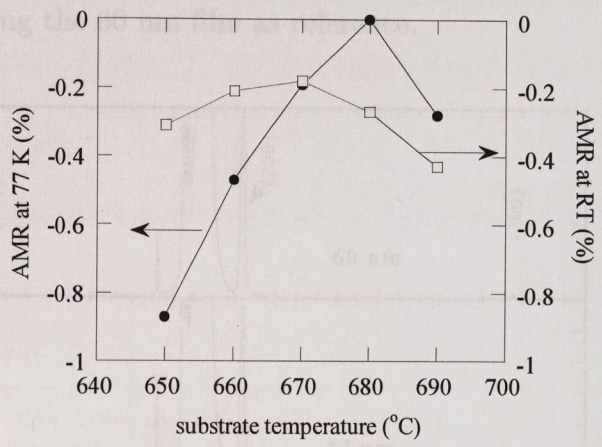


Figure 3.11. AMR at 77 K and room temperature for films deposited at different substrate temperatures.

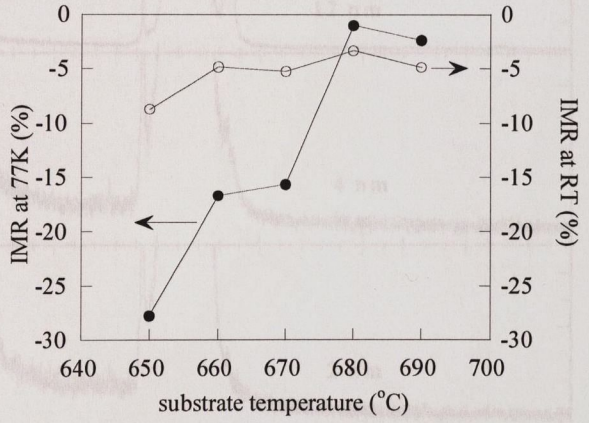


Figure 3.12. IMR at 77 K and room temperature for films deposited at different substrate temperatures.

IMR follows the expected trend, i.e. it is minimised for the film with less grain boundaries. Furthermore, it is much larger at low temperatures as observed previously. AMR, an intrinsic property of the material, shows an unexpected variation with microstructure, similar but much smaller than the isotropic component.

3.5 Influence of film thickness

Six samples with thicknesses of 60, 42, 12, 4, 2 and 1 nm were deposited at the optimum substrate temperature of 680°C. The thickness was calculated assuming a linear increase with deposition time using the 60 nm film as reference.

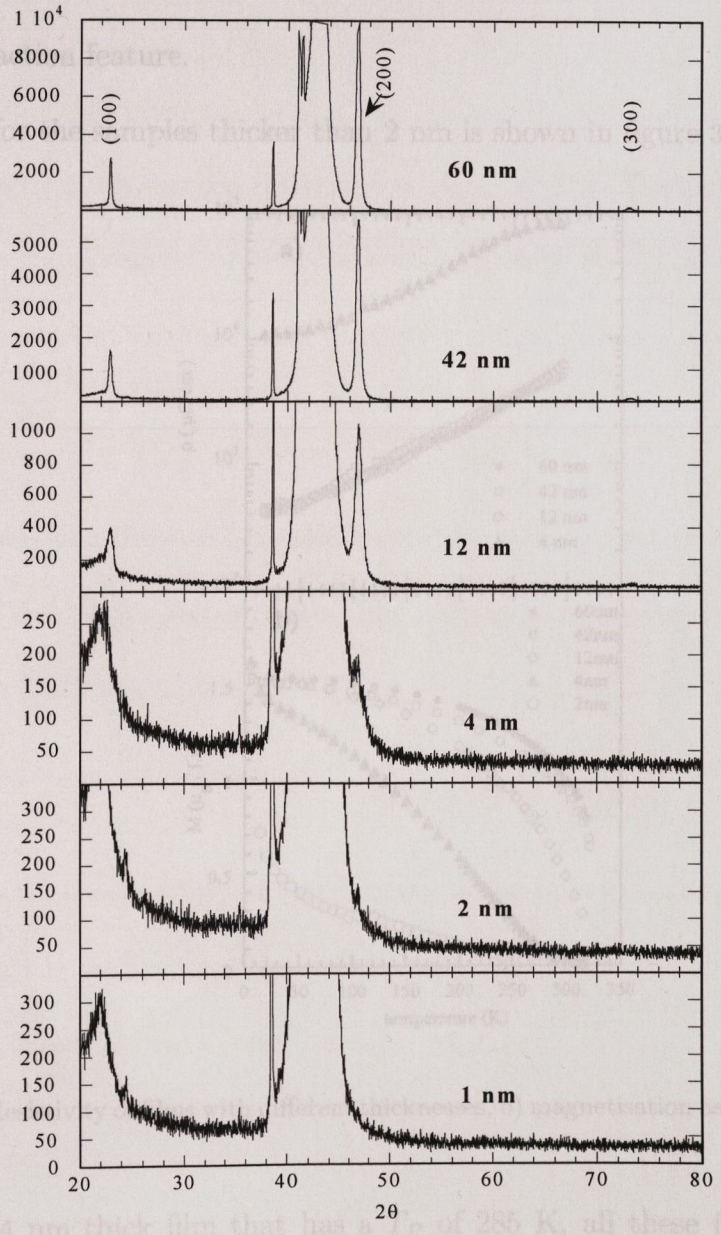


Figure 3.13. $\theta - 2\theta$ diffraction pattern of LSMO films with different thicknesses deposited on MgO.

The final thickness was checked for the four thickest films by x-ray reflectivity measured at CEA, Saclay and is in good agreement with the predicted values. As the film thickness decreases we see some broadening of the X-ray (00l) peaks as well as a decrease in intensity (Figure 3.13). The lattice parameter has a value of approximately 3.875 nm (the bulk value) for all except the thinnest film (Table 1). The 1 nm thick film does not exhibit any measurable manganite diffraction feature.

The resistivity for the samples thicker than 2 nm is shown in figure 3.14a).

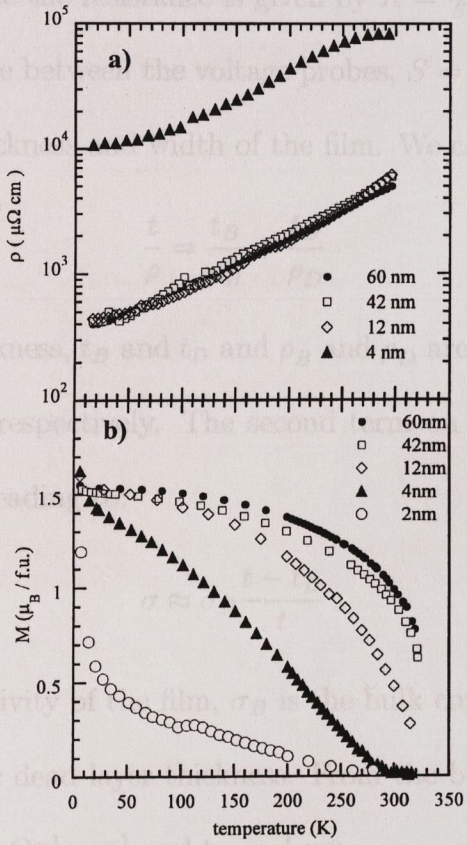


Figure 3.14. a) Resistivity of films with different thicknesses, b) magnetisation as a function of temperature.

Except for the 4 nm thick film that has a T_P of 285 K, all these films have a resistivity peak above room temperature. The striking feature of these curves is the fact that the resistivity is almost constant for the three thickest films; it increases for the 4 nm film with

thinner films being non conducting. A plot of the conductivity (Figure 3.15) as a function of film thickness at 15 K can be fitted by a model that considers two parallel resistors: one with high resistance corresponding to the film interfaces and the other with low resistance corresponding to the bulk of the film. One can write

$$\frac{1}{R} = \frac{1}{R_B} + \frac{1}{R_D} \tag{18}$$

where R is the total resistance of the film and R_B and R_D are the resistance of the bulk and dead layer respectively. Since the resistance is given by $R = \frac{\rho l}{S}$ where ρ is the resistivity of the material, l is the distance between the voltage probes, $S = tL$ is the cross section of the film and t and L are the thickness and width of the film. We can now write

$$\frac{t}{\rho} = \frac{t_B}{\rho_B} + \frac{t_D}{\rho_D} \tag{19}$$

where t is the total film thickness, t_B and t_D and ρ_B and ρ_D are the thickness and resistivity of the bulk and dead layer respectively. The second term on the right hand side is small compared to the first term leading to:

$$\sigma \approx \sigma_B \frac{t - t_D}{t} \tag{20}$$

where σ is the total conductivity of the film, σ_B is the bulk conductivity, t is the total film thickness and t_D the electric dead layer thickness. From the best fit to the data we obtain the values $\sigma_B = 2.76 \times 10^{-3}$ $\mu\Omega^{-1}\text{cm}^{-1}$ and $t_D = 4$ nm.

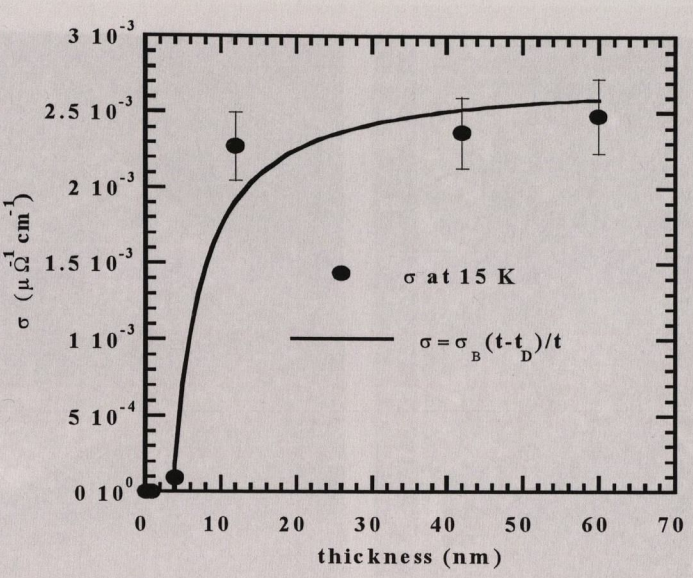


Figure 3.15. Fit of the conductivity at 15K of the films with different thicknesses using equation 5.

To check whether the insulating behaviour of the thinner films might be due to discontinuities that could arise from an island-like growth mode, the surface roughness of the films was investigated by white light interferometry and AFM. Values obtained were in the range 0.5 - 1.3 nm, similar to that obtained for the substrate. The 1 nm film is probably discontinuous but the measured value of 0.5 nm for the peak to valley roughness over an area of $1700nm \times 1800nm$ eliminates film discontinuity as the cause of the insulating behaviour for the 2 nm film (Figure 3.16).

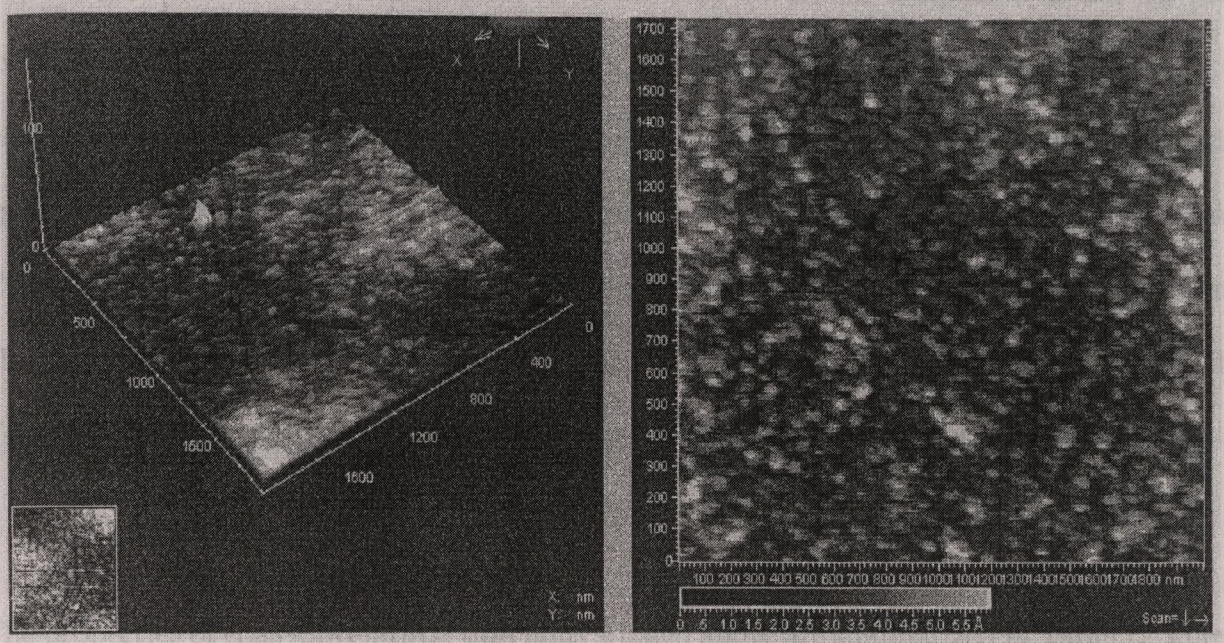


Figure 3.16. AFM scan on the 2 nm film showing a peak to valley roughness of 0.5 nm.

In Figure 3.8b) we showed the magnetic hysteresis measured at room temperature by MOKE. Only the three thickest films show a Kerr signal. All of them exhibit a square hysteresis loop as found in the previous section for the film deposited at the optimum temperature but there is evidence for two sorts of magnetic regions with different coercivities and there is a decrease in the value of coercivity as the thickness decreases.

The magnetisation data measured with the SQUID were corrected for the diamagnetism of the MgO substrates and the paramagnetism of S = 2 impurities. All substrates come from the same batch. The impurity concentration in MgO was found to be $9 \times 10^{24}\ m^{-3}$. The corrected magnetisation curves for the 60 nm film at three temperatures are shown in Figure 3.17. There is a readily saturatable component, in agreement with the MOKE data but at 5 K there appears a component that approaches saturation only slowly. The expected moment for LSMO is 3.7 μ_B per formula unit but this is rarely achieved [2] with a typical bulk value

of 3.5 μ_B per formula unit. The moment of the easy saturated component is 2.3 μ_B per formula unit hence 66 % of the 60 nm film is a soft ferromagnet.

Magnetisation was measured as a function of temperature for all the films with a small applied field of 8 mT (Figure 3.14b)). The thicker films behave very similarly to bulk samples. The magnetisation falls more rapidly as the film thickness is decreased and for the thinnest films (2 nm and 1 nm) only at low temperatures a ferromagnetic signal can be detected. There is a striking similarity between these data and the data presented in Reference [19].

3.6 Discussion

The properties of $(La_{0.7}Sr_{0.3})MnO_3$ thin films studied above are summarized in Table 1. They are strongly dependent on preparation conditions which have to be systematically studied and optimised if working devices based on this material are to be fabricated.

	T_S (°C)	P_{O_2} (mbar)	thickness (nm)	lattice parameter (Å) ±0.001 Å	ρ_{15K} ($\mu\Omega$ cm)	T_P (K)	T_C (K)
section 3.3	670	0.2	60	3.894	2×10^4	240	below RT
	680	0.2	60	3.901	6000	300	below RT
	680	0.3	60	3.880	200	~400	below RT
	700	0.2	60	3.893	4×10^4	150	below RT
	720	0.3	60	3.905	1.5×10^6	-	below RT
section 3.4	650	0.3	60	3.863	8×10^5	190	above RT
	660	0.3	60	3.874	3×10^5	210	above RT
	670	0.3	60	3.874	5×10^4	above RT	above RT
	680	0.3	60	3.874	200	above RT	above RT
	690	0.3	60	3.912	800	above RT	above RT
section 3.5	680	0.3	60	3.877	400	above RT	350
	680	0.3	42	3.872	400	above RT	350
	680	0.3	12	3.875	400	above RT	350
	680	0.3	4	3.882	10^4	220	290
	680	0.3	2	3.874	-	-	290
	680	0.3	1	-	-	-	290

Table1.Summary of the properties of LSMO thin films deposited on MgO substrates.

The search for the optimum deposition conditions was described in section 3.3. Figure 3.4

shows that an increase in the background oxygen pressure from 0.2 to 0.3 mbar can greatly improve the magnetic and transport properties. A higher pressure can reduce the deposition rate allowing a better arrangement of the atoms in the lattice, but this mechanism must play a minor role given the absence of any significant difference in the x-ray patterns of the two films. The data suggest that the films deposited in an O_2 pressure of 0.2 mbar are oxygen deficient. A shift to lower temperatures of the resistivity peak or even insulating behaviour in conjunction with an expanded lattice parameter in oxygen deficient films has been observed for LSMO [33], LCMO [34] and LBMO [35]. With increasing oxygen deficiency, the average manganese oxidation state decreases, which is equivalent to a lowering of the dopant concentration x. This could explain the decrease in T_C and the observed resistivity curves. The oxygen vacancies also lead to an expansion of the lattice parameter [8]. A study of the kinetics of oxidation of $(La_{0.67}Ba_{0.3})MnO_3$ thin films using an oblique-incidence optical reflectance difference technique shows that oxygen absorption by the film is very slow [36] with the full oxidation of a single monolayer taking up to one hour. The oxygen stoichiometry of the films must be determined primarily by reaction of the ionic species of the plume with the background gas rather than absorption by the deposited film. Another effect to be taken into account is that due to the presence of grain boundaries. The existence of (110) and (111) reflections in Figure 3.2 indicates the polycrystalline nature of these films. Polycrystalline ceramic samples of LSMO show metallic behaviour although with higher values of resistivity than single crystals. However as the grain size is reduced, the contribution of the surface layers of the grains start dominating transport [19] (the nature of these layers will be discussed below). In polycrystalline thin films, the average grain size should be of the order of the film thickness which is 60 nm in the present case. A low temperature resistivity peak is

observed in Reference 12 for ceramics with grain size smaller than 300 nm. In our samples, oxygen deficiency and granularity combine to produce the observed deviations from metallic behaviour.

Once the optimal conditions are found we can proceed to isolate the effect of a single deposition variable, in this case the substrate temperature. Film quality is strongly dependent on the substrate temperature during deposition and good quality films can be deposited at the optimum temperature of 680°C. These films are well textured showing only (00l) reflections. They show no granular (low field) magnetoresistance at 77 K unlike those deposited at lower temperatures. A deviation from this optimum temperature leads to an increase in the number of grain boundaries and therefore to an increase in the resistivity of the films as well as a shift of the resistivity peak to lower temperatures. The polycrystalline nature of the films with $T_S \neq 680°C$ is evident from the different plane orientations observed in the x-ray patterns. The 680°C film exhibits a typical single-domain hysteresis loop at room temperature whereas the others are multidomain. The 690°C film shows only (00l) x-ray reflections but its MOKE loop is similar to the other polycrystalline films. The magnetoresistance of this film has a linear dependence in field like the single crystal film, although with a larger slope. This could be due to misorientations in the ab plane that are not visible in a $\theta - 2\theta$ scan. The fact that the low temperature AMR is not constant for all films suggests that this quantity might not be intrinsic as proposed by Ziese [37]. The model proposed by this author considers the AMR to be dependent on Δ_{CF} (the crystal field splitting) and H_{ex} (the exchange-coupling energy). However, given that the grain boundaries are disordered, the values of Δ_{CF} and H_{ex} could change significantly. The films with higher resistivity also show quite high values of MR. This is reasonable since the largest contribution comes

from grain boundary magnetoresistance (or IMR). Using the value of 5×10^{-6} Ω cm^2 for the grain boundary resistivity of LSMO [38] and supposing a grain size of 0.1 μm (the order of magnitude of the film thickness), we estimate the resistance of a single grain boundary to be 5×10^4 Ω. Therefore, the intergranular resistance is much larger than the intrinsic resistance of the single crystal and indicates that both resistivity and magnetoresistance will be dominated by the grain boundary contribution.

Our resistivity measurements on films deposited at the optimum temperature with different thicknesses indicate that the conduction is not homogeneous throughout the films. The existence on an electrical 'dead' layer of about 4 nm total thickness on all films can be deduced from a plot of conductivity against film thickness (Figure 3.15). These data were fitted with a simple model based on two parallel resistors. The question arises whether the dead layer is just at the interface or at the free surface, or both. The dead layer may be associated with structural disorder at least at the level of the interface between film and substrate. It is known that due to the large lattice mismatch between LCMO and MgO the first few layers grow with very poor crystalline quality in the first 2 nm but the rest of the film shows properties very similar to bulk samples [34]. This indicates that the strain due to film/substrate lattice mismatch is released in a thickness which is less than the dead layer thickness. Since the thickness of the interface layer is constant we could in fact see a decrease in the total conductance of the film as the thickness of the good layer decreases (Figure 3.15). The electrical dead layer is likely to be present at the free surface, as well as the substrate/film interface, because the Mn atoms there are missing up to half their Mn-O neighbours, which will decrease the e_g bandwidth. This electric dead layer works as a tunnel barrier for spin dependent tunnelling across grain boundaries. It is interesting that a similar

dead layer is obtained in films grown on $LaAlO_3$ and $NdGaO_3$ substrates [18] which have a much better lattice match with LSMO than MgO.

Isothermic magnetisation curves taken at 290 K, 80 K and 5 K for the 60 nm film are shown in Figure 3.17. At 80 K and 290 K the magnetisation saturates easily in a field of 0.2 T. At 5 K a component appears that slowly increases and approaches saturation but only at fields of around 6 T. In order to explain these data we consider the films to be divided in three zones; the central part of the film and the film/substrate and film/air interfaces.

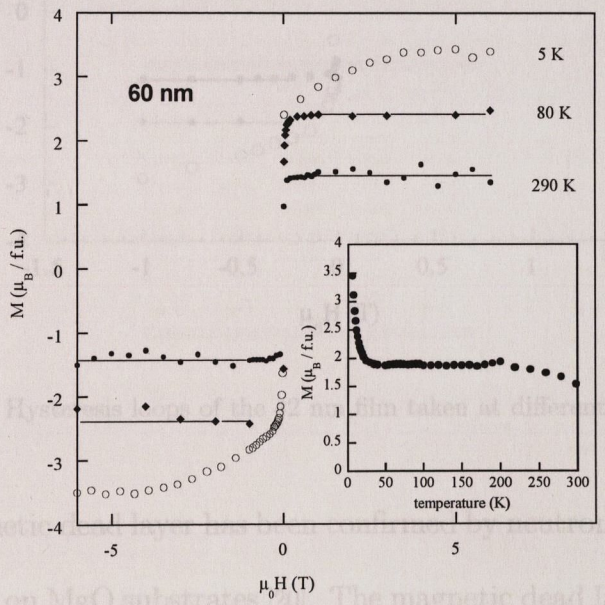


Figure 3.17. Hysteresis loops of the 60 nm film taken at different temperatures. The inset shows the temperature dependence of the magnetisation in a field of 3 Tesla.

The central part can be easily magnetised and represents around 60 % (37 nm) of the film thickness while the two interfaces (23 nm) consist of weakly coupled noncolinear spins with magnetisation falling off more rapidly than the central part as can be seen in Figure 3.14b). The volume fraction of the central part is obtained from Figure 3.17 as the ratio of the magnetic moment extrapolated from low temperature data in 0.2 T to the bulk saturation moment ($3.7\mu_B$/ f.u.). The temperature dependence of the magnetisation of the central

zone and the surfaces can be seen in the inset to Figure 3.17 from a measurement at 3 Tesla. Magnetisation data on the 42 nm film (Figure 3.18) show that the central part represents 48 % (20 mn) and the dead layers 52% (22 nm) of the film thickness, in agreement with the above calculation for the 60 nm film.

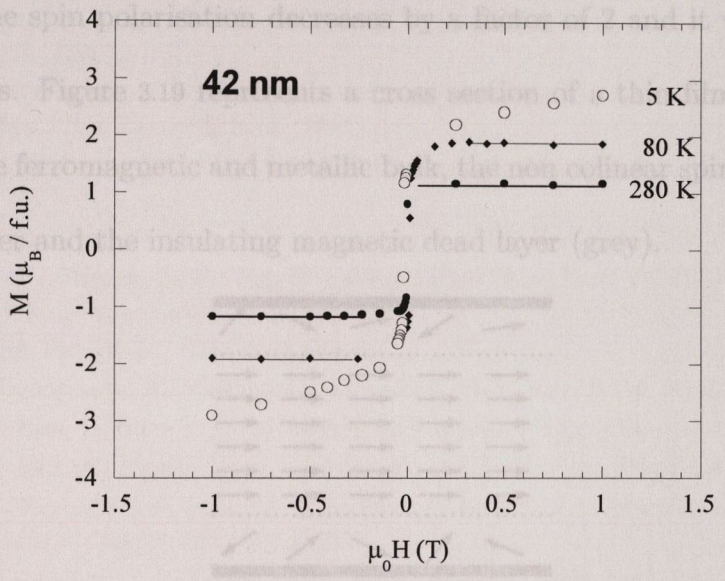


Figure 3.18. Hysteresis loops of the 42 nm film taken at different temperatures.

The existence of a magnetic dead layer has been confirmed by neutron diffraction on a similar series of films deposited on MgO substrates [20]. The magnetic dead layer appears as a region of depressed magnetisation at both interfaces.

The magnetic dead layer is notably thicker than the electric dead layer. This conducting magnetic dead layer will contribute to the spin dependent scattering at the interfaces between grain boundaries. It is metallic with weakly coupled non-colinear spins. The non colinear spins at the interface layers are due to lower effective magnetic coupling caused by the surface termination of the crystal structure [39]. The hopping electron is strongly coupled to these surface spins by the large on-site J_H, which explains the fast degradation of TMR with increasing temperature observed by other authors.

The insulating magnetic dead layer provides disordered spins in the tunnel barrier which contribute to the spin depolarization. In a related system, it has been demonstrated that the presence of a conducting non-magnetic (Cu) layer at the interfaces of $Co/Al_2O_3/Co$ tunnel junctions has a major effect on the spin polarisation [40]. With only one Cu monolayer at the interface the spin polarisation decreases by a factor of 2 and it vanishes completely for five monolayers. Figure 3.19 represents a cross section of a thin film showing the three different areas: the ferromagnetic and metallic bulk, the non colinear spins at the conducting magnetic dead layer and the insulating magnetic dead layer (grey).

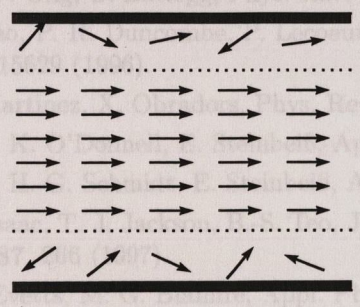


Figure 3.19. Schematic representation of the dead layers in a LSMO thin film.

In conclusion, we have investigated the dependence of magnetic and transport properties of LSMO thin films on the deposition conditions. The existence of electric and magnetic 'dead' layers at the interfaces of thin LSMO films has also been demonstrated. The electric dead layer works as a tunnel barrier while the magnetic dead layer works as a spin scattering region. Our results point to the importance of controlling magnetic disorder at the interface if half metallic oxides are to be effectively incorporated in thin film devices. If the dead layers are an intrinsic feature of these materials then their application in devices such as non-volatile memories would not be feasible.

References

[1] R. von Helmolt, J. Wecker, B. Holzapfel, L. Schultz, K. Samwer, Phys. Rev. Lett. **71**, 2331 (1993).

[2] J. M. D. Coey, M. Viret, S. von Molnár, Adv. Phys. **48** (2), 167 (1999).

[3] M. Viret, M. Drouet, J. P. Contour, J. Nassar, C. Fermont, A. Fert, Europhys. Lett. **39**, 545 (1997).

[4] R. J. Soulen Jr, J. M. Byers, M. S. Osofsky, B. Nadgorny, T. Ambrose, S. F. Cheng, P. R. Broussard, C. T. Tanaka, J. Nowak, J. S. Moodera, A. Barry, J. M. D. Coey, Science **282**, 85 (1998).

[5] J.-H. Park, E. Vescovo, H.-J. Kim, C. Kwon, R. Ramesh, T. Venkatesan, Nature **392**, 794 (1998).

[6] Y. Lu, X. W. Li, G. Q. Gong, G. Xiao, A. Gupta, P. Lecoeur, J. Z. Sun, Y. Y. Wang, V. P. Dravid, Phys. Rev. B **54**, R8357 (1996).

[7] J. Z. Sun, W. J. Gallagher, P. R. Duncombe, L. Krusin-Elbaum, R. A. Altman, A. Gupta, Y. Lu, G. Q. Gong, G. Xiao, Appl. Phys. Lett. **69**, 3266 (1996).

[8] H.L. Ju, J.Gopalakrishnan, J.L. Peng, Qi Li, G.C. Xiong, T. Venkatesan, R.L. Green, Phys. Rev. B **51**, 6143 (1995).

[9] P. Schiffer, A. P. Ramirez, W. Bao, S.-W. Cheong, Phys. Rev. Lett. **75**, 3336 (1995).

[10] H. Y. Hwang, S.-W. Cheong, N. P. Ong, B. Batlogg, Phys. Rev. Lett. **77**, 2041 (1996).

[11] A. Gupta, G. Q. Gong, Gang Xiao, P. R. Duncombe, P. Lecoeur, P. Trouilloud, Y. Y. Wang, V. P. Dravid, J. Z. Sun, Phys. Rev. B **54**, R15629 (1996).

[12] Ll. Balcells, J. Fontcuberta, B. Martinez, X. Obradors, Phys. Rev. B **58**, R14697 (1998).

[13] K. Steenbeck, T. Eick, K. Kirsch, K. O'Donnell, E. Steinbeiß, Appl. Phys. Lett. **71**, 968 (1997).

[14] K. Steenbeck, T. Eick, K. Kirsch, H.-G. Schmidt, E. Steinbeiß, Appl. Phys. Lett. **73**, 2506 (1998).

[15] N. D. Mathur, G. Burnell, S. P. Isaac, T. J. Jackson, B.-S. Teo, J. L. MacManus-Driscoll, L. F. Cohen, J. E. Evetts, M. G. Blamire, Nature **387**, 266 (1997).

[16] S. P. Isaac, N. D. Mathur, J. E. Evetts, M. G. Blamire, Appl. Phys. Lett. **72**, 2038 (1998)

[17] J. E. Evetts, M. G. Blamire, N. D. Mathur, S. P. Isaac, B.-S. Teo, L. F. Cohen, J. L. MacManus-Driscoll, Philos. Trans. Roy. Soc. London A **356**, 1593 (1998).

[18] J.Z. Sun, D.W. Abraham, R.A. Rao, C.B. Eom, Appl. Phys. Lett. **74**, 3017 (1999).

[19] J.-H. Park, E. Vescovo, H.-J. Kim, C. Kwon, R. Ramesh, T. Venkatesan, Phys. Rev. Lett. **81**, 1953 (1998).

[20] F. Ott, M. Viret, R. P. Borges, R. Lyonnet, E. Jacquet, C. Fermon, J.-P. Contour, J. Magn. Magn. Mater. **211**, 200 (2000).

[21] A. Filippetti and W. E. Pickett, Phys. Rev. Lett. **83**, 4184 (1999).

[22] R. A. Rao, D. Lavric, T. K. Nath, C. B. Eom, L. Wu, F. Tsui, Appl. Phys. Lett. **73**, 3294 (1998).

[23] H. L. Ju, K. M. Krishnan, D. Lederman, J. Appl. Phys. **83**, 7073 (1998).

[24] J. Aarts, S. Freisem, R. Hendrikx, H. W. Zandbergen, Appl. Phys. Lett. **72**, 2975 (1998).

[25] E. S. Vlakhov, R. A. Chakalov, R. I. Chakalova, K. A. Nenkov, K. Dörr, A. Handstein, K.-H. Müller, J. Appl. Phys. **83**, 2152 (1998).

[26] E. Gommert, H. Cerva, J. Wecker, K. Samwer, J. Appl. Phys. **85**, 5417 (1999).

[27] Justin Lawler, PhD Thesis, Trinity College Dublin (1993).

[28] D. B. Chrisey, G. K. Hubler (Eds.), *Pulsed Laser Deposition of Thin Films, Ch. 5, Wiley, New York (1994).*

[29] D. B. Geohegan, Appl. Phys. Lett. **60** 2732 (1992).

[30] Duncan Cole, PhD. Thesis, Trinity College Dublin 1998.

[31] J. M. D. Coey, M. Viret, L. Ranno, K. Ounadjela, Phys. Rev. Lett. **75**, 3910 (1995).

[32] N. F. Mott, *Metal-insulator transitions, 2nd ed, Taylor & Francis, London (1999).*

[33] H. L. Ju, C. Kwon, Qi Li, R. L. Greene, T. Venkatesan, Appl. Phys. Lett. **65**, 2108 (1994).

[34] S. Jin, T. H. Tiefel, M. McCormack, R. A. Fastnacht, R. Ramesh, L. H. Chen, Science **264**, 413 (1994).

[35] G. C. Xiong, Qi Li, H. L. Ju, R. L. Greene, T. Venkatesan, Appl. Phys. Lett. **66**, 1689 (1995).

[36] X. D. Zhu, W. Si, X. X. Xi, Qi Li, Q. D. Jiang, M. G. Medici, Appl. Phys. Lett. **74**, 3540 (1999).

[37] M. Ziese and S. P. Sena, J. Phys.: Condens. Matter **10**, 2727 (1998).

[38] J. J. Versluijs, F. Ott, J. M. D. Coey, Appl. Phys. Lett. **75**, 1152 (1999).

[39] H. Y. Hwang, S.-W. Cheong, Nature **389**, 943 (1997).

[40] P. LeClair, H. J. M. Swagten, J. T. Kohlhepp, R. J. M. van de Veerdonk, W. J. M. de Jonge, Phys. Rev. Lett. **84**, 2933 (2000).

Chapter 4

Double Perovskites

4.1 Introduction

The Curie temperatures of mixed-valence manganites of the type $(R_{1-x}A_x)MnO_3$ cannot be increased above 400 K by any manipulation of the composition or stoichiometry [1]. The Curie temperature for CrO_2 is similar. Substantially higher Curie points are required if devices which rely on spin-polarized transport in half-metallic oxides are to operate in a practically-useful temperature range around room temperature. These devices will rely on low-field switching of the magnetization of adjacent decoupled ferromagnetic regions which are separated by some sort of barrier, across which electrons may pass without completely losing their spin polarization. Examples are planar tunnel junctions with an insulating barrier [2], polycrystalline material with grain boundaries [3] and pressed powder with interparticulate contacts [4].

Double perovskites $A_2BB'O_6$ with two ordered B-site cations have been studied since the 1960's and are known to be magnetic for B = Cr, Fe and B' = Mo, W, Re [5] [6] [7] [8] [9] where A is an alkaline earth cation. Recent interest in the family derives from reports by Kobayashi et al. [10] [11] that Sr_2FeMoO_6 and Sr_2FeReO_6 are half-metallic ferrimagnets, with an electronic structure where only minority spins are present at the Fermi level. The calculated electronic structure shows that the minority spin electron has $4d(Mo)t_{2g}^{\downarrow}$ character, that is, the molybdenum spins are antiparallel to the Fe spins. A neutron diffraction study of Sr_2FeMoO_6 by Garcia-Landa et al. [12] indicated that there is an iron moment of 4.1 μ_B but no localized moment was found on Mo. A study of Ca_2FeMoO_6 by Pinsard-Gaudart et al.

[13] using neutron diffraction and Mössbauer Spectroscopy has shown that there is a formal Fe^{3+}/Mo^{5+} charge configuration, and an iron moment of 4.0(1) μ_B with -0.2(3) μ_B on the Mo. These results might appear consistent with a $Fe^{2+}(3d^6)/Mo^{6+}(4d^0)$ valency, but this is excluded since it would give rise to insulating behaviour due to the localised nature of the Fe 3d orbitals. Because the $4d^{\downarrow}$ molybdenum electrons are delocalised, they contribute to the measured moment of $4\mu_B$ at the Fe site and originate the ferromagnetic Fe^{3+}-Fe^{3+} coupling by hybridising with the empty $3d(Fe)t_{2g}^{\downarrow}$ orbitals. Fluctuating valence states of $Fe^{2.8+}$ ($3d^{5.2}$) in Ca and Sr compounds [15] and $Fe^{2.5+}$ ($3d^{5.5}$) in Ba [15] and Sr [16] compounds have been observed from Mössbauer measurements. These fluctuating valencies are also aassociated with a reduction of the Fe site magnetic moment. The results are interpreted as the effect of the antiferromagnetically coupled itinerant electron that reduces both the spin and the valence state of the Fe ions. The exchange is analogous, but not identical to the double exchange in manganites. In manganites the hopping electron mediating the double exchange interaction is a Mn $3d^{\uparrow}$ electron. In the double perovskites it is a $\downarrow$ electron, mostly associated with Mo.

Much of the interest in double perovskites arises from the prospects of finding half-metallic oxides with high Curie temperatures. The paper by Kobayashi et al. [10] was followed by a series of reports from other groups confirming the high values of T_C and magnetoresistance of other materials of this series such as Sr_2FeMoO_6 [14] [12], Ca_2FeMoO_6 [14] and Ba_2FeMoO_6 [17] [14]. But more importantly, this surge of interest has hinted that the double perovskite system may be quite a complex one. The most striking feature from references [17] [12] [14] is that the expected magnetic moment of 4 μ_B/f.u. is never achieved for any of the compositions studied. Values ranging from 3.1 μ_B/f.u. [12] to 3.5 μ_B/f.u. [14] for SFMO ceramics in a

magnetic field of 5 T at 5 K have been reported. A stoichiometric half-metal has an integral number of electrons per formula unit and an integral number in the ↑ (or ↓) band because there is a gap with no ↓ (or↑) electrons at the Fermi energy. There is therefore an integral number of ↓ (or ↑) electrons, and the difference between the number of ↑ and ↓ electrons is also an integer. Hence the spin moment is also an integral number of Bohr magnetons. The values reported for the MR of SFMO are also inconsistent, ranging from MR<8% [12] to 15 % [14] at 77 K in a field of 1 T. These inconsistencies have raised a number of issues related to sample quality such as influence of microstructure or B-site cation ordering.

The influence of microstructure in transport properties has been studied using the same methods already applied to the manganese perovskites, such as a variation of the final annealing temperature in order to obtain different grain sizes. Such a procedure was followed by Maignan et al. in their study of Ba_2FeMoO_6 [17]. The starting sample was made from a stoichiometric mixture of oxides of the components annealed at 1100°C in vacuum for 10 hours. This sample shows the typical low temperature magnetoresistance of the type attributed to grain boundaries in the manganese perovskites. Furthermore, it also shows a large magnetoresistance near T_C =340 K (similar to the manganese system) which the authors attribute to a double exchange like mechanism. In order to separate the intergranular and intragranular components of the magnetoresistance, the sample was annealed in Ar/H_2 at 1000°C. The authors report a very small variation on the intragranular MR measured at 340 K. However, an increase from 20 % to 37 % at 10 K and 7 T was observed for the intergranular component demonstrating clearly the importance of intergrain transport in these compounds. Yuan et al. [18] prepared SFMO ceramics with three grain sizes: 29, 35 and 45 nm and found that both resistivity and MR increase with decreasing grain size in a similar way to that

reported by Balcells et al on $(La_{0.7}Sr_{0.3})MnO_3$ ceramic samples [19]. In spite of the similarities with the manganese perovskites, it is not clear yet what is the magnetic nature of the grain boundaries. The properties of a Sr_2FeMoO_6 single crystal were reported by Tomioka et al. [20]. T_C of the single crystal is 420 K and M_S=3.2 μ_B/f.u. due to anti-site disorder of 8% in the NaCl superstructure. Due to the absence of grain boundaries no magnetoresistance is observed at room temperature. Kim et al. [21], in a study of polycrystalline SFMO found that the low field MR ($\mu_0 H < 0.2T$) decreases with increasing temperature but at a slower rate that other half metals such as $(La_{0.7}Sr_{0.3})MnO_3$ and CrO_2. The authors suggest that, unlike in the manganese perovskites, the magnetic coupling between the Fe^{3+} and Mo^{5+} is the same in the bulk and at the grain boundaries although the latter are insulating. The suggestion is based on the similar behaviour of pyroclore $Tl_2Mn_2O_7$ where the grain boundary is expected to be ferromagnetic and insulating. However, this idea still lacks experimental confirmation. Some recent publications have focused on the problem of the influence of B-site cation ordering on magnetic and transport properties of the double perovskites. A study of a CFMO ceramic by Pinsard-Gaudart et al. [13] ascribes a double structure of the Mössbauer spectrum to Fe/Mo disorder (anti-site disorder). A value of p=7% for the concentration of anti-site defects is in good agreement with the Mössbauer measurements and a saturation magnetisation of 3.63 μ_B/f.u. for CFMO. Sarma et al. [22] have reported a study of magnetoresistance on ordered and disordered SFMO ceramics. The ordered ceramic was prepared by solid state reaction and the disordered ceramic by arc melting with the samples having similar grain size and morphology. The ordered sample shows large low field MR and a nearly saturated maximum MR value of 37% at 4.2 K and 7 T. The MR of the disordered sample shows a linear dependence in the whole field range reaching a maximum of 10% at 4.2K and 7 T.

The authors ascribe the low field MR of the ordered sample to intergrain spin-dependent tunneling. Because the disordered sample is not a half metal the spin-dependent scattering is greatly reduced and the MR arises mostly from the suppression of spin fluctuations. The effect of anti-site defects in SFMO was studied by Ogale et al. [23] by a Monte Carlo simulation. The magnetisation and T_C are found to decrease at a rate of -0.065 μ_B/x and -3K/x respectively, where x is the anti-site defect concentration. This finding is in good agreement with values of $T_C = 415$K and $M_S = 3\ \mu_B$/f.u. (at 4.2 K) reported by Kobayashi et al. [10] in a 13% disordered SFMO ceramic. The authors also consider the effect of oxygen vacancies, showing that the saturation magnetisation and T_C decrease with increasing concentration of vacancies. Since oxygen is the bridge for the superexchange interactions in this system, such oxygen vacancies would essentially switch off these interactions across a fraction of the bonds and reduce the saturation magnetisation.

A related model groups the misplaced cations together on antiphase boundaries such as exist in thin films of Fe_3O_4[25], which show less than the bulk saturation magnetization, and were recently proposed to explain the low magnetization of Sr_2FeMoO_6 ceramics[15] [26] [27] and thin films. In polycrystalline materials, nucleation takes place at many points. Normally, the crystallites meet at a grain boundary, but prolonged annealing can lead to grain growth where the antiphase boundaries persist in large crystallites as vestiges of the original grain boundaries. Antiphase boundaries will have consequences for the magnetization of the A_2FeMoO_6 series, because the boundaries are planes of Fe - O - Fe superexchange bonds, instead of the normal Fe - O - Mo bonds in the ideal ordered structure. An applied field of order of the exchange field is required to overcome the antiferromagnetic coupling at the antiphase boundary. In an applied field, the regions on either side of the antiphase boundaries

are aligned, but there is a quasi-domain wall at the boundary which narrows with increasing field. The antiferromagnetically coupled spins at the boundary therefore align perpendicular to the applied field and do not contribute to the magnetization. Furthermore, since they resemble domain walls which are only one atom wide, the antiphase domain boundaries should contribute greatly to the resistance of a half metal in the unmagnetized state. It is possible to reconcile the large resistance of the A_2FeMoO_6 compounds with their supposed half-metallicity in this way.

Ritter et al. [28] studied the correlation between crystal structure and magnetic properties of a series of ceramics AA'$FeMoO_6$ with AA'=Ca_2, Sr_2, Ba_2 and BaSr. As the average ionic radius decreases, the crystallographic structure evolves from cubic (AA'=Ba_2, BaSr) to tetragonal (Sr_2) and finally to monoclinic (Ca_2). A maximum value of T_C is obtained for the tetragonal structure. The authors find a very good correlation between the value of T_C and the bandwidth W which depends on the crystal structure.

Fabrication of thin films is a paramount requirement in order to realise the double perovskites potential in device applications. Manako et al. [29] deposited Sr_2FeMoO_6 thin films by PLD on $SrTiO_3$ substrates with orientations (001) and (111). The authors used an estimate based on thermodynamics to find the optimum deposition conditions leading to Fe^{3+}/Mo^{5+} valences. These are a substrate temperature between 900 and 950°C and an oxygen pressure of 10^{-5} Torr. The resistivity of their films showed metallic behaviour below room temperature with values of the order of 1 mΩcm. Magnetoresistance values of 5 % at room temperature and 7 Tesla were observed but the saturation magnetisation at 5 K did not exceed 2 μ_B/f.u. suggesting a high degree of B site disorder. Asano et al. [30] used PLD to deposit SFMO films on $SrTiO_3$ (001) substrates at temperatures of 800 and 850°C. The authors found

saturation magnetisations of only 1.5 μ_B/f.u. and observed the existence of $SrFeO_3/SrMoO_3$ phase separation (for the film deposited at 850°C) leading to positive magnetoresistance. Westerburg et al. [31] reported a systematic study of the film properties dependence on deposition conditions for SFMO. Films were deposited on $SrTiO_3$ (001) substrates at different temperatures and background pressures. Even for O_2 pressures as low as 10^{-1} Torr the films form in a yellow insulating phase for all substrate temperatures. The double perovskite structure can be obtained at substrate temperatures as low as 320°C but full B-site cation ordering just takes place for substrate temperatures above 930°C when the magnetisation was found to reach its full value of 4 μ_B/f.u.

4.2 Study of A_2FeMoO_6 for A = Ca, Sr, Ba

4.2.1 Ceramics

Here we present a study on the magnetic properties and magnetoresistance of A_2FeMoO_6 ceramics with A=Ca, Sr, Ba. All samples were prepared under the same conditions from a stoichiometric mixture of ACO_3 (A=Ca, Sr, Ba), $FeCO_3$ and $MoCO_3$ calcined at 980 °C and then reground and refired, with a final firing for 5 - 10 hours at 1100°C in an atmosphere of 1% H in Ar. All compounds are single-phase and exhibit a series of superstructure reflections due to cation order of Fe and Mo on alternate B-sites of the perovskite structure. A detailed study of the crystal structure of these samples can be found in the PhD Thesis of R.-M. Thomas [32]. Lattice parameters and x-ray densities are listed in Table 4 in the Discussion section. All the ceramics have a density of about 90 % of the X-ray density. Curie temperatures were determined by AC susceptibility measurements on ceramic bars [32]. They are T_C^{CFMO}= 345 K, T_C^{SFMO}= 425 K and T_C^{BFMO}= 367 K.

The microstructure of the samples was studied by scanning electron microscopy and is shown in Figure 4.1.

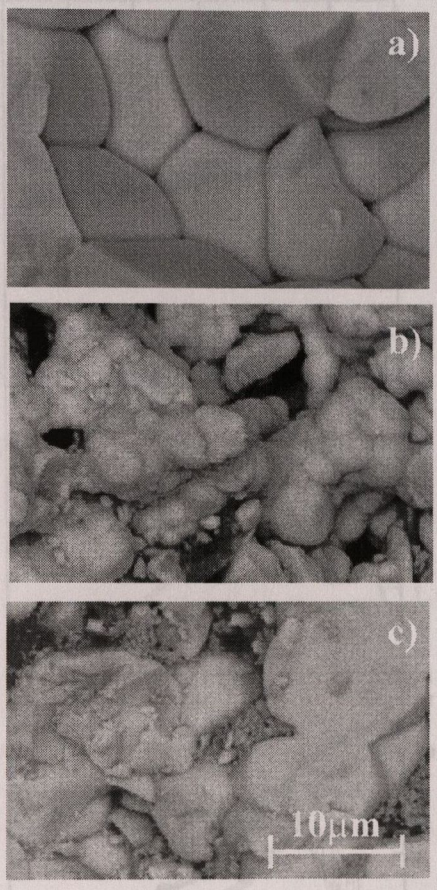


Figure 4.1. The grain structure of the double perovskite ceramic samples studied. a) Ca_2FeMoO_6, b) Sr_2FeMoO_6 and c) Ba_2FeMoO_6.

The Ca sample is very compact showing well defined grains with sizes 5-10 μm. The Sr sample has grains with sizes 3-5 μm and is more porous than the Ca sample. The Ba sample shows a mixed grain structure with well defined 10 μm grains together with smaller ($<1\mu$m) powder like grains.

The temperature dependence of resistivity was measured while cooling in zero field (ZFC) and heating in field (FH) of 0.3 T. The resistivity of the ceramic samples is quite variable, but all have the positive temperature coefficient of resistivity characteristic of a metal. The

to the values for the more conducting ferromagnetic manganites. No magnetoresistance was observed over the whole temperature range for this sample.

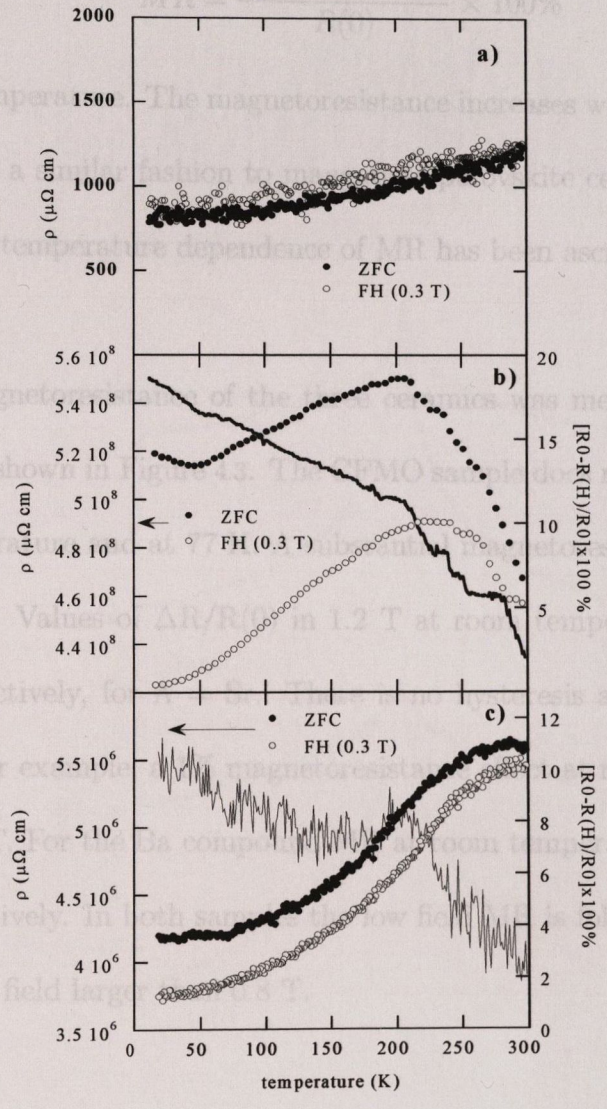


Figure 4.2. The resistivity in zero field and 0.3 Tesla and magnetoresistance (solid line) for a) Ca_2FeMoO_6, b) Sr_2FeMoO_6 and c) Ba_2FeMoO_6.

The resistivity of the Sr and Ba samples is shown in Figure 4.2b) and c) respectively. The magnetoresistance shown in the figure was calculated from the expression

$$MR = \frac{R(0) - R(0.3T)}{R(0)} \times 100\% \tag{21}$$

magnetoresistance shown in the figure was calculated from the expression

$$MR = \frac{R(0) - R(0.3T)}{R(0)} \times 100\% \tag{21}$$

for each value of temperature. The magnetoresistance increases with decreasing temperature for both samples in a similar fashion to manganese perovskite ceramics. In the manganese system this kind of temperature dependence of MR has been ascribed to transport through grain boundaries.

The isothermal magnetoresistance of the three ceramics was measured at 77 K and room temperature and is shown in Figure 4.3. The CFMO sample does not exhibit any measurable MR at room temperature and at 77 K. A substantial magnetoresistance is observed on the Sr and Ba samples. Values of $\Delta R/R(0)$ in 1.2 T at room temperature and at 77 K are 7 % and 15 %, respectively, for A = Sr. There is no hysteresis and a substantial low-field response is seen. For example, a 1% magnetoresistance effect at room temperature requires a field of just 20 mT. For the Ba compound MR at room temperature and 77 K in 1.2 T is 6% and 14% respectively. In both samples the low field MR is followed by a linear decrease of the resistivity for field larger than 0.8 T.

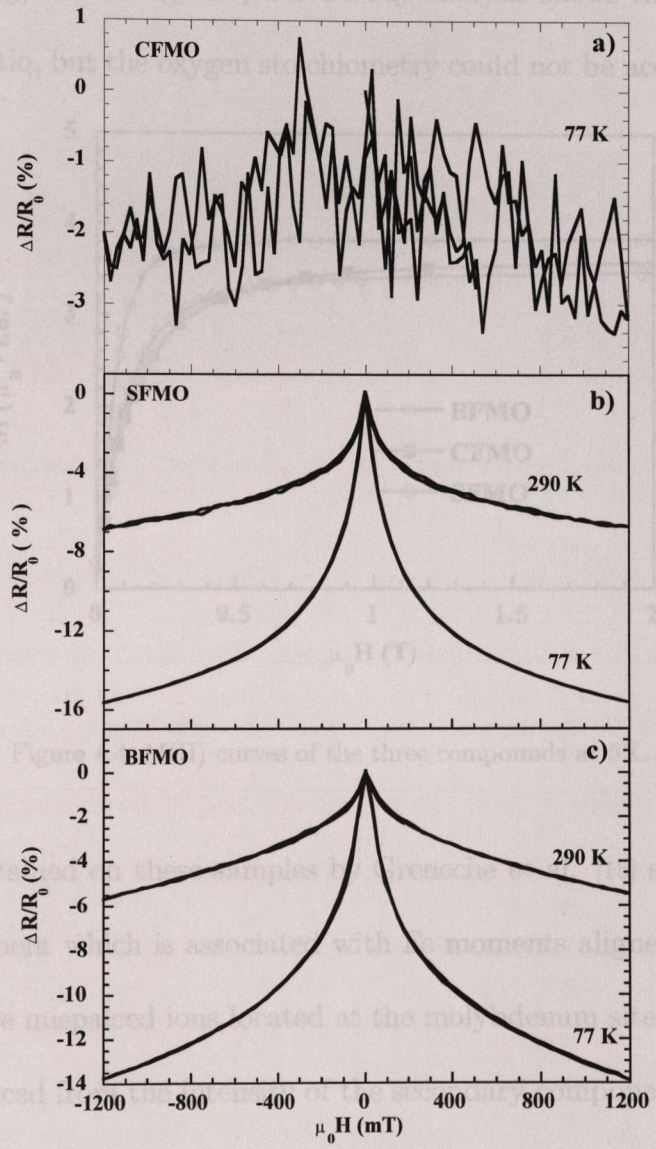


Figure 4.3. Isothermic magnetoresistance at room temperature and 77 K of a) Ca_2FeMoO_6, b) Sr_2FeMoO_6 and c) Ba_2FeMoO_6.

The isothermal magnetisation of the three compounds was measured at 5 K and is shown in Figure 4.4. The measurements were performed using a SQUID magnetometer at Laboratoire de Physicochimie des Solides du CNRS, Université Paris-Sud. The saturation magnetisation of all samples is lower than the (5-1) = 4 μ_B/f.u. expected from the ionic ferrimagnetic configuration Fe^{3+}/Mo^{5+}. Only the Ba sample approaches this value with a saturation

magnetisation of 3.9 μ_B/f.u. Energy-dispersive x-ray analysis shows that our samples have the expected cation ratio, but the oxygen stoichiometry could not be accurately determined.

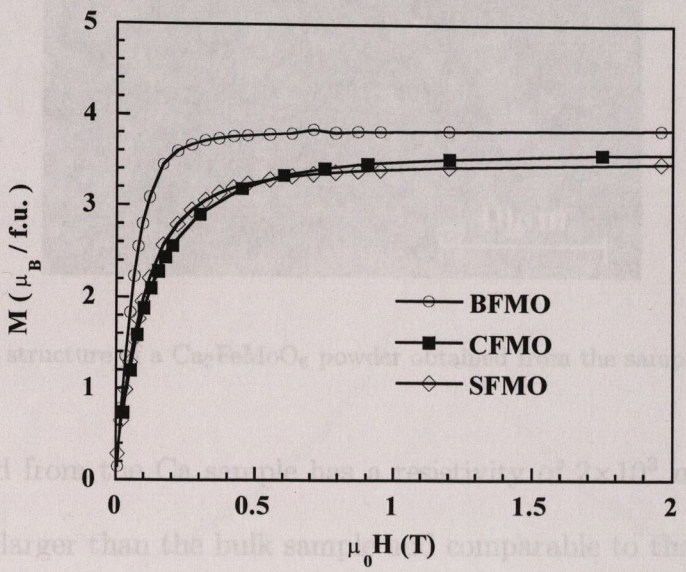


Figure 4.4. M(H) curves of the three compounds at 5K.

Mössbauer spectra obtained on these samples by Greneche et al. [15] show the appearence of a secondary component which is associated with Fe moments aligned antiparallel to the applied field. These are mispalced ions located at the molybdenum sites. The percentage of displaced Fe ions deduced from the intensity of the secondary component is 7, 6 and 2% for the Ca, Sr and Ba compounds respectively.

The Ca and Sr samples were used to measure powder magnetoresistance. The ceramics were ground with a pestle and mortar and the powders were pressed into 5 mm diameter pellets. No heat treatment was performed on the samples. The microstructure of the CFMO powder shown in Figure 4.5 is representative of ceramic powder samples. The change in microstructure is clear as compared to Figure 4.1a), with irregularly shaped grains and a wider size distribution. The density of the pellets is 80 % and 74% of the x-ray density for the Ca and Sr ceramics respectively.

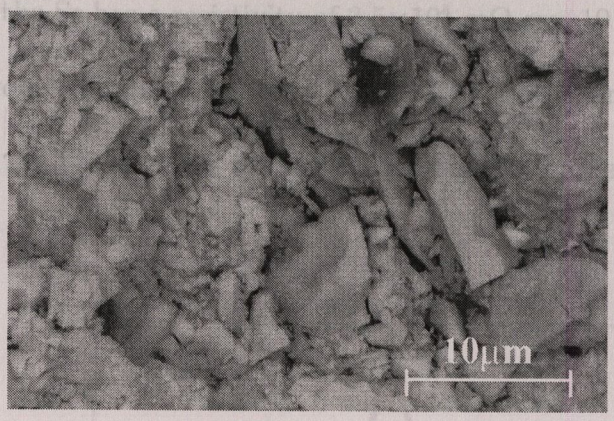


Figure 4.5. The grain structure of a Ca_2FeMoO_6 powder obtained from the sample shown in Figure 4.1.

The powder obtained from the Ca sample has a resistivity of 2×10^3 mΩ cm, almost four orders of magnitude larger than the bulk sample and comparable to that of the BFMO ceramic. The magnetoresistance of the CFMO pressed powder at 77 K is shown in Figure 4.6. The MR is largely improved in the powder sample with a value of 4% in 1.2 T. The MR loop shows the typical butterfly shape, with two symmetrical resistivity maxima corresponding to the coercivity of the material, observed in other pressed powder samples [4]. No magnetoresistance was observed at room temperature.

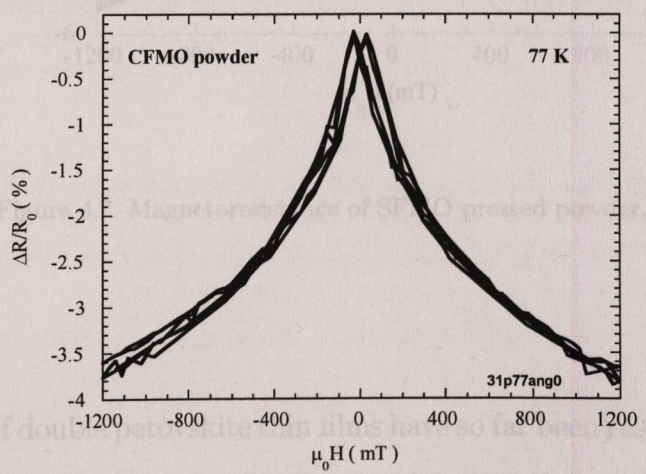


Figure 4.6. Magnetoresistance at 77 K of Ca_2FeMoO_6 cold pressed powder.

The pressed powder of the Sr has a resistivity of 3.5×10^4 mΩ cm, 10 times smaller that the bulk sample. The powder compound shows 1.3 % MR at 290 K and 5.5 % at 77 K in a field of 1.2 T (Figure 4.7). These values are lower than those obtained for the bulk ceramic sample.

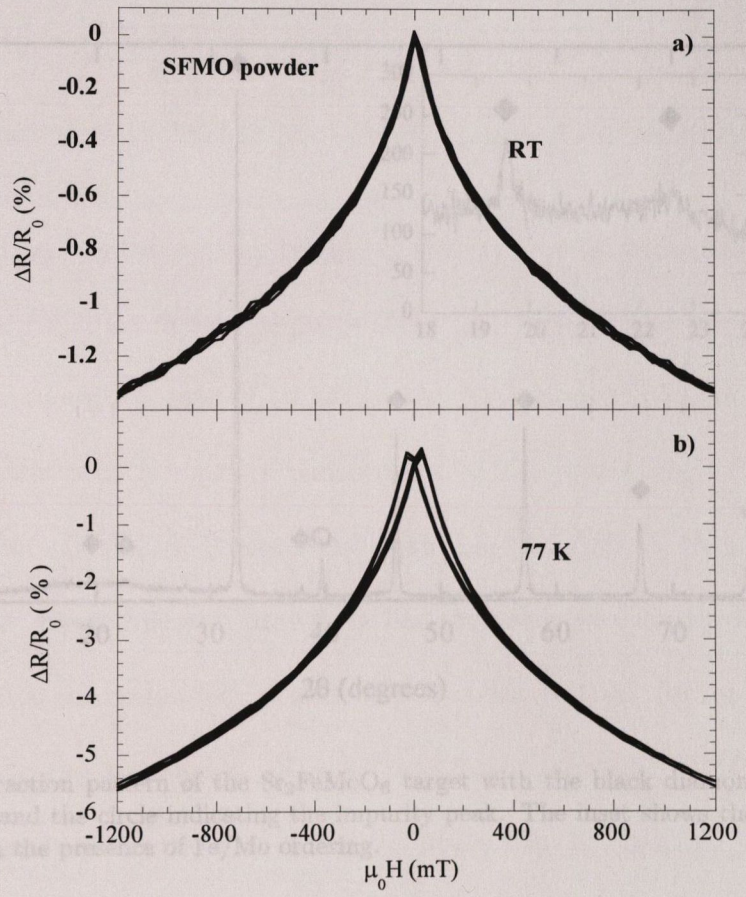


Figure 4.7. Magnetoresistance of SFMO pressed powder.

4.2.2 Thin films

Reports on deposition of double perovskite thin films have so far been restricted to Sr_2FeMoO_6 films on $SrTiO_3$ substrates deposited by PLD [29] [30] [31] or magnetron sputtering [33]. Here we present a study of structural, transport and magnetic properties of Sr_2FeMoO_6 thin films

deposited on $SrTiO_3$ (100) and MgO (100) substrates. Thin films were deposited from a Sr_2FeMoO_6 target prepared by solid state reaction. Figure 4.8 shows the x-ray diffraction pattern of the target showing the SFMO single phase and small amount of an unidentified impurity phase.

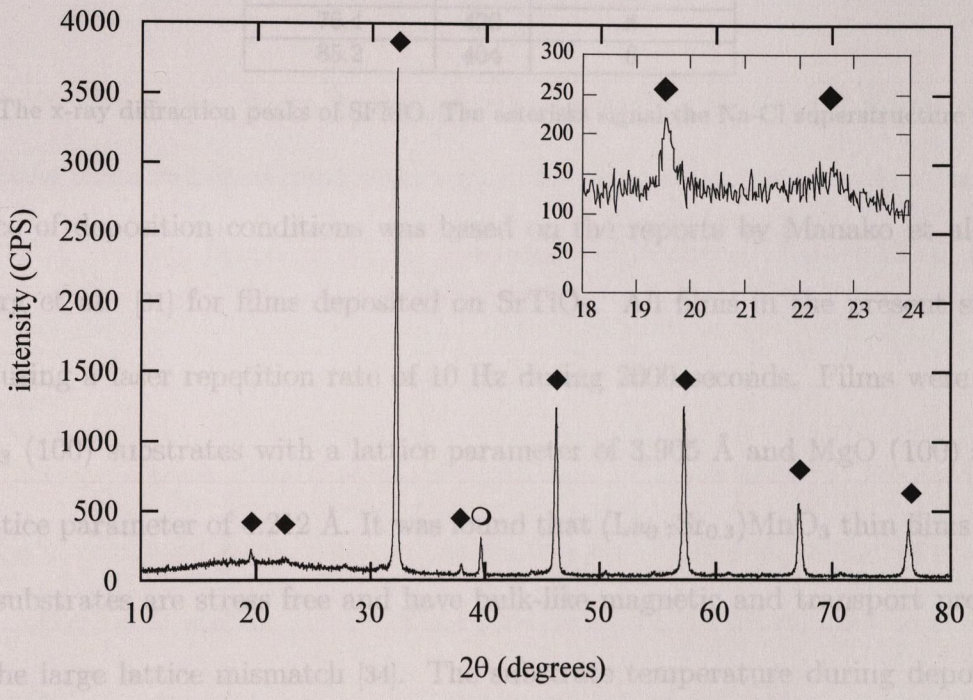


Figure 4.8. X-ray diffraction pattern of the Sr_2FeMoO_6 target with the black diamonds indicating the double perovskite phase and the circle indicating the impurity peak. The inset shows the (101) and (002) reflections, only visible in the presence of Fe/Mo ordering.

The (101), (002) and (103) reflections only appear when the Fe and Mo are ordered in the rock salt Na-Cl type structure. The inset to Figure 4.8 shows the (101) and (002) reflections. The extent of Fe/Mo ordering can be deduced from the relative intensity of these reflections. However, for the purpose of laser ablation it is sufficient to have a stoichiometric target given that the cation ordering in the film is determined by the deposition conditions [31]. Table 2 gives the position of the (hkl) reflections of SFMO indicating the superstructure reflections

corresponding to Fe/Mo ordering in alternate B-sites.

2θ (degrees)	(hkl)	Intensity (%)
19.1*	101	15
22.1*	002	7
32.1	112	100
37.6*	103	10
46.2	220	24
57.2	204	34
67.1	224	21
76.4	420	8
85.2	404	6

Table2.The x-ray diffraction peaks of SFMO. The asterisks signal the Na-Cl superstructure reflections.

The choice of deposition conditions was based on the reports by Manako et al. [29] and Westerburg et al. [31] for films deposited on $SrTiO_3$. All films in the present study were obtained using a laser repetition rate of 10 Hz during 2000 seconds. Films were deposited on $SrTiO_3$ (100) substrates with a lattice parameter of 3.905 Å and MgO (100) substrates with a lattice parameter of 4.212 Å. It was found that $(La_{0.7}Sr_{0.3})MnO_3$ thin films deposited on MgO substrates are stress free and have bulk-like magnetic and transport properties in spite of the large lattice mismatch [34]. The substrate temperature during deposition was measured using an infrared pyrometer. A substrate temperature of 950^{o}C represents an upper limit for the temperature produced by the SN heaters in the chamber. The deposition pressure was the lowest possible in the present system, 10^{-6} mbar and all other variables are as described in Chapter 3 for $(La_{0.7}Sr_{0.3})MnO_3$, including a laser fluence on the target of 2 Jcm^{-2}. A series of seven films was deposited using the conditions summarised in Table 3.

sample name	substrate temperature (°C)	pressure (mbar)	in situ annealing
stoA	950	10^{-6}	none
stoB	900	10^{-6}	none
stoC	770	10^{-6}	none
mgoA	950	10^{-6}	none
mgoB	720	10^{-6}	none
mgoC	950	10^{-6}	600°C, 0.4 bar O_2, 30 min
mgoD	950	10^{-6}	900°C, vacuum, 30 min

Table3.Deposition conditions of SFMO films deposited on MgO substrates.

The prefix to the capital letter in the sample name refers to the substrate used. Film thickness was measured by etching a corner of one film of each series by ion beam milling and measuring the step height by AFM. The measured thickness of the films is 100 nm. A separate description of the properties of thin films deposited on the two different substrates is given below.

X-ray diffraction patterns of the three films deposited on STO substrates are shown in Figure 4.9. All the non-indexed x-ray peaks in this section are originated on the substrate. Only the (220) reflection is visible, i.e. the films grow with the c axes parallel to the substrate plane. The lattice parameter a is larger than the bulk value of 5.573 Å for all films reaching a maximum of 5.671 Å, 1.8 % larger than the bulk value, for sample stoC. Table 4 in the Discussion section summarises all the data obtained on these films.

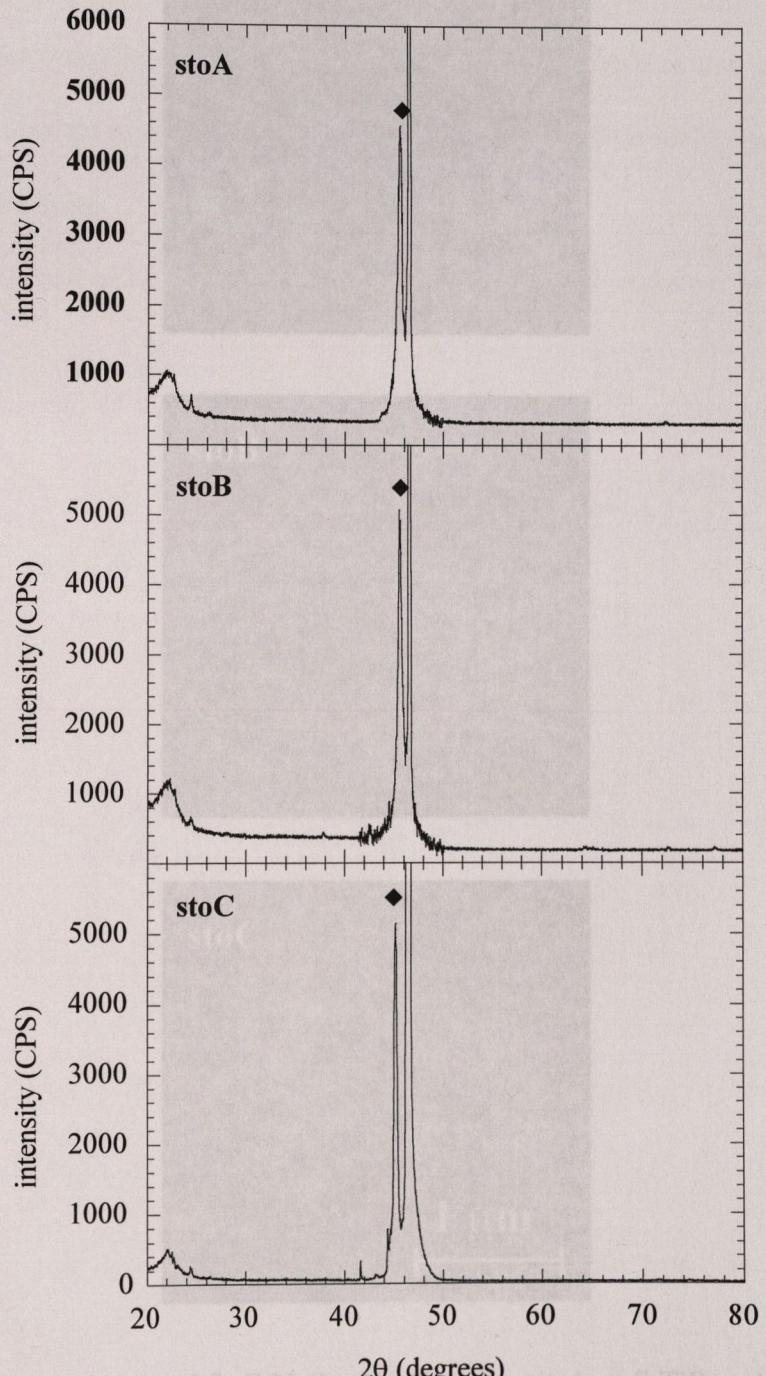


Figure 4.9. X-ray diffraction patterns for SFMO films deposited on STO (100) substrates. There is only one visible reflection - (220) - marked by the black diamond.

The surface morphology was studied by AFM and is shown in Figure 4.10.



Figure 4.10. Surface morphology of Sr_2FeMoO_6 thin films deposited on $SrTiO_3$ substrates at different temperatures.

Sample stoA deposited at 950^{o}C has a granular structure with grain size in the range 100-200 nm. Films deposited at 900^{o}C show the existence of L-shaped holes with a depth of

approximately 12 nm. The same surface morphology was observed in another film deposited at 850°C. A striking feature of these holes is that they are all oriented along the same two perpendicular directions. Sample stoC, deposited at 770°C shows a smooth surface. The surface roughness over an area of 3×3μm is 12 nm for sample stoB and approximately 1 nm for the other two samples.

Resistivity as a function of temperature between 12 and 300 K is shown in Figure 4.11.

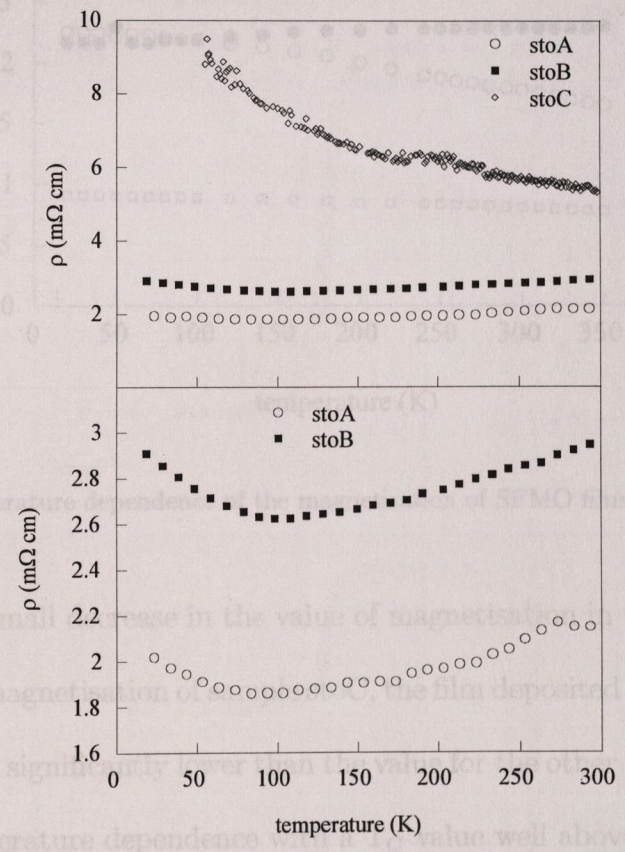


Figure 4.11. Temperature dependence of resistivity in zero field for the three films deposited on STO substrates.

The film deposited at the highest substrate temperature (950°C) shows the lowest resistivity with a value of approximately 2 mΩ cm. The resistivity of both samples stoA and stoB has a small dependence on temperature showing a minimum around 100 K. The film deposited at

the lowest temperature (770°C) shows a semiconducting behaviour with a room temperature resistivity of 6 mΩcm.Magnetisation measured as a function of temperature between 20 and 350 K in 0.3 T is shown in Figure 4.12.

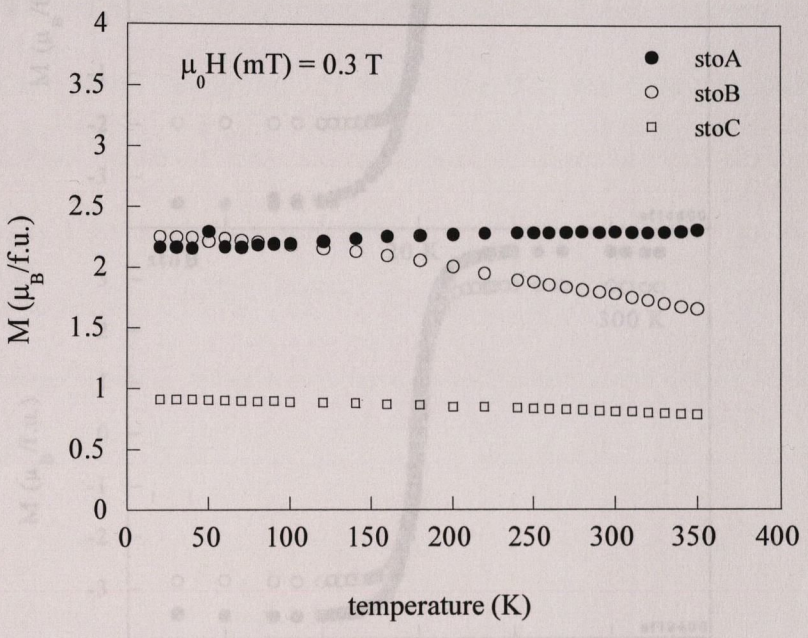


Figure 4.12. Temperature dependence of the magnetisation of SFMO films on STO substrates.

All films show a very small decrease in the value of magnetisation in the temperature range studied. The value of magnetisation of sample stoC, the film deposited at the lowest substrate temperature (770°C) is significantly lower than the value for the other two samples but shows the same type of temperature dependence with a T_C value well above 350 K. This suggests the formation of a more disordered phase for this film. Further information can be obtained from the isothermic magnetisation loops measured at 20 and 300 K and shown in Figure 4.13.

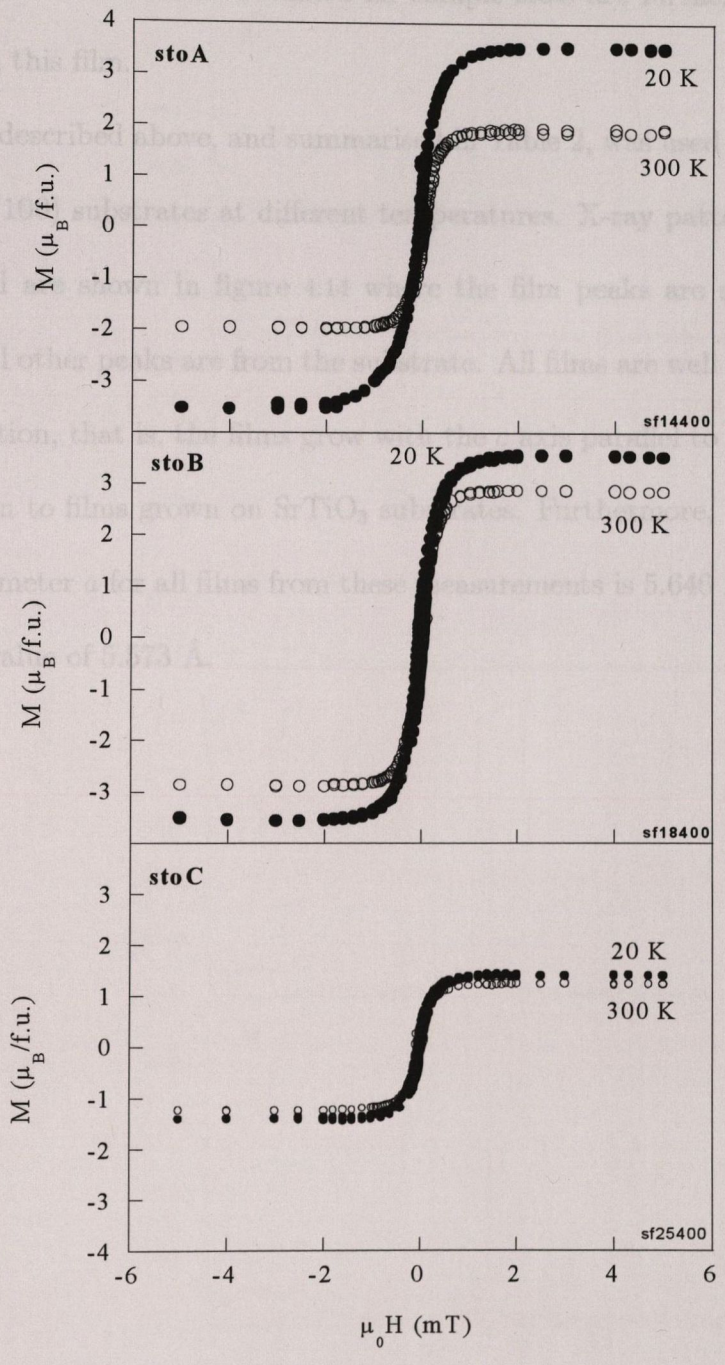


Figure 4.13. Isothermal magnetisation loops for the three films deposited on STO substrates.

Samples stoA and stoB have saturation magnetisation values of 3.5 μ_B/f.u. at 20 K, very close to the full value of 4 μ_B/f.u. obtained at 5 K by other authors [31] [33]. The poor

saturation magnetisation values obtained for sample stoC are further indication of a lower Fe/Mo order in this film.

The procedure described above, and summarised in Table 2, was used to deposit four SFMO films on MgO (100) substrates at different temperatures. X-ray patterns were obtained for all samples and are shown in figure 4.14 where the film peaks are signalled with a black diamond and all other peaks are from the substrate. All films are well textured showing only the (220) reflection, that is, the films grow with the c axis parallel to the substrate plane in a similar fashion to films grown on $SrTiO_3$ substrates. Furthermore, the value obtained for the lattice parameter a for all films from these measurements is 5.646 Å which is 1.3% larger than the bulk value of 5.573 Å.

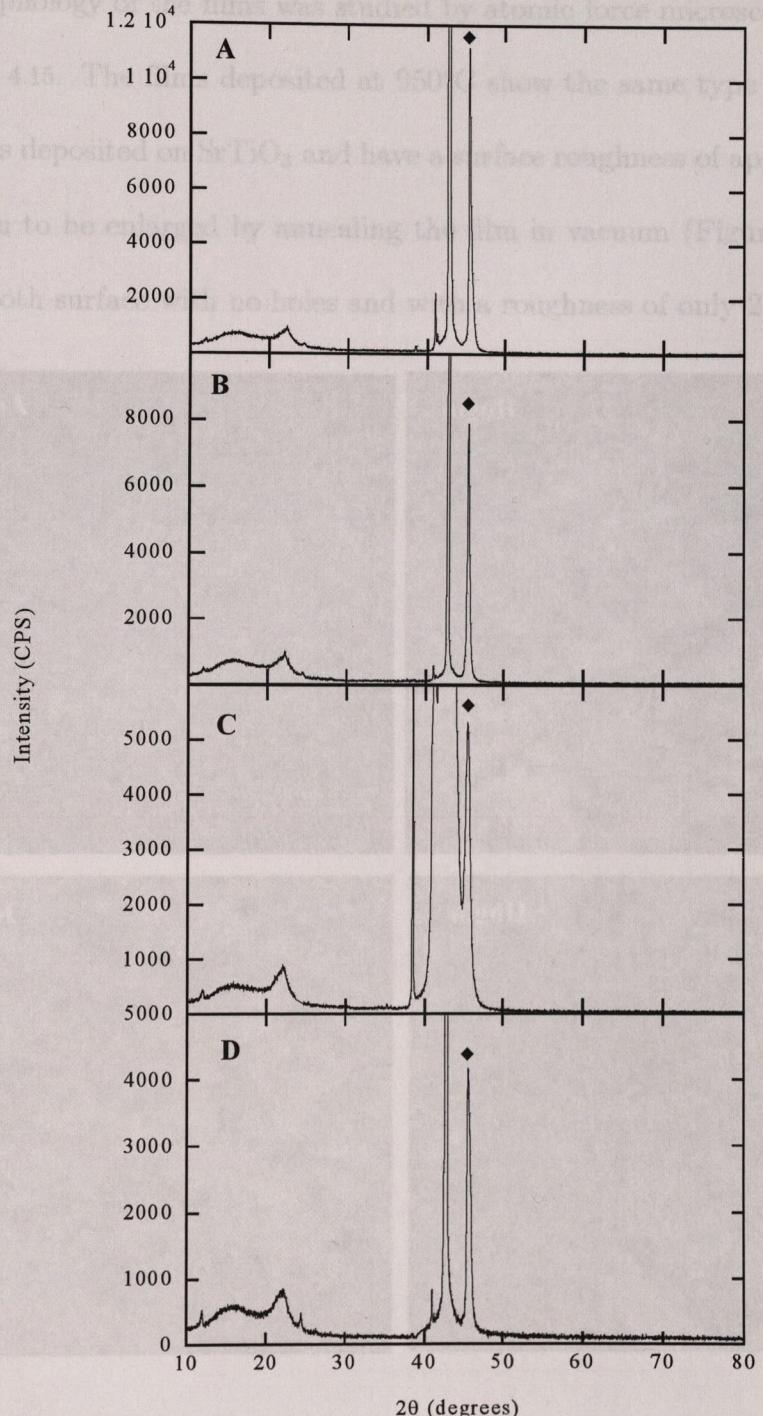


Figure 4.14. X-ray diffraction patterns of Sr_2FeMoO_6 films deposited on MgO. (220) is the only visible SFMO peak and is indicated by a black diamond.

The (220) reflection of film mgoC is broader than that of the other films.

The surface morphology of the films was studied by atomic force microscopy (AFM) and is shown in Figure 4.15. The films deposited at 950°C show the same type of L-shaped holes observed for films deposited on $SrTiO_3$ and have a surface roughness of approximately 5 nm. These holes seem to be enlarged by annealing the film in vacuum (Figure 4.15 D). Sample mgoB has a smooth surface with no holes and with a roughness of only 2 nm.

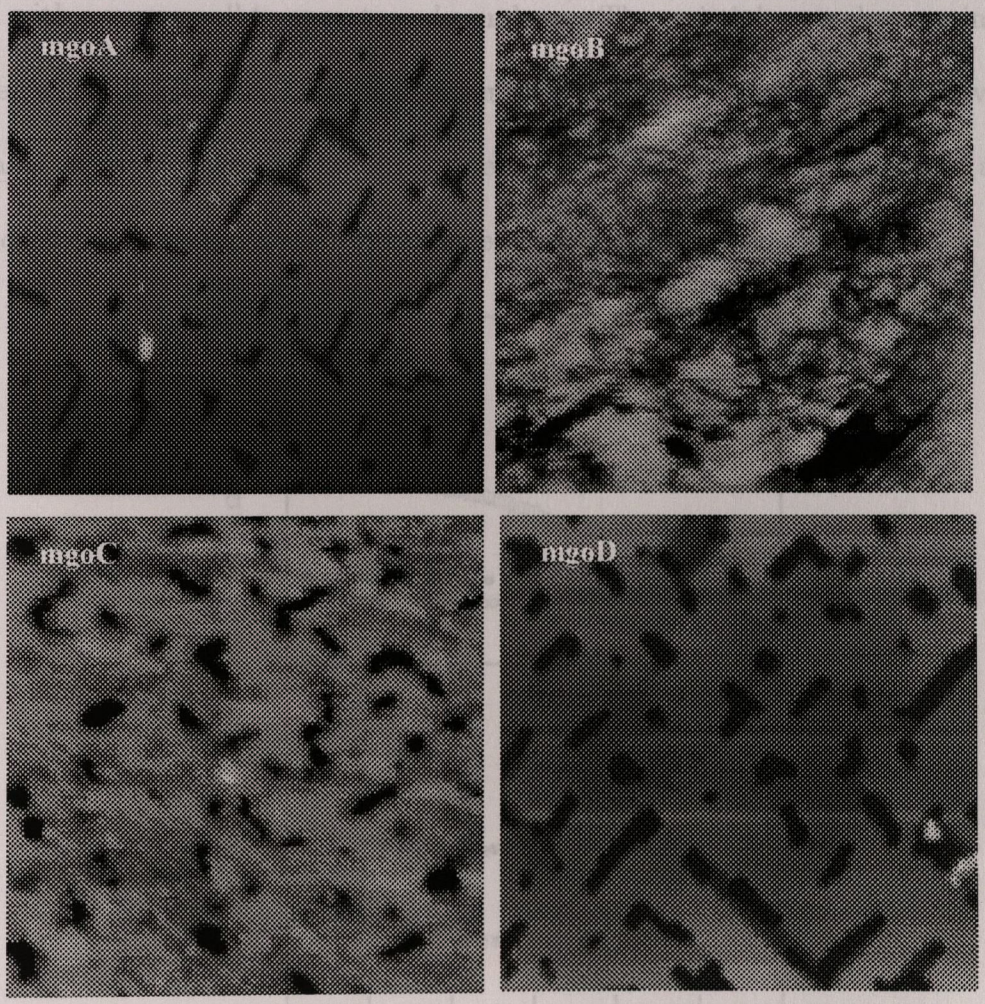


Figure 4.15. Surface topography of Sr_2FeMoO_6 films deposited on MgO substrates at different temperatures.

Resistivity as a function of temperature was measured for the four samples in zero field and the results are shown in Figure 4.16. The resistivity of the sample annealed in oxygen

(mgoC) is not shown since it is insulating. All the other samples show room temperature resistivity values in the range 1.5 - 3 mΩ cm in good agreement with the results of other authors [31] [33]. The film deposited at 720°C shows a semiconducting behaviour over the whole temperature range. The resistivity of the films deposited at 950°C is shown in Figure 4.16b). The film deposited at 950°C with no annealing has a metallic behaviour in the range 150-300 K with a very small temperature dependence. The resistivity reaches a minimum at 150 K after which it increases to values higher that the room temperature resistivity. The film annealed in vacuum shows the same type of behaviour but the minimum is at 110 K above which the sample has a more pronounced metallic resistivity.

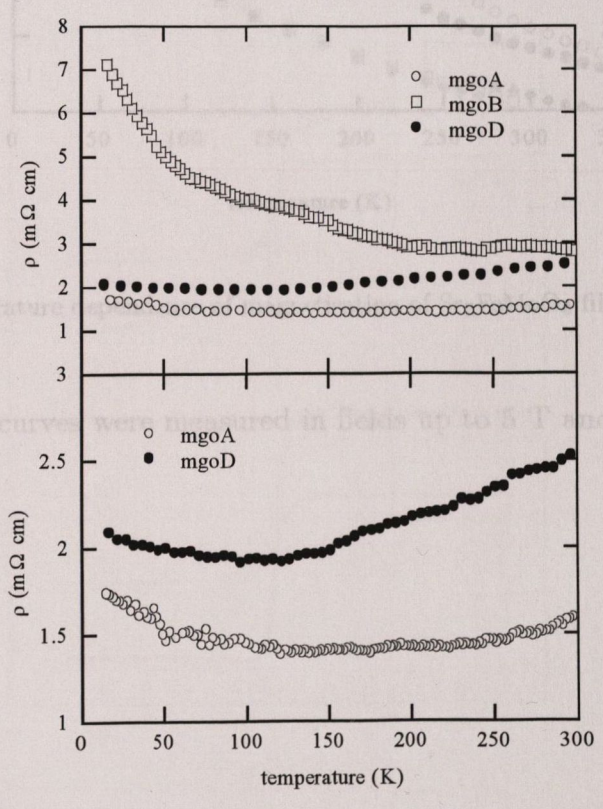


Figure 4.16. The zero field resistivity of films deposited on MgO substrates.

The magnetisation as a function of temperature is shown in Figure 4.17 for the four samples in

a field of 0.1 T. The magnetisation decays rather rapidly with temperature for all samples, with the sample deposited at 720°C (mgoB) having T_C below room temperature. The magnetisation of sample mgoC is similar to mgoB but still has a small magnetisation of $0.07\mu_B$/f.u. at room temperature. Samples mgoA and mgoD have T_C above 350 K.

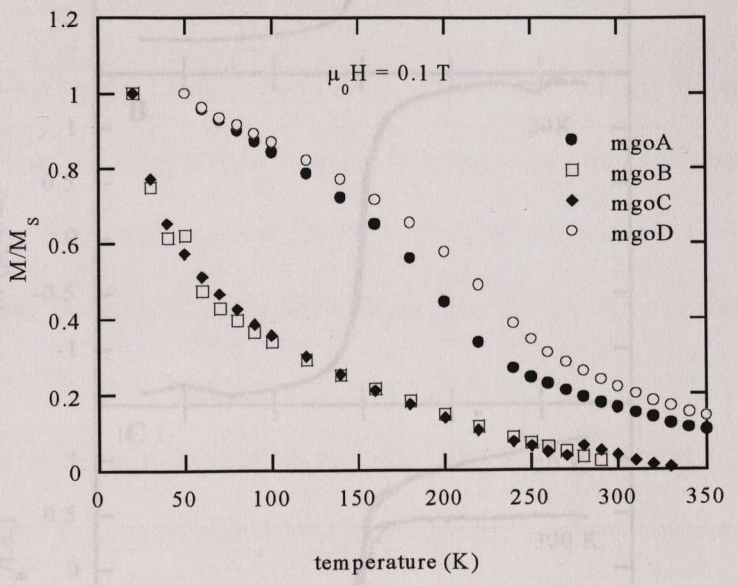


Figure 4.17. The temperature dependence of magnetisation of Sr_2FeMoO_6 films deposited on MgO.

Isotermic magnetisation curves were measured in fields up to 5 T and are shown in Figure 4.18.

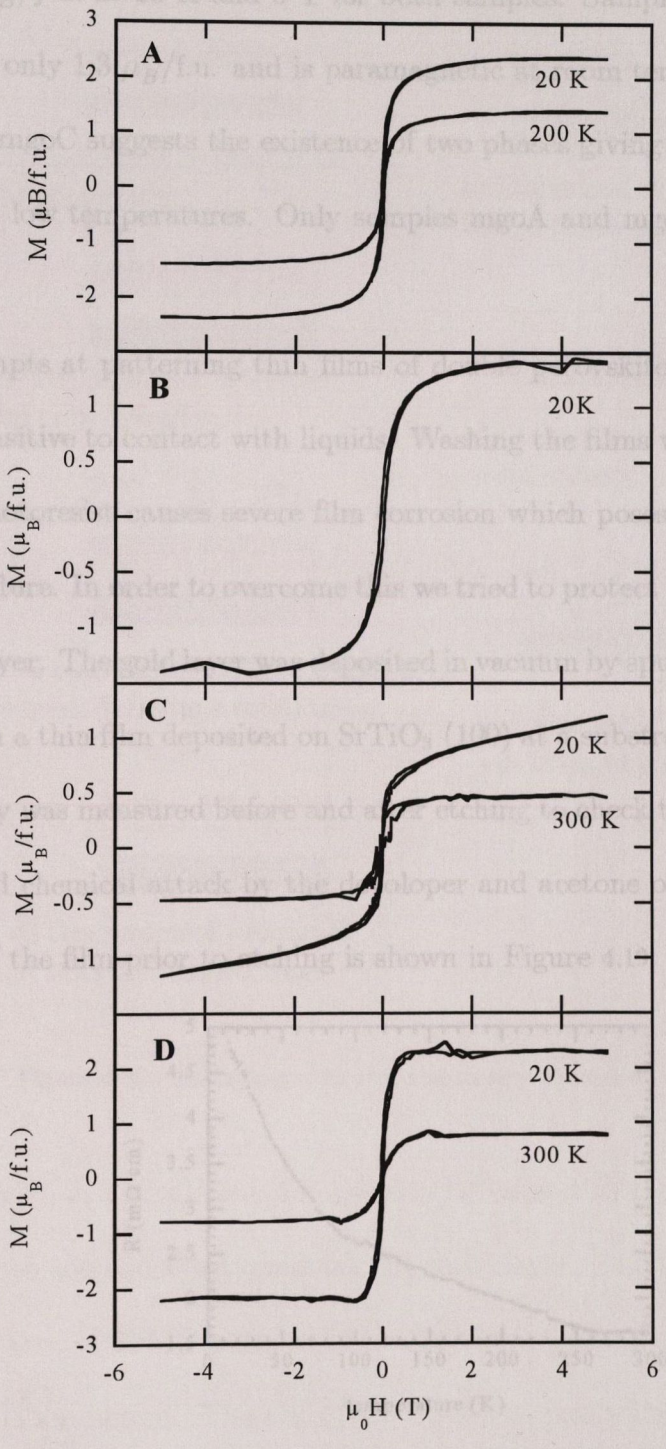


Figure 4.18. Magnetisation curves of the four SFMO films deposited on MgO.

Samples mgoA and mgoD are the best ferromagnets, although the saturation magnetisa-

tion is just 2.3 $\mu_B/f.u.$ at 20 K and 5 T for both samples. Sample mgoB has a saturation magnetisation of only 1.3 μ_B/f.u. and is paramagnetic at room temperature. The magnetisation of sample mgoC suggests the existence of two phases giving rise to a non-saturatable magnetisation at low temperatures. Only samples mgoA and mgoD have T_C above room temperature.

In the first attempts at patterning thin films of double perovskites it was found that they are extremely sensitive to contact with liquids. Washing the films with acetone or methanol to remove the photoresist causes severe film corrosion which poses a major obstacle to any patterning procedure. In order to overcome this we tried to protect the films by deposition of 30 nm gold cap layer. The gold layer was deposited in vacuum by sputtering. This experiment was performed on a thin film deposited on $SrTiO_3$ (100) at a substrate temperature of 850°C and the resistivity was measured before and after etching to check the combined effect of ion beam etching and chemical attack by the devoloper and acetone on the quality of the film. The resistivity of the film prior to etching is shown in Figure 4.19.

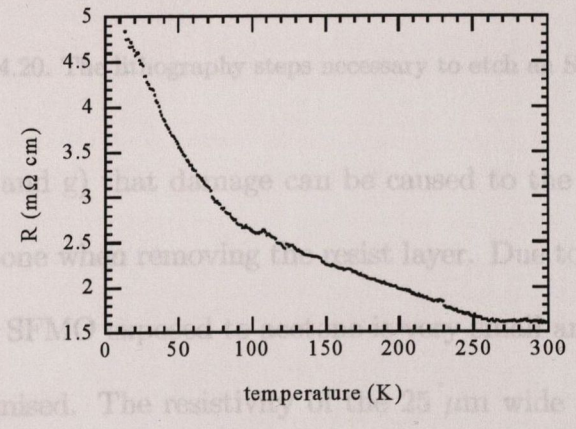
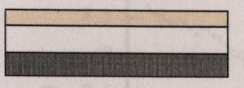
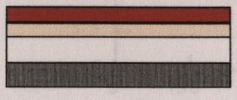


Figure 4.19. The pre-etching resistivity of an SFMO film deposited on $SrTiO_3$ at 850°C.

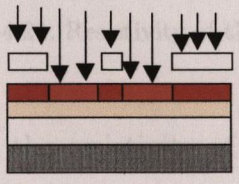
A track with a width of 25 nm was etched on this film following the procedure summarised in Figure 4.20.



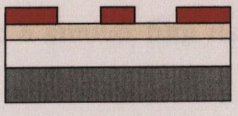
a) Deposition of gold layer by sputtering.



b) Deposition of UV resist layer by spinning.



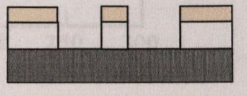
c) Exposure to UV light through a mask defining a small track.



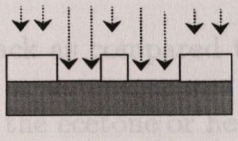
d) Development - removal of the polymerised areas.



e) Etching of exposed areas by ion beam milling.



f) Removal of the resist with acetone.



g) Removal of gold layer by ion beam milling.

Figure 4.20. The lithography steps necessary to etch an SFMO film.

It is during steps e), f) and g) that damage can be caused to the film by the ion beam or by the contact with acetone when removing the resist layer. Due to the presence of the gold layer the surface area of SFMO exposed to acetone is very small and the damage caused by chemical attack is minimised. The resistivity of the 25 μm wide etched track is shown in Figure 4.21.

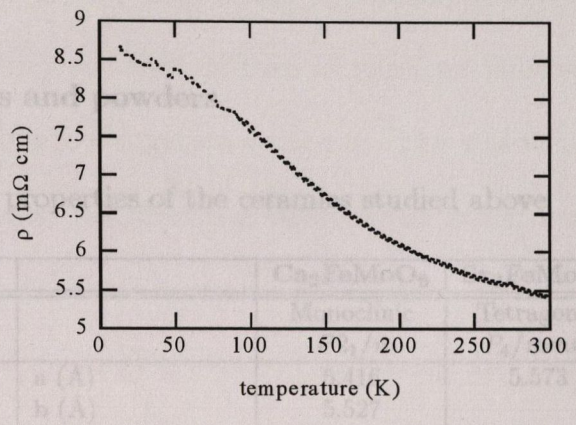


Figure 4.21. Resistivity of the SFMO film of Figure 4.19 after etching.

There is an increase in the resistivity of the etched track as compared to the film which is probably due to damage caused by quemical attack by the ecetone or heating caused by the ion beam. However, this damage is confined to a few microns at the sides of the track. A 3 μm wide track etched on a similar film using the procedure described above is insulating.

4.3 Discussion

4.3.1 Bulk ceramics and powders

Table 4 summarises the properties of the ceramics studied above.

		Ca_2FeMoO_6	Sr_2FeMoO_6	Ba_2FeMoO_6
Crystal structure		Monoclinic $P2_1/n$	Tetragonal P_4/mmm	Cubic $Fm3m$
Lattice parameters	a (Å) b (Å) c (Å) β (^{o})	5.416 5.527 7.698 90.04	5.573 7.905 	8.062
X-ray density	ρ_X (kgm^{-3})	4727	5714	6623
Curie temperature	T_C (K)	345	426	367
Saturation magnetisation	m_0 (μ_B/f.u.)	3.63	3.51	3.85
Spontaneous magnetisation at 290 K	m_S (μ_B/f.u.)	1.58	2.04	1.56
Resistivity at 290 K	ρ ($\mu\Omega$ cm)	1000	4.5×10^8	5.5×10^6
Magnetoresistance in 1.2 T at 77 K (ceramic)	$(\Delta R)/R_0 \times 100$ %	-	15.0	13.3
Magnetoresistance in 50 mT at 290 K (ceramic)	$(\Delta R)/R_0 \times 100$ %		2.6	1.6
Magnetoresistance in 1.2 T at 77 K (powder)	$(\Delta R)/R_0 \times 100$ %	3.5	6	
Magnetoresistance in 50 mT at 290 K (powder)	$(\Delta R)/R_0 \times 100$ %	-	1	

Table4.Properties of A_2FeMoO_6; A=Ca, Sr, Ba.

Figure 4.1 shows that there is a significant difference in the morphology of the three samples. Given that all samples were prepared following the same procedure, the results obtained suggest that a systematic study of ceramic preparation should be done for each material in order to control the final grain structure. These different sample morphologies are reflected in the results obtained for the resistivity where a difference on the order of 10^6 is observed. One should remember that the range of temperatures covered by the resistivity measurements

of Figure 4.2 is well below T_C for all samples (the lowest value is for CFMO with T_C=345 K). CFMO has a resistivity of only 1 mΩ cm at room temperature, comparable to values obtained in perovskites of the manganese system [1]. This resistivity decreases slightly with decreasing temperature and the difference between the values measured in zero field and 0.3 T is negligible. A look at the microstructure of this sample shows a dense ceramic of large and well compacted grains (Figure 4.1 a) suggesting that both resistivity and MR are mostly of intrinsic origin. For the SFMO and BFMO ceramics the resistivity is much higher with values of 4.5×10^5 and 5.5×10^3 mΩ cm at room temperature respectively. Here the resistivity behaviour observed is clearly of extrinsic origin since the resistivity of a single crystal of SFMO is only 0.6 mΩ cm at room temperature [20]. This is further confirmed by the large difference between the values of resistivity obtained in zero field and 0.3 T. The approximately linear increase in MR with decreasing temperature is explained by intergrain spin dependent scattering when the magnetisation of the grains is aligned under the magnetic field.

The isothermic magnetoresistance also reflects the influence of the ceramic microstructure. All ceramics have a negative MR. CFMO shows no measurable magnetoresistance at room temperature or 77 K and 1.2 T. The SFMO and BFMO samples show 7% and 6% MR at room temperature respectively in 1.2 T, values that are higher than those obtained for any manganese perovskite in the same magnetic field [1]. The values obtained at 77 K and 1.2 T are 16% and 14% for SFMO and BFMO respectively. For these two samples there are two distinct MR regimes; a low field regime ($\mu_0 H$ smaller than 0.3 T) with a very sharp resistivity decrease of 5% for SFMO and 3% for BFMO. Above this field a smoother resistivity decrease is observed that becomes linear for $\mu_0 H \geq 0.6$ T at 77 K and $\mu_0 H \geq 0.4$ T at room

temperature. Above this value the resistivity versus field slope is the same in both samples. The high field slope arises from the progressive alignment of misplaced cations that tend to order antiferromagnetically with the surrounding matrix. In samples with a 13% Fe/Mo disorder this slope extends to fields as high as 8 T [10] while for a sample with 8% Fe/Mo anti-site defects [22] the magnetoresistance was found to be practically saturated in such fields. The most striking result from the present study is the value of 1% MR obtained at room temperature for the SFMO ceramic in only 20 mT making this material very attractive from the point of view of device fabrication.

Powder magnetoresistance was measured on the Ca and Sr samples. The microstructure of this powder is illustrated in Figure 4.5. The results obtained should be analysed by comparing the microstructure of bulk and powder samples. In general, the grinding procedure breaks the crystalline grains and introduces a much wider range of particle sizes. For the Ca sample it degrades the intergrain connections resulting in the introduction of an extrinsic resistivity and tunnelling between particles. This is not enough to produce a measurable magnetoresistance at room temperature but it gives rise to a value of 3.5 % MR at 77 K. For the SFMO ceramic, it was found that the powder ceramic is less resistive than the bulk and therefore the extrinsic contribution to MR is reduced from 7 % to only 1.3 % at room temperature and 1.2 T. The increase of the magnetoresistance at 0.3 T with resistivity associated with intergrain transport can be observed from the plot of Figure 4.22.

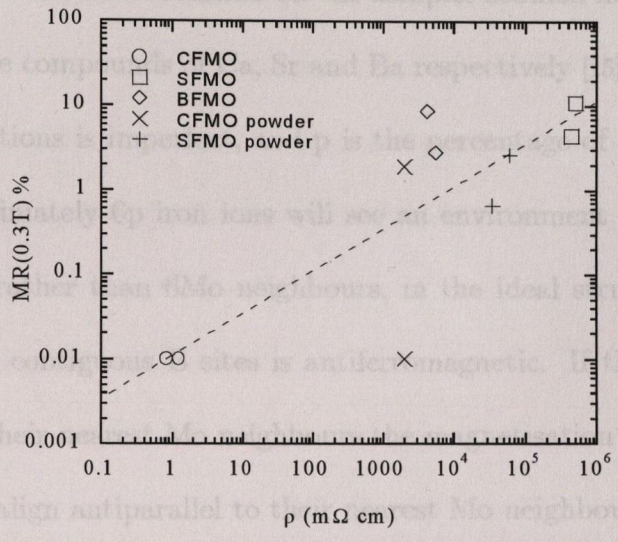


Figure 4.22. MR at 0.3 T as a function of zero field resistivity from 77 K and room temperature data. The dotted line is a guide to the eye.

The results encourage further work to tune the magnetoresistance by an appropriate manipulation of the microstructure. However, a significant improvement of the room temperature MR will require an increase of the Curie temperature by altering the oxide composition or stoichiometry and improving the Fe/Mo ordering. Any device applications will have to take into account the interplay between MR and resistivity.

The magnetisation curves of Figure 4.4 show that none of the samples reaches the full theoretical moment of 4 μ_B/f.u. The magnetisation of the Ba compound comes closest to the expected value. Possible explanations for the discrepancy include covalent mixing with the unpolarized 2p(O) orbitals, spin canting or imperfect cation order on alternate sites, together with antiferromagnetic coupling of iron ions in adjacent layers. A stoichiometric, ordered half-metallic ferromagnet must have a saturation magnetisation that is an integral number of Bohr magnetons because the number of electrons per formula is an integer, and the number of spin up (or spin down) electrons is also integral because of the gap in one or other

density of states. Mössbauer measurements on the samples studied here show 6, 7 and 2 % of anti-site defects in the compounds of Ca, Sr and Ba respectively [15]. If the NaCl-type ordering of Mo and Fe cations is imperfect, and p is the percentage of cations occupying the wrong site then approximately 6p iron ions will see an environment with (5Mo,1Fe) nearest cation neighbours, rather than 6Mo neighbours, in the ideal structure. The exchange between two Fe ions in contiguous B sites is antiferromagnetic. If the Mo misplaced ions are aligned parallel to their nearest Mo neighbours the magnetisation is given by M=(4-8p) μ_B/f.u. If the Mo ions align antiparallel to their nearest Mo neighbours, the magnetisation is M=(4-10p) μ_B/f.u. For M=(4-8p) μ_B/f.u. we get 3.44, 3.52 and 3.84 μ_B/f.u. for the Ca, Sr and Ba compounds and the measured values at 5 K are 3.63, 3.51 and 3.85 μ_B/f.u for Ca, Sr and Ba respectively. The agreement is very good for the Sr and Ba compounds. The calculated value for Ca_2FeMoO_6 is lower than the measured M_S. This difference can be explained by invoking the concept of antiphase boundaries. Unlike an isolated misplaced iron ion, which modifies the environment of six others, the iron in an antiphase boundary changes the environment of only two other iron ions. This difference permits a quantitative evaluation of the relative proportions of the two sorts of defects from the intensities of the Mössbauer sub-spectra. The hypothesis of only antiphase boundaries is quite inconsistent with the magnetization data of the Ca compound. The number of such defects would have to be 3p and the magnetisation is then approximately (4-30p) μ_B/f.u., giving 1.9 μ_B for the Ca compound. We conclude that point defects predominate. From the intensity of Mössbauer spectra, making the simplified assumption that all iron spins in 6 T are either parallel or perpendicular to the applied field, the percentage of iron ions that are aligned perpendicular to the field near the antiphase boundaries is only 2-3 %. The percentage of iron ions in

the boundaries should be approximately ~1% [15]. An estimate of f_5, the fraction of iron atoms that do not contribute to the magnetization in 5 T, is (4 - M_5)/4, where M_5 is the magnetization in 5 T in μ_B/f.u. Based on this idea, the smallest possible size of the antiphase domain, d_{ap} is approximately $12a/f_5$, where a is the lattice parameter (~0.8 nm). The lower limit to the antiphase domain size is of order 0.1 μm. From this value, we estimate the size of the antiphase domains to be ~0.5 μm [15].

4.3.2 Thin films

Table 4 summarises the properties of the thin films described above.

Sample Name	**Substrate**	**Substrate temperature (°C)**	**Appearance**	**Lattice parameter a=b (Å)**	**M_S at 20 K (μ_B/f.u.)**	**ρ_{300K} (mΩcm)**
stoA	$SrTiO_3$	950	black	5.631	3.5	2.2
stoB	$SrTiO_3$	900	black	5.633	3.5	2.9
stoC	$SrTiO_3$	770	black	5.671	1.4	6
mgoA	MgO	950	black	5.646	2.3	1.6
mgoB	MgO	720	black	5.646	1.4	2.9
mgoC	MgO	950 + oxygen annealing	yellow	5.646	does not saturate	insulating
mgoD	MgO	950 + vacuum annealing	black	5.646	2.3	2.5

Table5.Properties of SFMO thin films deposited by PLD.

All SFMO films are textured along the (220) direction with the c axis parallel to the substrate plane. It can be shown that this is the orientation that minimises the lattice mismatch between film and substrate. The lattice mismatch is calculated by using the expression

$$\frac{(a_{film}/2) - a_{sub}}{a_{sub}} \tag{22}$$

where a_{film} is the lattice parameter of SFMO and a_{sub} the lattice parameter of the substrate. Here we use the SFMO bulk values of $a = 5.573$Å and $c = 7.905$Å together with $a = 3.905$Å for $SrTiO_3$ and $a = 4.212$Å for MgO. Lets consider first the deposition on $SrTiO_3$. The

lattice mismatch between the SFMO lattice parameter a and the substrate is -28 %. Between the SFMO lattice parameter c and the substrate it is only +1.2 %. It is obvious that if the film grows with the c axis parallel to the substrate plane the strain is substantially minimised. Furthermore, because the films grow oriented along the (220) direction, the other SFMO lattice parameter in contact with the substrate is given by $\sqrt{2}a$ which has a lattice mismatch of only +0.91 % with $SrTiO_3$. The same applies for films deposited on MgO substrates. Here the lattice mismatch between c and MgO is -6%. The parameters $\sqrt{2}a$ has a lattice mismatch of -6% with MgO. It should be noticed that c=7.905Å and $\sqrt{2}a$ = 7.881Å have essentially the same size, suggesting that the film growth mimics the cubic structure of the substrates. Furthermore, the value of a is approximately 1.5 % larger than the bulk value for all films. This lattice distortion is most likely associated with a change in the size of c which can not be measured with the existing equipment.

AFM pictures of the films deposited at 950°C on MgO and 900°C on $SrTiO_3$ show that film growth is by island mode giving rise to rectangular grains separated by L shaped holes. All the holes observed are oriented along two perpendicular directions which probably reflect the orientation of the substrate a and b axis. Singh and Narayan [35] observed similar features in YBCO films grown on $SrTiO_3$ with the c axis parallel to the film plane and a axis perpendicular. This type of texture was obtained for films deposited at low substrate temperatures (T_S=650°C) where the authors also observe long rectangular holes defining square grains. The authors attribute this kind of film growth to the low oxygen content of the deposited films, for which the associated lattice distortion results in a better lattice match between the YBCO c axis and the substrate. The films deposited at 720°C on MgO (sample mgoB) and 770°C on $SrTiO_3$ show the same x-ray (220) texture as the other samples but

with a smooth surface with no holes and a surface roughness of only 2 nm, suggesting that layer by layer growth might take place at lower deposition temperatures. However, films deposited at these lower temperature have very poor transport and magnetic properties. The AFM scans on films deposited on $SrTiO_3$ show that the formation of holes occurs at an intermediate temperature range ($\sim 800 - 900^oC$) above and below which the films show flat surfaces. The data obtained for films deposited on MgO suggest that substrate temperatures above 950°C might be necessary to obtain films without holes.

The resistivity of thin films is very similar for both series of films. The samples deposited at higher temperatures on both substrates show a small temperature dependence of the resistivity which reaches a minimum between 100 and 150 K. The same feature has been observed in both thin film [33] [31] and ceramic samples [10].The films deposited at lower temperatures in both $SrTiO_3$ and MgO (stoC and mgoB) show semiconducting behaviour with a room temperature resistivity of 3 mΩcm in good agreement with the results reported by Westerburg et al. [31] for films deposited at T_S below 920°C. The semiconducting behaviour is attributed to a high degree of Fe/Mo disorder.

The film deposited at 950°C on MgO and annealed in oxygen (sample mgoC) forms a transparent, yellow and insulating phase. This yellow phase is observed in all films (on both MgO and $SrTiO_3$) deposited or annealed in O_2 or N_2. The effect of deposition or annealing in atmosphere is the degradation of the crystallinity of the films as confirmed by the broadening of the (220) reflection of sample mgoC compared to the rest of the samples. There is some phase segregation leading to $SrMoO_4$, an insulator with a yellow colour [37], which explains the appearance of the film. In addition, it is possible that there is a high degree of anti-site defects in these films as shown by the low saturation moment compared to other films de-

posited on MgO. The lack of saturation of magnetisation even at high magnetic fields at low temperature may be attributed to the presence of ferromagnetic clusters a spin-glass or paramagnetic matrix. AC magnetic susceptibility, magnetisation in field-cooled (FC) and zero field cooled (ZFC) could help determing the exact magnetic nature of these films.

Magnetisation data show that the best quality samples are obtained for films deposited on $SrTiO_3$. The magnetisation of films deposited on this substrate at 900 and 950°C reaches a saturation value of 3.5 μ_B/f.u. at 20 K and 1.5 T. Sample stoC deposited at a temperature of 770°C shows a much smaller saturation value with only 1.4 μ_B/f.u. at 20 K and 1.5 T. This low value is due to the formation of a more disordered phase at low deposition temperatures. All films deposited on $SrTiO_3$ have T_C well above 350 K as seen from the plots of magnetisation as a function of temperature of Figure 4.12. Isothermic magnetisation loops also suggest poor Fe/Mo ordering in the films deposited on MgO with the best values obtained for samples mgoA and mgoD with only 2.36 and 2.29 μ_B/f.u. respectively at 20 K. This suggests that higher deposition temperatures might be necessary in order to achieve ordered samples on MgO substrates with properties similar to those of bulk materials. Unfortunately, this is not possible in our system, where the maximum substrate temperature is 950°C.

The results suggest a low Fe/Mo order for films deposited on MgO substrates which can be overcome by deposition at higher temperatures. However, the formation of large L shaped holes at high temperatures is a serious obstacle to the use of this type of films for device applications since devices such as tunnel junctions require atomically flat surfaces. Films deposited on $SrTiO_3$ substrates have smooth surfaces, T_C well above 350 K and high saturation magnetisation and can become a successful alternative to $(La_{0.7}Sr_{0.3})MnO_3$ in the spin

electronics research area.

References

[1] J. M. D. Coey, S. von Molnar and M. Viret, Advances in Physics 48, 167, (1999).

[2] J. M. De Teresa, A. Barthélémy, A. Fert, J. P. Contour, R. Lyonnet, F. Montaigne, P. Seneor, A. Vaurès, Phys. Rev. Lett. 82, 4288, (1999).

[3] H.Y. Hwang, S. W. Cheong, N. P. Ong, B. Batlogg, Phys. Rev. Lett. **77**, 2041 (1996).

[4] J. M. D. Coey, Appl. Phys. Lett. **85**, 5576 (1999).

[5] J. M. Longo and R. Ward, J. Am. Chem. Soc. **83**, 1088, (1961).

[6] A. W. Sleight, J. M. Longo and R. Ward, Inorg. Chem. **1**, 245 (1962).

[7] F. Patterson, C. Moeller and R. Ward, Inorg. Chem. **2**, 196 (1963).

[8] F. S. Galasso, *Structure, Properties and Preparation of Perovskite Type Compounds*, Pergamon, Elmsford, New York, (1969).

[9] A. W. Sleight and J. F. Weiher, J. Phys. Chem. Solids **33**, 679 (1972).

[10] K. I. Kobayashi , T. Kimura, H. Sawada, K. Terakura and Y. Tokura, Nature **395**, 677 (1998).

[11] K. I. Kobayashi, T. Timura, Y. Tomioka, H. Sawada, K. Terakura and Y. Tokura, Phys. Rev. B. **59**, 11159 (1999).

[12] B. Garcia-Landa, C. Ritter, M. R. Ibarra, J. Blasco, P. A. Algrabel, R. Mahendiran and J. Garcia, Sol. Stat. Comms. **110**, 435 (1999).

[13] L. Pinsard-Gaudart, R. Suryanarayanan, A. Revcolevschi, J. Rodriguez-Caravaja, P. A. I. Smith, R. M. Thomas, R. P. Borges, J. M. D. Coey, J. Appl. Phys. **87**, 7118 (2000).

[14] R. P. Borges, R.-M. Thomas, C. Cullinan, J. M. D. Coey, R. Suryanarayanan, L. Ben-Dor, L. Pinsard-Gaudart, A. Revcolevschi, J. Phys.: Condens. Matter **11**, L445 (1999).

[15] J. M. Greneche, M. Venkatesan, R. Suryanarayanan, J. M. D. Coey, unpublished.

[16] J. Linden, T. Yamamoto, K. Karppinen, H. Yamauchi, T. Pietari, Appl. Phys. Lett. **76**, 2925 (2000),

[17] A. Maignan, B. Raveau, C. Martin and M. Hervieu, J. Sol. Stat. Chem. **144**, 224 (1999).

[18] C. L. Yuan, S. G. Wang, W. H. Song, T. Yu, J. M. Dai, S. L. Ye, Y. P. Sun, Appl. Phys. Lett. **75**, 3853 (1999).

[19] Ll. Balcells, J. Fontcuberta, B. Martinez, X. Obradors, Phys. Rev. B **58**, R14697 (1998).

[20] Y. Tomioka, T. Okuda, Y. Okimoto, R. Kumai, K.-I. Kobayashi, Y. Tokura, Phys. Rev. B **61**, 422 (2000).

[21] T. H. Kim, M. Uehara, S.-W. Cheong, S. Lee, Appl. Phys. Lett. **74**, 1737 (1999).

[22] D. D. Sarma, E. V. Sampathkumaran, R. Sugata, R. Nagarajan, S. Majundar, A. Kumar, G. Nalini, T. N. Guru Row, Solid State Communications **114**, 465 (2000).

[23] A. S. Ogale, S. B. Ogale, R. Ramesh, T. Venkatesan, Appl. Phys. Lett. **75**, 537 (1999).

[24] W. Prellier, V. Smolyaninova, A. Biswas, C. Galley, R. L. Greene, K. Ramesha and J. Gopalakrishnan, preprint.

[25] M. L. Rudee, D. T. Margulies, A. E. Berkowitz, Microsc. Microanal **3**, 126 (1997).

[26] J. B. Goodenough, R. I. Dass, Int. J. Inorg. Mat. **2**, 3 (2000).

[27] H. Q. Yin, J. S. Zhou, R. Dass, J. P. Zhou, J. T. McDevitt, J. B. Goodenough, J. Appl. Phys **87**, 6761 (2000).

[28] C. Ritter, M. R. Ibarra, L. Morellon, J. Blasco, J. Garcia, J. M. De Teresa, unpublished.

[29] T. Manako, M. Izumi, Y. Konishi, K.-I. Kobayashi, M. Kawasaki, Y. Tokura, Appl. Phys. Lett. **74**, 2215 (1999).

[30] H. Asano, S. B. Ogale, J. Garrison, A. Orozco, Y. H. Li, E. Li, V. Smolyaninova, C. Galley, M. Downes, M. Rajeswari, R. Ramesh, T. Venkatesan, Appl. Phys. Lett. **74**, 3696 (1999).

[31] W. Westerburg, D. Reisinger, G. Jakob, Phys. Rev. B **62**, R767 (2000).

[32] R.-M. Thomas, PhD Thesis, Trinity College Dublin 1999.

[33] R. Boucher et al, unpublished.
[34] E. Gommert, H. Cerva, J. Wecker, K. Samwer, J. Appl. Phys. **85**, 5417 (1999).
[35] R. K. Singh and J. Narayan, J. Appl. Phys. **67**, 3785 (1990).
[36] W. Westerburg, F. Martin, G. Jakob, J. Appl. Phys. **87**, 5040 (2000).
[37] *Handbook of Chemestry and Physics*, 53^{rd} edition, Cleveland, Ohio 1972.

Chapter 5

Devices

5.1 Introduction

Magnetic sensors differ from most other detectors in that they do not directly measure the physical property of interest. Devices that monitor properties such as temperature, pressure, strain, or flow provide an output that directly reports the desired parameter. Magnetic sensors, on the other hand, detect changes, or disturbances, in magnetic fields that have been created or modified, and from them derive information on properties such as direction, presence, rotation, angle, or electrical currents. The output signal of these sensors requires some signal processing for translation into the desired parameter. Although magnetic detectors are somewhat more difficult to use, they do provide accurate and reliable data, and above all, without physical contact [1].

Each type of sensor is active over a certain magnetic field range. Lenz [2] has classified these devices as low-field sensors (B<0.1 nT), Earth's field sensors (0.1 nT<B<1 mT) and bias magnet field sensors (B>1 mT). A list of the different technologies available with their respective field detection ranges is given in Figure 5.1.

Low field sensors are mainly used in medicine and scientific instruments. The most sensitive of these devices, and probably the most widely used one, is the SQUID magnetometer. It can detect fields of the order 10^{-13} Tesla making it a fundamental research tool in areas such as neurology given that the magnetic fields produced in the human brain are of this order of magnitude. This kind of devices require careful engineering to avoid the effect of the Earth's magnetic field. One of their main drawbacks is the low working temperature

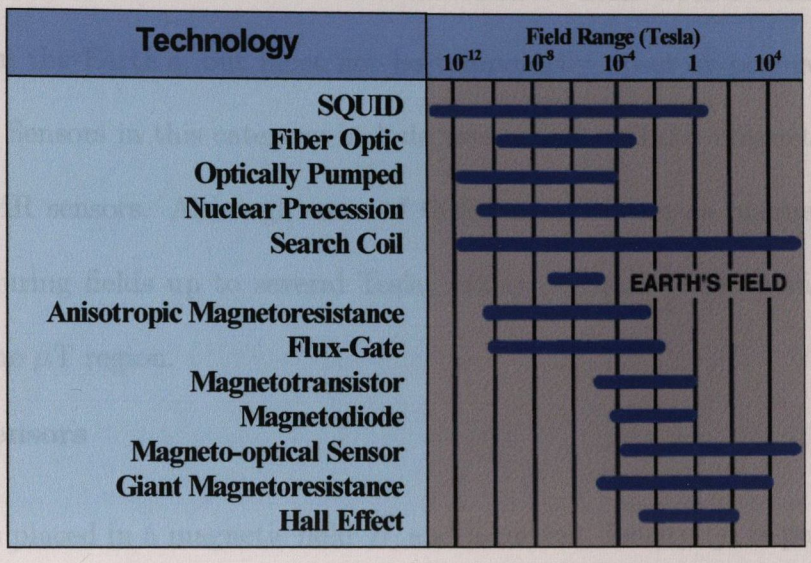


Figure 5.1. The field ranges for the different magnetic sensor technologies [1].

(~4 K) requiring cooling with liquid helium.

Earth's field sensors such as flux gate magnetometers are generally used in compass-based navigation systems. The most common type incorporates two coils, primary and secondary, wrapped around a common high permeability ferromagnetic core [3]. A drive signal applied to the primary coil with a frequency of the order of 10 kHz, causes the core to oscillate between magnetisation saturation points. In the presence of an external magnetic field, the magnetisation of the core element changes shifting the centre of oscillation. This is picked-up as a change in the amplitude of the secondary coil output signal. The signal can be demodulated with the appropriate electronics to obtain the value of the external applied field.

Bias magnetic field sensors are the most widely used in industrial applications. Most industrial sensors use permanent magnets as a source of the magnetic field to be detected. These magnets magnetise, or bias, ferromagnetic objects close to the sensor, which then detects

changes in the total field around itself. Bias field sensors must detect fields that are typically larger than the Earth's, but must not be temporarily upset or permanently affected by a large field. Sensors in this category include reed switches, InSb magnetoresistors, Hall devices, and GMR sensors. Although some of these sensors, such as magnetoresistors, are capable of measuring fields up to several Tesla, others, such as GMR devices, can detect fields down to the μT region.

5.1.1 Hall sensors

When a metal is placed in a magnetic field $\overrightarrow{H}$ and a current density $\overrightarrow{j}$ is passed through it a transverse electric field $\overrightarrow{E}_H$ develops given by

$$\overrightarrow{E}_H = R_H \overrightarrow{B} \times \overrightarrow{j} \tag{23}$$

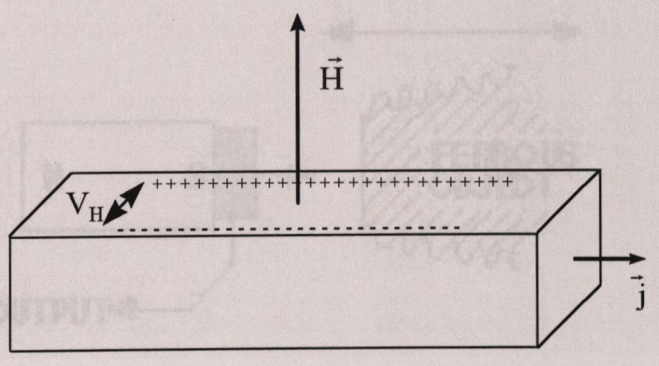


Figure 5.2. Hall effect.

The origin of the effect is the Lorentz force $\overrightarrow{F}$=-$e\overrightarrow{v} \times \overrightarrow{B}$ where e is the charge of the carriers and $\overrightarrow{v}$ their velocity [4].

A Hall sensor uses a geometry similar to that shown in Figure 5.2. Charge carriers are deflected to the side and build up until they create a Hall voltage across the slab with a

force equalling the Lorentz force on the charge carriers. At this point the charge carriers travel the length in approximately straight lines, and no additional charge builds up. Since the final charge carrier path is essentially along the applied electric field, the end-to-end resistance changes little with the magnetic field. When the Hall voltage (V_H) is measured between electrodes placed at the middle of each side, the resulting differential voltage is proportional to the magnetic field perpendicular to the slab. It also changes sign when the sign of the magnetic field changes. The ratio of the Hall voltage to the input current is called the Hall resistance, and the ratio of the applied voltage to the input current is called the input resistance.

It is clear from the description of the Hall effect that a change in direction or magnitude of the magnetic field can be seen as a change in Hall voltage. This is the working principle of Hall sensors and it is illustrated in Figure 5.3. A ferrous object coming close to the sensor,

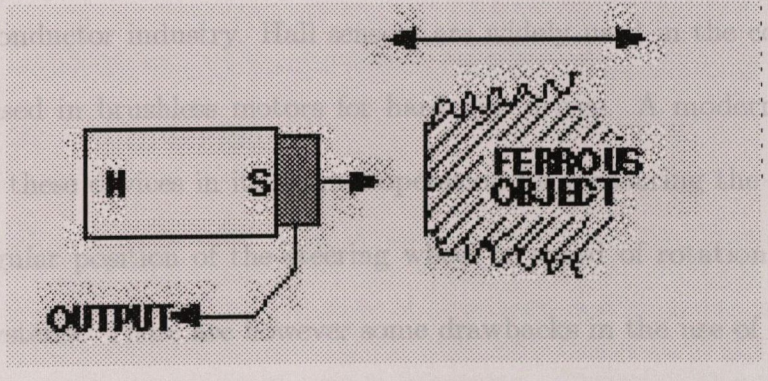


Figure 5.3. Schematic representation of the operation of a commonly used magnetic sensor (Hall or GMR) with biasing magnet.

e.g. a finger of a rotating gearwheel, will concentrate and increase the field produced by the bias magnet. The Hall voltage increases linearly with applied field and fields from 0.1 mT to several Tesla can be detected depending on the device characteristics. Most applications are in the low field region where these devices can be used to monitor the speed of rotation

of shafts and gearwheels or the position of mechanical parts.

The materials used to fabricate Hall sensors are generally n-type silicon for low cost applications or GaAs for higher temperature applications due to its large band gap. Materials such as InAs and InSb are becoming popular due to their high carrier mobilities (greater sensitivity) and higher frequency response. The temperature dependence of V_H and the input resistance is governed by the temperature dependence of the carrier mobility and Hall coefficient. Different materials and doping levels result in trade-offs between sensitivity and temperature dependence as can be seen from the datasheets of any of these sensors.

Magnetic field sensors based on the Hall effect are probably the most widely used sensing devices with more that 2 billion being sold world wide every year [5]. Such success is in great part due to their almost perfect compatibility with microelectronic technology. The optimal material properties, device structures and dimensions and fabrication processes are similar to those of semiconductor industry. Hall sensors are widely used in the computer industry where they are used in brushless motors for hard disc drives. A modern car depends on nearly a dozen of these devices in its normal operation for measuring the speed of rotation of shafts, the angular position of the steering wheel or speed of rotation of the wheels in anti-lock brake systems. There are however some drawbacks in the use of Hall sensors such as a low signal to noise ratio and low temperature stability. They are two part sensors, which require a permanent magnet as well as the Hall field detector, which can lead to potential alignment difficulties as well as increasing the final total price of the device. The low signal to noise ratio can be overcome by using the Hall sensor in an integrated circuit which implies an increase in the cost of the sensor.

5.1.2 GMR sensors

The basics of GMR and some devices based on this effect have been described in chapter 1. In that chapter we focused mainly on information technology applications where these devices have enjoyed tremendous success.

They have also entered the car industry where they compete with the Hall sensors for essentially the same tasks. They have a better signal to noise ratio and temperature stability than Hall sensors. However, because they are based on metallic multilayers, they require extra fabrication processing beyond the semiconducting industry standards which can make them less attractive.

GMR sensors share with Hall sensors the need for a biasing permanent magnet that normally represents half the cost of the device. Any type of sensor capable of reproducing the characteristics of Hall or GMR sensors without the need for a magnet would therefore have huge potential for applications in the automotive industry.

5.1.3 Manganite based devices

The finding of half-metallicity and a large magnetoresistance in manganese perovskites opened new perspectives for the fabrication of spin memory elements with the possibility of effective ON/OFF switching in tunnel junctions. However, there is evidence that magnetic disorder at the interfaces of thin film samples leads to full depolarisation of the current making their application impossible [6] [7] [8]. The double perovskite series, of which Sr_2FeMoO_6 and Sr_2FeReO_6 were predicted to be half-metals [9] [10] with T_C above 400K, could possibly overcome the limitations of the manganese compounds. Another possibility is the Heussler alloy Mn_2VAl for which Weht and Pickett [11] have predicted half-metallic behaviour together with T_C=800 K. This alloy has recently been studied in Trinity College,

Dublin but to this date, the MR values obtained are only of the order of 0.1% in 1 Tesla at room temperature [12].

There is still scope for a variety of applications of manganese perovskites in sensor technology. Xu et al. [13] [14] have developed a magnetic field sensor using polycrystalline ceramics of LCMO, LSMO and LBMO. The sensor consists of a ceramic bar of $8\times0.8\times0.14mm^3$ with four electrical contacts and placed on an Al_2O_3 base plate. The operation is based on the magnetoresistance of the materials. Magnetic fields are applied in three directions respective to the current: longitudinal, transverse (in plane field, normal to the current) and perpendicular (field perpendicular to sample plane). The sensors show variations in resistivity of 20% at 77 K and 1.5% at 298 K in fields of 700 Oe. Corresponding field sensitivities as high as 170%/T at 3 mT and 298 K, and 800%/T at 5 mT and 77 K can be obtained. The high field MR is independent of the mutual orientation of magnetic field and current. Direction sensitivity can be obtained due to the strongly anisotropic low field MR, which depends on the relative orientation of the field.

Another magnetic field sensor based on manganese perovskite materials has been developed by Coey et al. [15]. The sensor is a ceramic piece, polished to a spherical shape to minimise the demagnetising factor, with two current and two voltage contacts. The device senses the magnitude of an applied field from the decrease in the resistivity of the ceramic.

A recent development is the contactless potentiometer developed by Balcells et al [16] fabricated from printable inks of LSMO ceramic powder and a highly refractive insulating material. The relative concentration of the LSMO/insulator mixture has been investigated in order to optimize the magnetoresistive response. This ink is used to define four resistive tracks each one being one arm of a Wheatstone bridge. A variable magnetic field will change

the resistance of each track differently according to their relative orientation. This device can be used to measure angular position and works at room temperature.

5.2 A versatile microwave sensor

The device presented here is a novel type of position and motion sensor. It was originaly designed to make use of the narrow hysteresis loop of LSMO (see Figure 3.8 b) in a fashion similar to the flux gate magnetometer described in section 5.1. The microwave electronics were designed to perform the dual function of driving the magnetisation oscillation and picking up the signal. However, in the version of the device presented in this work, it was found that the electronics are capable of performing the detection function on their own. In a similar implementation of the device, where the sensitive probe is a small copper solenoid whose core can be filled with any chosen material, it was shown that the use of a LSMO bulk ceramic can indeed enhance the output signal when detecting magnetic objects [19]. Due to its characteristics it is a very versatile sensor that is capable of detecting the motion of a wide range of materials, such as magnetic and non-magnetic metals, ceramics and plastics. It can also detect continuous and discontinuous fluid flow. The device operation is described below.

The sensitive probe of the device is a single-turn flat coil made of a conducting material. A basic block diagram of the whole device is given in Figure 5.4. The sensitive coil is part of a microwave (f = 3 GHz) closed loop containing an amplifier, a non-linear element and a detector. In the implemantation described here all these functions are performed by a GaAs metal semiconductor field effect transistor (MESFET). The mechanical part to be detected, e.g. a gearwheel, is rotated near the coil. Each time a finger of the gearwheel passes the sensitive volume of the coil it causes an electromagnetic loss that is detected by the resonant

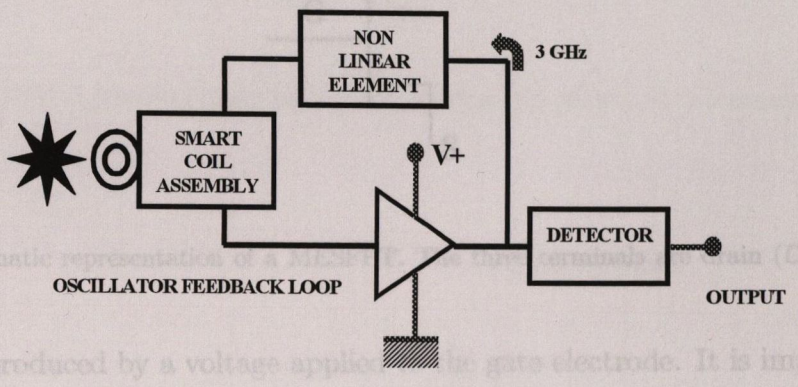


Figure 5.4. Diagram of the microwave motion sensor.

circuit and converted to an output signal on an oscilloscope. The amplifier also feeds back the signal into the circuit and the non-linear element sets the coil voltage to a value that depends on the electromagnetic losses in the loop. The bandwidth of the circuit is limited by the response time of the DC signal amplifier which amplifies the signal output. The distinguishing feature of this device is that the detection is made through a variation of the quality factor (Q) of the coil rather than the change in frequency at resonance.

In practice, the device is divided into two component circuits: the sensor circuit and a control circuit described below.

5.2.1 The sensor circuit

The sensor circuit centres around a NE72089 GaAs (MESFET) as the active component [17]. This MESFET is capable of sustaining oscillation up to frequencies of about 10 GHz. The GaAs MESFET used in the present sensor is an n-channel three terminal (source, drain and gate) device represented in Figure 5.5. Conduction between drain and source is controlled by

conductance

$$g_m = \left(\frac{\partial I_D}{\partial V_G}\right)_{V_{DS}} \tag{24}$$

Figure 5.6 shows how a small change in V_G can have a big effect on the current flow between drain and source.

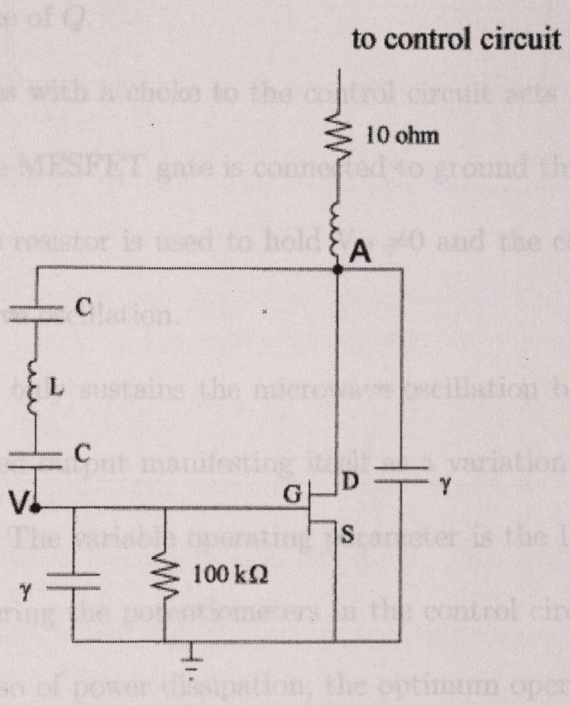


Figure 5.7. Diagram of the sensor circuit. The inductance L corresponds to the single turn coil.

The sensor circuit is represented in Figure 5.7. It is an auto-oscillator in which the GaAs MESFET plays a dual role: sustaining the oscillation and detecting the electromagnetic losses in the coil. This circuit is a standard Colpitts high-frequency oscillator with the resonant circuit connected between drain and gate of the GaAs MESFET. The resonant circuit can be tuned to the desired operation frequency (in this case is in the low microwave range) by an appropriate choice of values of R, L and C. The quality factor Q of the resonant

circuit is given by

$$Q = \frac{\omega L}{R} \tag{25}$$

where ω is the oscillation frequency and L and R are respectively the coil inductance and resistance (see Appendix A). It will be shown below that the signal in this device derives from a change in the value of Q.

The 10 Ω resistor in series with a choke to the control circuit acts as a stopper to prevent parasitic oscillations. The MESFET gate is connected to ground through a 100 kΩ resistor and a capacitor (γ). The resistor is used to hold $V_G \neq 0$ and the capacitor provides a loss free path for the microwave oscillation.

The GaAs MESFET not only sustains the microwave oscillation but also acts as a signal detector, with the detected output manifesting itself as a variation of the GaAs MESFET DC drain current $<I_D>$. The variable operating parameter is the DC drain-source voltage which may be set by altering the potentiometers in the control circuit. From the point of view of sensitivity and also of power dissipation, the optimum operating conditions are for $<V_{DS}>$ between 1.8 and 2.0 V [17]. When the circuit oscillates, the gate self-biasses by an amount comparable with the microwave amplitude V_0. When an object passes near the coil, the amplitude V_0 falls and the consequent rise in V_G contributes to an increase in the average drain current $<I_D>$. The corresponding signal output observed on the oscilloscope screen is negative. In our circuit, the measured gate voltage at $<V_{DS}>=2$ V is approximately -1.7 V. Given that the gate conducts for $V_{GS}>+0.3$ V this implies $V_0 \backsim <V_{DS}>$. The relation between the DC current I_D and the microwave oscillation in this circuit is a subtle but important one which Figure 5.8 tries to clarify. In normal oscillation, the microwave amplitude is ~2 V and there is conduction between drain and source every time the gate

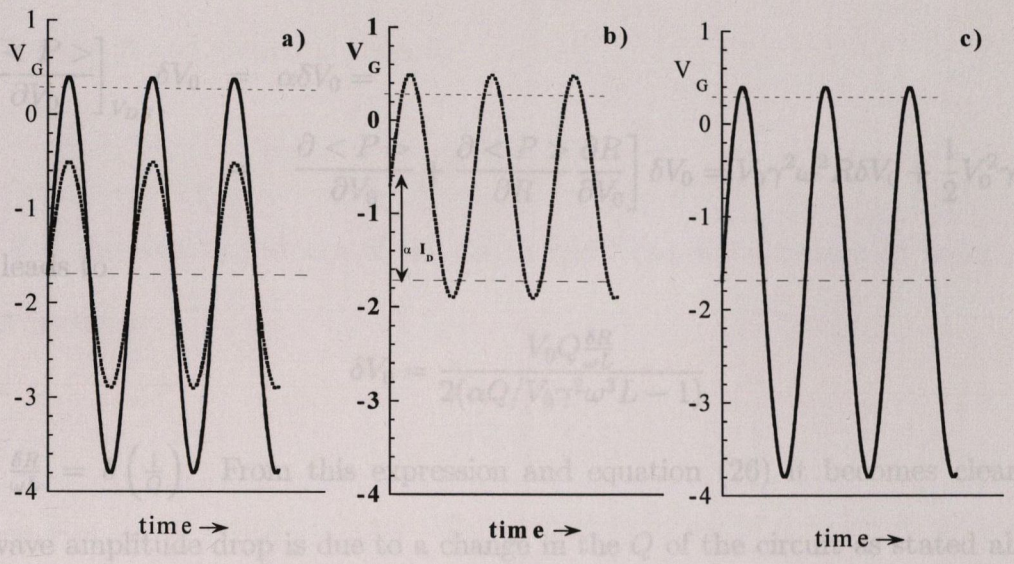


Figure 5.8. Detection of an object by the sensor.

voltage exceeds +0.3 V (Figure 5.8a)). When an object approaches the coil, the circuit losses increase and the microwave amplitude decreases (dotted sine wave in Figure 5.8a)) in such a way that V_G is always below the conduction threshold. This leads to a reduction of V_{DS} that the control circuit detects and tries to correct by dumping more current on the drain. This extra current supplied by the control circuit registers as signal output. Once the object leaves the coil sensitive volume the microwave amplitude goes back to its initial value of ~2 V (Figure 5.8c)) and the current supplied to the drain by the control circuit is reduced to its pre-resonance value.

One should now analyse in more detail the microwave amplitude drop at resonance. Under steady state conditions the net power delivered by the GaAs MESFET $< P >$ is equal to the power dissipated in the resonant circuit $< P' >= \frac{1}{2}V_0^2\gamma^2\omega^2 R$ (Appendix A), where R is

the resistance of the coil. This implies

$$\left.\frac{\partial < P >}{\partial V_0}\right]_{V_{DS}} \delta V_0 = \alpha \delta V_0 =$$

$$= \left[\frac{\partial < P >}{\partial V_0} + \frac{\partial < P >}{\partial R}\frac{\partial R}{\partial V_0}\right] \delta V_0 = V_0 \gamma^2 \omega^2 R \delta V_0 + \frac{1}{2} V_0^2 \gamma^2 \omega^2 \delta R$$

which leads to

$$\delta V_0 = \frac{V_0 Q \frac{\delta R}{\omega L}}{2(\alpha Q / V_0 \gamma^2 \omega^3 L - 1)} \tag{26}$$

where $\frac{\delta R}{\omega L} = \delta\left(\frac{1}{Q}\right)$. From this expression and equation (26) it becomes clear that the microwave amplitude drop is due to a change in the Q of the circuit as stated above. Furthermore, the electromagnetic losses at resonance are equivalent to a variation of the coil resistance R. The operation of the circuit will be demonstrated below for detection of magnetic and dielectric materials. It can be shown (Appendix A) that in the magnetic case $\delta\left(\frac{1}{Q}\right) = \eta\chi''$ where η is the filling factor of the coil and χ'' the imaginary part of the magnetic susceptibility. In the dielectric case $\delta\left(\frac{1}{Q}\right) = \eta\chi_e''$ where χ_e'' is the imaginary part of the electric susceptibility.

This circuit can be analysed by studying the equivalent low frequency circuit shown in Figure 5.9. This will allow a correct choice of the values of capacitance, inductance and resistance

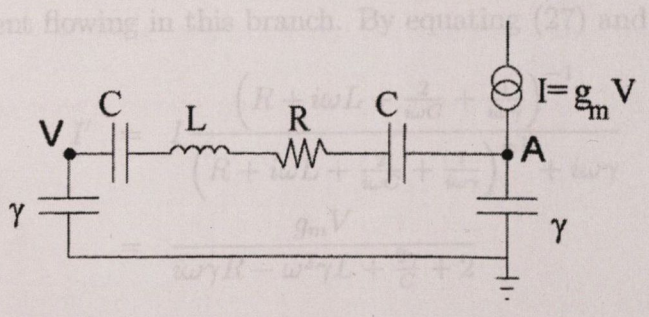


Figure 5.9. The equivalent of the circuit of Figure 5.7.

of the circuit. Point V in Figures 5.7 and 5.9 is the same in both circuits. The potential drop between point A and ground is given by

$$V = ZI \tag{27}$$

where Z is the total impedance of the circuit and I the input current in point A. Z for a parallel circuit is

$$\frac{1}{Z} = \frac{1}{Z_1} + \frac{1}{Z_2} \tag{28}$$

where Z_1 and Z_2 are respectively the left and right branches of the circuit. In this circuit

$$Z_1 = R + i\omega L + \frac{2}{i\omega C} + \frac{1}{i\omega\gamma} \tag{29}$$

and

$$Z_2 = \frac{1}{i\omega\gamma} \tag{30}$$

The voltage drop given in equation (27) is equal to the voltage drop across the left branch of the circuit

$$V = Z_1 I' \tag{31}$$

where I' is the current flowing in this branch. By equating (27) and (31) we get

$$I' = I\frac{\left(R + i\omega L + \frac{2}{i\omega C} + \frac{1}{i\omega\gamma}\right)^{-1}}{\left(R + i\omega L + \frac{2}{i\omega C} + \frac{1}{i\omega\gamma}\right)^{-1} + i\omega\gamma} \tag{32}$$

$$= \frac{g_m V}{i\omega\gamma R - \omega^2\gamma L + \frac{2\gamma}{C} + 2} \tag{33}$$

The potential developed by I' across γ must be greater than or equal to V

$$\frac{I'}{i\omega\gamma} = \frac{-g_m V}{2i\omega\gamma - \omega^2\gamma^2 R - i\omega^3\gamma^2 L + \frac{2i\omega\gamma^2}{C}} \geqslant V \tag{34}$$

component	value
C	2.2 pF
γ	47 pF
L	4.5 nH
R	0.3 Ω
g_m	5×10^{-3} mho

Table6.The electronic components incorporated in the oscillator and their values

The complex part of the denominator vanishes

$$2\omega\gamma - \omega^3\gamma^2 L + \frac{2\omega\gamma^2}{C} = 0 \tag{35}$$

from which we get

$$\omega^2 = \frac{2\gamma + \frac{2\gamma^2}{C}}{\gamma^2 L} = \frac{1}{LC^*} \tag{36}$$

where $C^* = \frac{2}{C} + \frac{2}{\gamma}$. From the real part we get the oscillation condition

$$g_m \geqslant \omega^2\gamma^2 R \tag{37}$$

from which we get

$$R \leqslant \frac{g_m}{\omega^2\gamma^2} \tag{38}$$

From equations (36) and (38) we can chose values of γ, C and R that will make the oscillator work at the desired operation frequency. In this case the value chosen was f ~3 GHz. The values of the capacitors and the resistance and inductance of the coil are shown in the table. Figure 5.10 shows the sensor circuit mounted on a copper plate. The diameter of the coil is 2 mm.

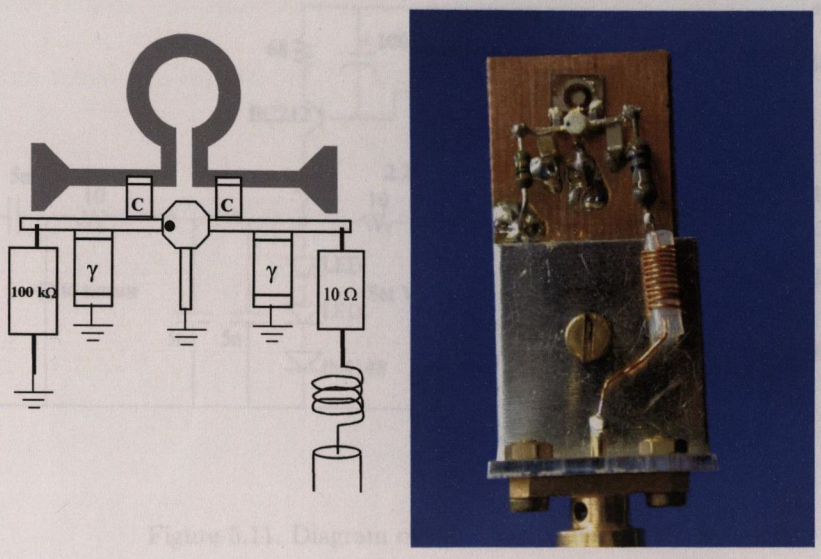


Figure 5.10. Left: diagram of the sensor circuit; right: the sensor circuit assembled on a copper plate.

The magnetic field produced by the coil can be obtained from the expression

$$L = \frac{AB}{I} \tag{39}$$

where L is the inductance of the coil, A the area of the coil, B the magnetic field and I the current. The current I can be found from the voltage at point V of Figure 5.12

$$V = \frac{1}{i\omega} I \tag{40}$$

so that

$$B = \frac{i\omega LV}{A} \tag{41}$$

and by using a value of 0.3 V for the maximum voltage at point V we get values of I = 0.26 A and B = 0.4 mT as the magnetic field produced by the coil.

5.2.2 The control circuit

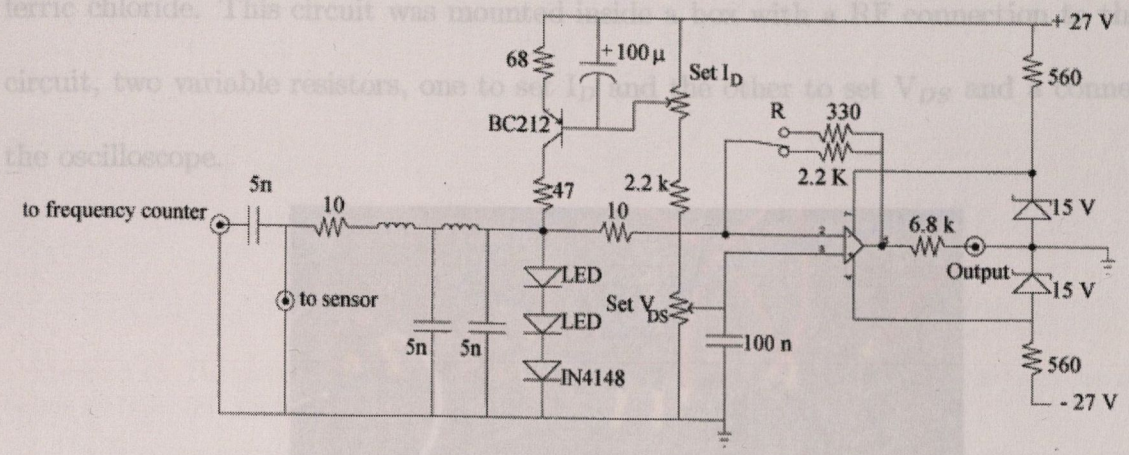


Figure 5.11. Diagram of the control circuit.

The control circuit is shown in Figure 5.11. The essential features are a variable current source that provides current in the GaAs MESFET drain and a 741 operational amplifier (OPA) which is set to survey the MESFET drain voltage and which corrects for deviations of V_{DS} from the set voltage (applied to the operational amplifier positive input) by adding to or subtracting from the current supplied by the current source. The extent of the correction which it may apply is set by the feedback resistor R_F and the power rails of the operational amplifier. If the OPA loses control, the two light emitting diodes (LED) in series with a silicon signal diode across the GaAs MESFET feed ensure that the drain voltage remains within safe limits and give external warning in case of circuit malfunctioning. When the circuit detects an object, the current taken by the GaAs MESFET varies and this is reflected by an excursion of the OPA output. The larger the value of R_F the greater the signal amplification but the less the current range over which the OPA maintains control, hence the option of changing R_F to a smaller value to cope with large absorptions without stopping the oscillator. A view of the control circuit is shown in Figure 5.12. The control circuit was assembled on

a copper circuit board with the contacts between components defined by wet etching with ferric chloride. This circuit was mounted inside a box with a RF connection to the sensor circuit, two variable resistors, one to set I_D and the other to set V_{DS} and a connection to the oscilloscope.

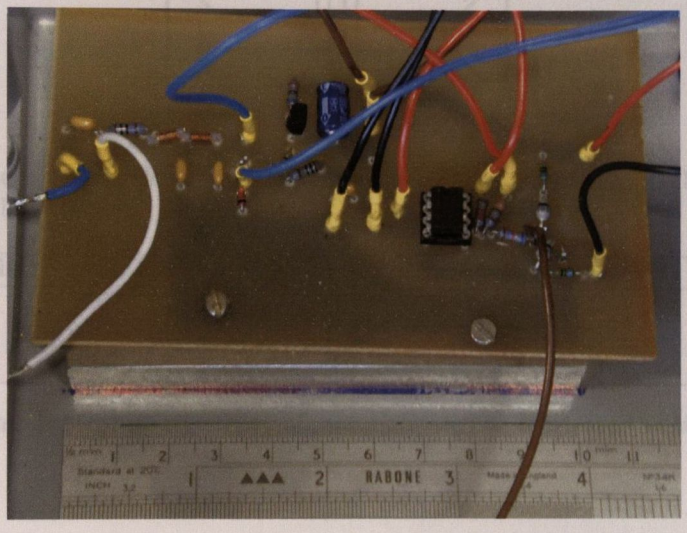


Figure 5.12. View of the assembled control circuit. Contacts between the components are defined by wet etching at the back of the plate.

5.3 Results and applications

Three different sensor circuits were assembled in small rectangular pieces of copper circuit board (4×2 cm^2). The components used were chip capacitors and resistors, normal resistors, the GaAs MESFET and a single turn coil made from a metallic thin film deposited on a substrate. The difference between each circuit is the material of which the coil is made. The sensor is connected to the control circuit through a choke to avoid parasitic oscillations.

The single turn coil is defined on a metallic film by UV lithography. A mask was designed containing Ω shaped single turn coils of different sizes. The coil chosen and its dimensions is represented in Figure 5.13. The inductance of a solenoid can be calculated from the expression

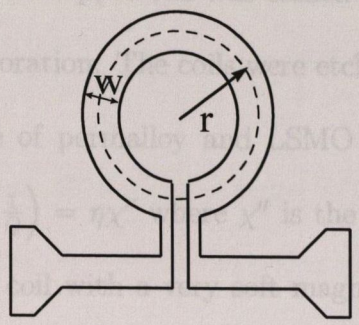


Figure 5.13. The pattern used to define the single turn coil. Dimensions used in this work are an average radius r=1mm and width w=0.6mm

material	resistivity ($\mu\Omega cm$)	coil thickness (μm)	resistance (Ω)	signal/noise
LSMO/Cu	100/1.67	0.3	0.7	100
Permalloy	8	0.4	2.3	58
Copper	1.67	0.2	1.3	71

Table7.Room temperature resistivity of materials used to fabricate the single turn coil

[18]

$$L(\mu H) = \frac{5.08 \times N^2 \times d}{3.5 + 8(l/d)} \tag{42}$$

where N is the number of turns, d the coil diameter in milimeters and l the length of the solenoid. For a flat coil l/d is very small so that the coil dimensions used in this work produce an inductance of 4.5 nH. According to equation (38) the coil resistance should not exceed 0.5 Ω if one wishes to work at a frequency of 3 GHz. The coil resistance is set by its thickness depending on the resistivity of the material used. The three coils used here are made of LSMO/Cu, permalloy and copper whose resistivities at room temperature are given in the table.

The LSMO coil was etched on a 12 nm thick LSMO film deposited by PLD on a MgO substrate. Due to the high resistivity of LSMO, the oscillation condition (equation (37)) can only be satisfied by depositing a copper overlayer before etching for conduction of the microwaxe signal. The permalloy coil was etched from a permalloy film deposited on a silicon

wafer by electrodeposition and the copper coil was etched on a copper film deposited on a MgO substrate by thermal evaporation. The coils were etched by ion beam milling.

The motivation behind the use of permalloy and LSMO coils comes from the fact that the signal is proportional to $\delta\left(\frac{1}{Q}\right) = \eta\chi''$ where χ'' is the imaginary part of the magnetic susceptibility. By fabricating a coil with a very soft magnetic material (narrow hysteresis loop) where a small magnetic field can vary the susceptibility from a very high value to $\chi \sim 0$ (by reaching magnetisation saturation in the coil) an extra loss is being added to the system, and therefore the output signal and signal to noise ratio could be magnified. However, we found that the differences in signal/noise of the different coils can be accounted for by the resistance of the coils only. The signal/noise was measured by dividing the signal amplitude read on the oscilloscope screen by the amplitude of flat signal obtained when the gearwheel is stoped. The values shown in the table refer to the metallic gearwheel rotating with an angular velocity of 2000 rpm at a distance of 5 mm from the coil.

In a different implementation of the device, using a multiturn copper coil inside which a piece of bulk magnetic material can be placed, it was found that the presence of the magnetic material significantly improves the detection of magnetic materials [19] with the best results being obtained for $(La_{0.7}Sr_{0.3})MnO_3$ and Sr_2FeMoO_6. In the case of the flat coil, the amount of magnetic material is $\sim 10^{-7}$g, too small to have an effect on the signal. All the data shown in the sections below refer to the LSMO coil since it is the one whose resistance is closest to that imposed by the oscillation condition (equation (38)).

The figure of merit in any device is the signal to noise ratio. The origin of noise in oscillators was studied by Robinson [20] [21]. In the Colpitts oscilator the noise takes the form of

Josephson noise

$$V_n = \left(\frac{4k_B T F \Delta f Q}{\omega C}\right)^{1/2} \tag{43}$$

where k_B is the Boltzman constant, T the temperature, F the noise figure of the circuit and Δf the bandwidth imposed by the control amplifier and the signal amplitude is given by

$$V_s = V_0 \frac{\delta Q}{Q} = V_0 Q \delta \left(\frac{1}{Q}\right) = V_0 Q \eta \chi'' \tag{44}$$

so that the signal to noise ratio is

$$\frac{V_s}{V_n} = V_0 \eta \chi'' \left(\frac{\omega C Q}{4k_B T F \Delta f}\right)^{1/2} \tag{45}$$

A few observations can be made from the expression above. There are five variables that can be changed by the user in order to improve the signal to noise ratio: V_0, χ'', ω, C, Q and Δf. This allows the circuit a very flexible operation, with the ability to tune the signal to noise ratio depending on the desired operation or the demands of the sorrounding environment. An example of circuit tunning by changing some of these parameters is given in Appendix C.

5.3.1 Detection of mechanical parts

Here we show the operation of the device as an angular velocity and position sensor for a metallic gearwheel. The gearwheel used here is shown in Figure 5.14 on the right. The device was tested by rotating the gearwheel in the vicinity of the coil. The optimal signal was found by rotating the gearwheel at 1000 rpm at a distance of 5 mm from the coil and changing the settings of I_D and V_{DS} until the maximum signal amplitude is observed on the oscilloscope screen.



Figure 5.14. Gearwheels used for angular velocity and position sensing. They are made of plastic (left) and mild steel (right).

The gearwheel is connected to a DC motor and is rotated in front of the coil as shown in Figure 5.15. A typical oscilloscope trace obtained for the rotation of the mild steel gearwheel



Figure 5.15. The experimental set-up for measuring angular velocity and position of the fingers of a mild steel gearwheel.

is shown in Figure 5.16. Each peak in this trace corresponds to the passage of a finger of

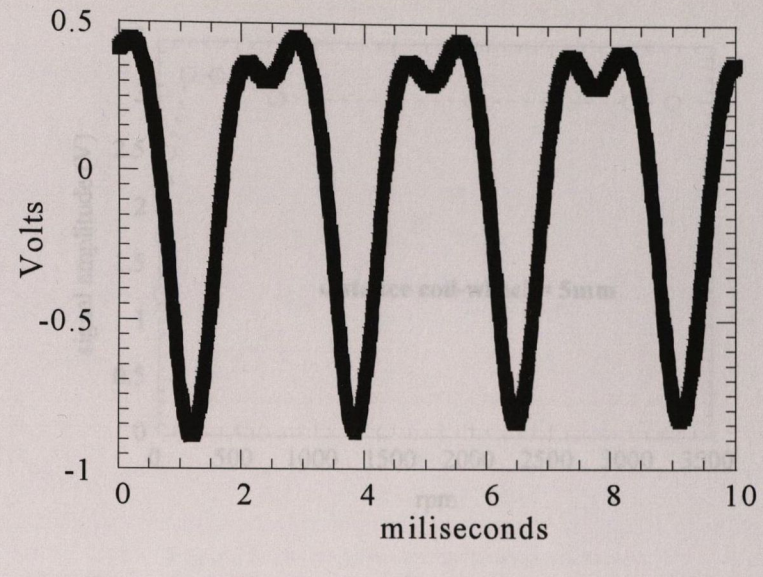


Figure 5.16. Oscilloscope trace obtained by rotating a mild steel gearwheel in front of the coil.

the gearwheel in the sensitive volume of the coil which allows effective position detection. From the signal we can find a value of 3000 rpm for the angular velocity. The signal is speed independent above 200 rpm. Below this, it decays quickly but it still has a magnitude of 1.2 V, that is, between 3000 rpm and 15 rpm the speed decreases by a factor of 200 and the signal by only a factor of 2 (Figure 5.17). The low speed decrease in amplitude can be corrected by an appropriate tuning of the circuit, more specifically by increasing the total capacitance of the circuit which leads to a decrease of the cut-off frequency. Therefore, for a given application the detection can become speed independent with the proper circuit tuning.The signal amplitude dependence on the distance between the coil and the gearwheel is shown in Figure 5.18. The signal decays with increasing distance between the coil and the gearwheel. For distances below 2 mm the signal is very irregular due to the complexity of the near field electromagnetic pattern, in similarity to what is observed in radio antennas and emitters.

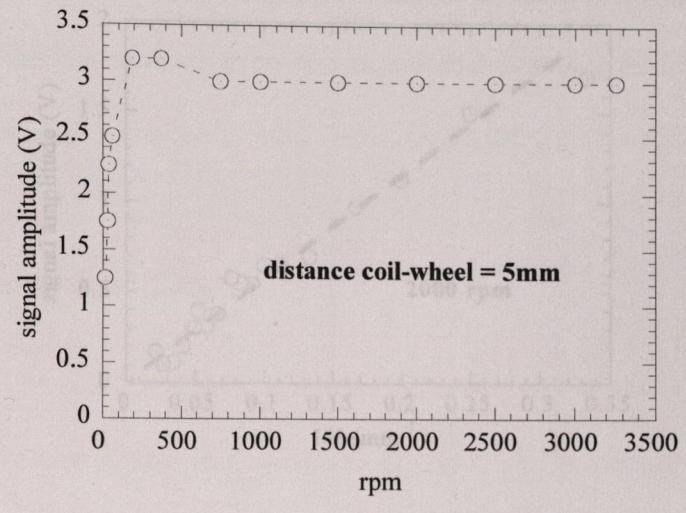


Figure 5.17. The signal amplitude versus angular speed.

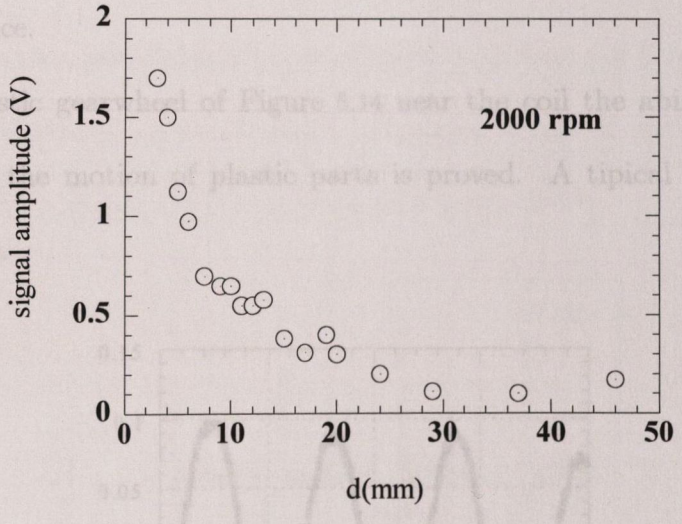


Figure 5.18. Signal amplitude versus distance.

The signal dependence on the distance is better illustrated by the plot of signal versus inverse distance of Figure 5.19.

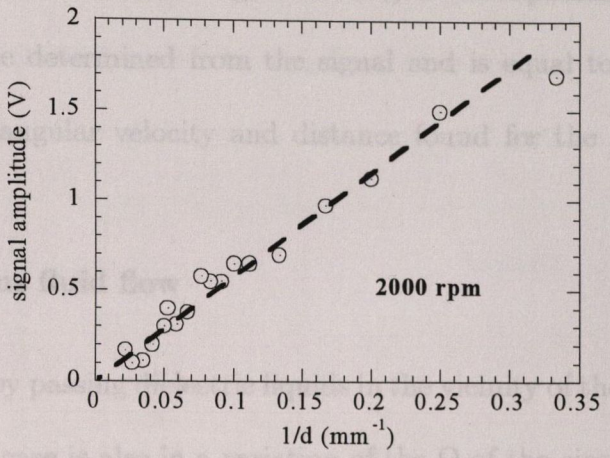


Figure 5.19. Signal versus inverse distance

It is clear that there is a well defined linear dependence of the signal amplitude with the inverse of the distance.

By rotating the plastic gearwheel of Figure 5.14 near the coil the ability of the device to detect and monitor the motion of plastic parts is proved. A tipical oscilloscope trace is shown in Figure 5.20.

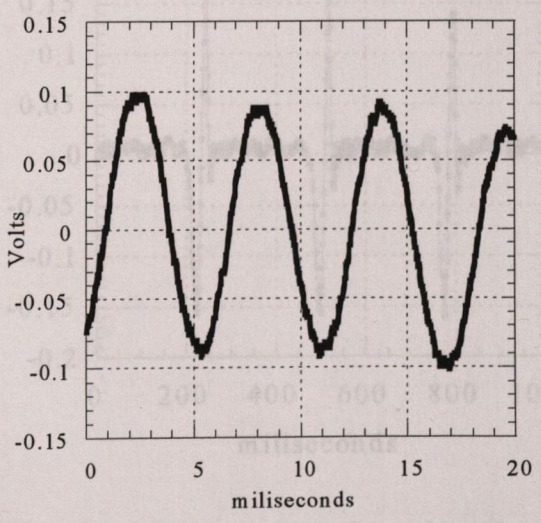


Figure 5.20. A typical osciloscope trace obtained with the plastic gearwheel of Figure 5.14.

Each peak corresponds to one of the fingers of the gearwheel passing near the coil and the angular velocity can be determined from the signal and is equal to 1200 rpm. The same signal dependence on angular velocity and distance found for the detection of the metal wheel apply here.

5.3.2 Discontinuous fluid flow

The device was tested by passing dielectric liquids in the vicinity of the coil. The origin of the signal in the dielectric case is also in a variation of the Q of the circuit where $\delta\left(\frac{1}{Q}\right) = \eta\chi_e''$ where χ_e'' is the electric susceptibility of the material being sensed. A detailed discussion of the signal origin is given in Appendix A. Discontinuous flow is achieved with a burette where drops of liquid can be released at a well controled rate. The burette is mounted so that the liquid drops pass parallel to the coil plane at a distance of 5 mm from the coil. Figure 5.21 shows the typical signal obtained by passing drops of water at a distance of 5 mm from the coil where each spike corresponds to a water drop.

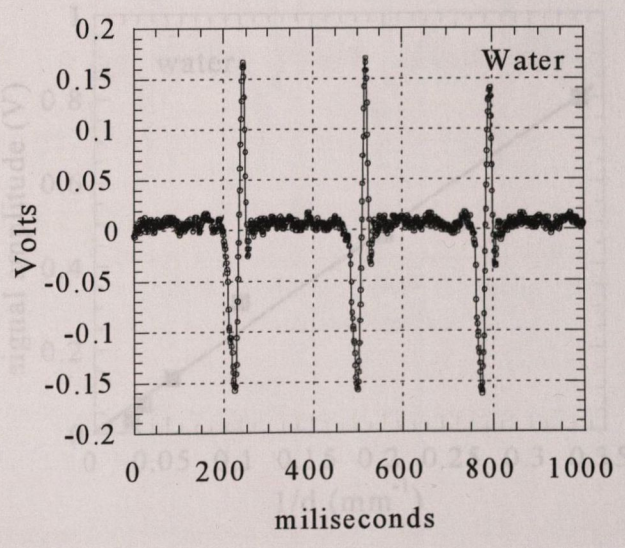


Figure 5.21. Signal obtained from water drops passing at 5 mm from the coil. Each peak corresponds to one drop.

In another experiment the dependence of the signal amplitude on the distace between the coil and the drops was studied where the signal amplitude is the distance in volts between maximum and minimum value of the signal. The results are summarised in Figure 5.22.

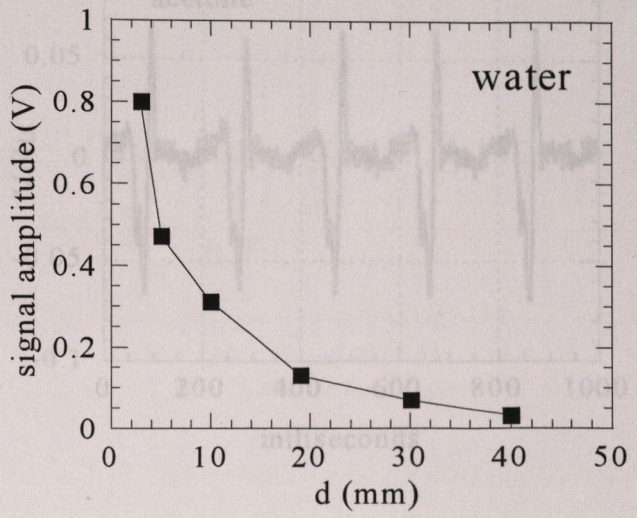


Figure 5.22. Signal amplitude measured as a function of distance.

The fall in amplitude is best fitted by a 1/d dependence shown in Figure 5.23.

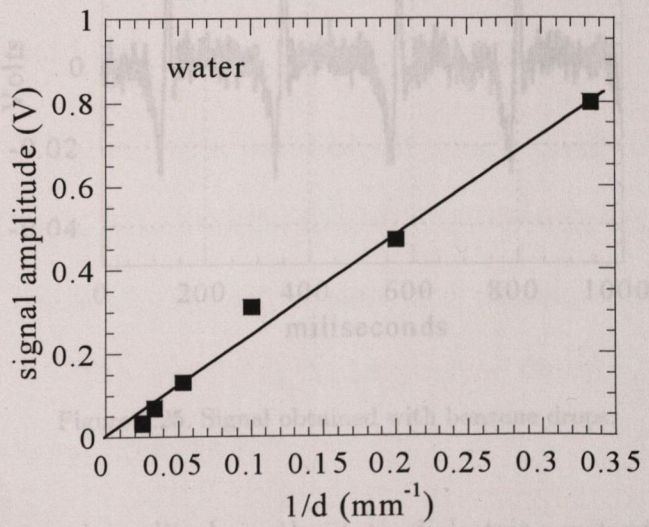


Figure 5.23. Signal amplitude as a function of the inverse of the distance between coil and watre drop.

The signal amplitude and shape was also studied for liquids with different dielectric constant.

The separation between the drops and the coil was 5 mm in all cases. Figures 5.24 and 5.25 shows the signal obtained for acetone and benzene.

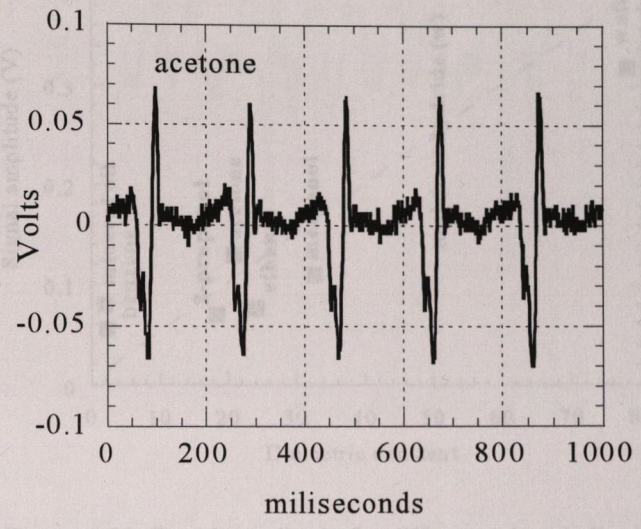


Figure 5.24. Signal obtained with acetone drops.

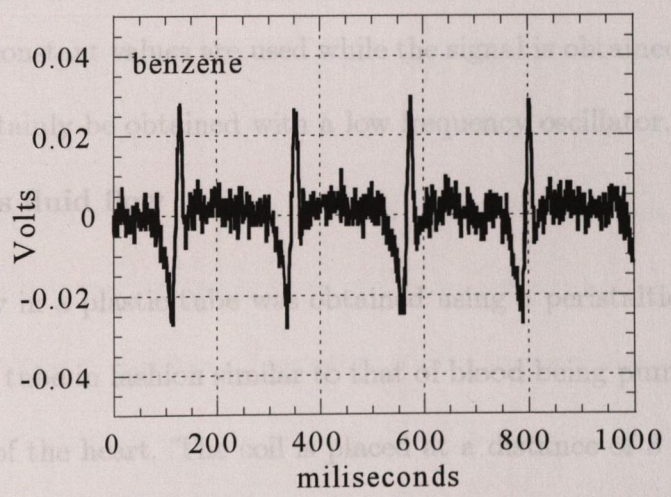


Figure 5.25. Signal obtained with benzene drops.

The dependence of the signal amplitude on the static dielectric constant of the liquids studied is plotted in Figure 5.26.

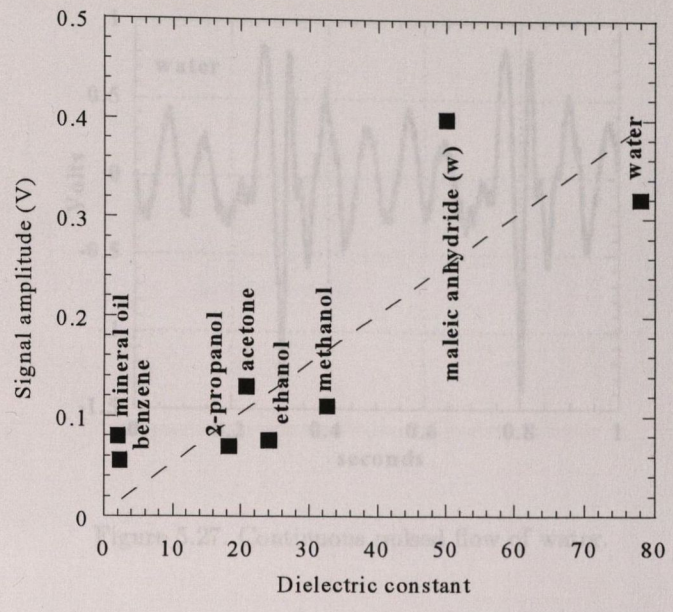


Figure 5.26. Signal amplitude for different ielectric liquids.

The dependence is roughly linear, but one should take in consideration the fact that low frequency dielectric constant values are used while the signal is obtained at 3 GHz. A better agreement would certainly be obtained with a low frequency oscillator.

5.3.3 Continuous fluid flow

Continuous fluid flow in a plastic tube was obtained using a peristaltic pump. The fluid is pumped through the tube in fashion similar to that of blood being pumped into the arteries by the contractions of the heart. The coil is placed at a distance of 3 mm from the plastic tube and the plane of the coil is parallel to the longitudinal direction of the tube. The flow of tap water gives the signal in Figure 5.27.

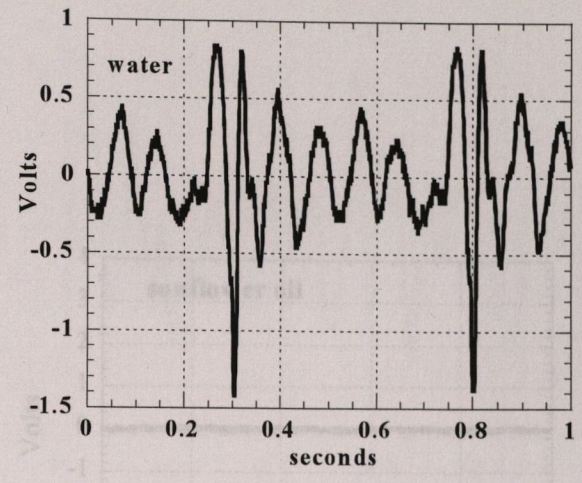


Figure 5.27. Continuous pulsed flow of water.

The signal for continuous flow is not as well defined as in the previous experiment but each negative peak on the oscilloscope trace corresponds to a pulse of liquid passing the coil and the measured frequency is the same as that of the pump.

This set up was used to analyse a mixture of different fluids. A beaker was filled with tap water and sunflower oil left to rest until full separation of the fluids was obtained. The first signal was obtained by pumping only sunflower oil through the tubes (top of Figure 5.28). When the input tube is moved to the bottom of the beaker so that water is allowed in, the signal in the central graph is obtained. The signal will be unstable for as long as the mixture of fluids is present in the tube. As the amount of oil decreases the signal slowly becomes more stable and the features of the third graph become progressively more clear until there is only water flowing in the tube. Another simple experiment can prove the ability of the sensor to detect a gas/liquid mixture. Figure 5.29 shows the signal obtained when a freshly open carbonated soft drink is passed in the plastic tube. At this stage the drink is rich in gas and the fluid in the tube is basicly a foam.

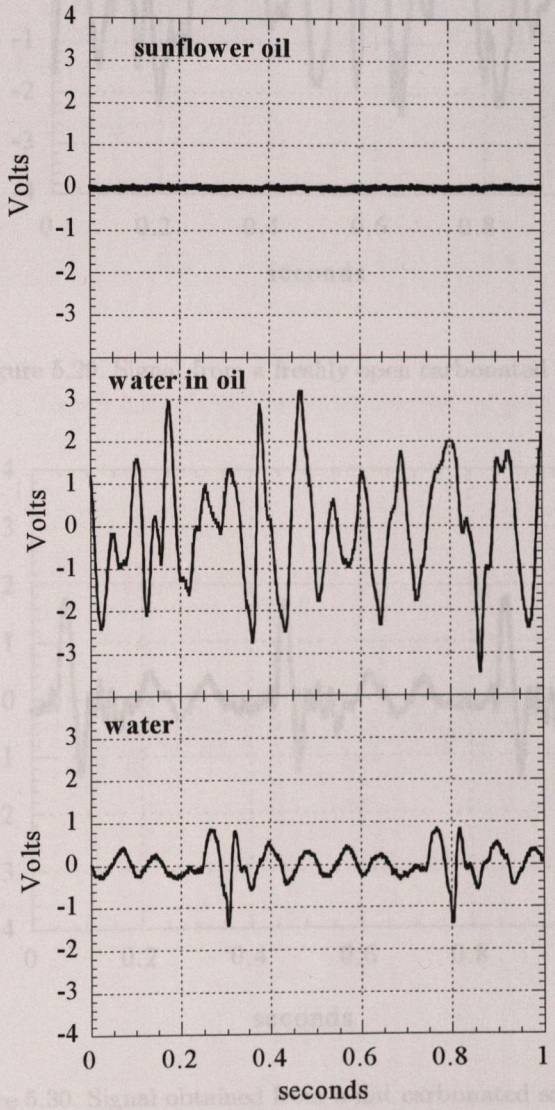


Figure 5.28. Signal obtained for sunflower oil (top), a mixture of oil and water (middle)and water (bottom).

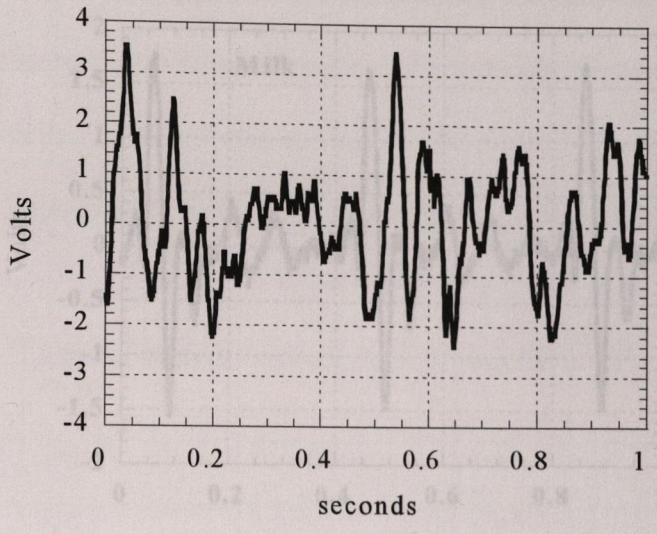


Figure 5.29. Signal from a freshly open carbonated drink.

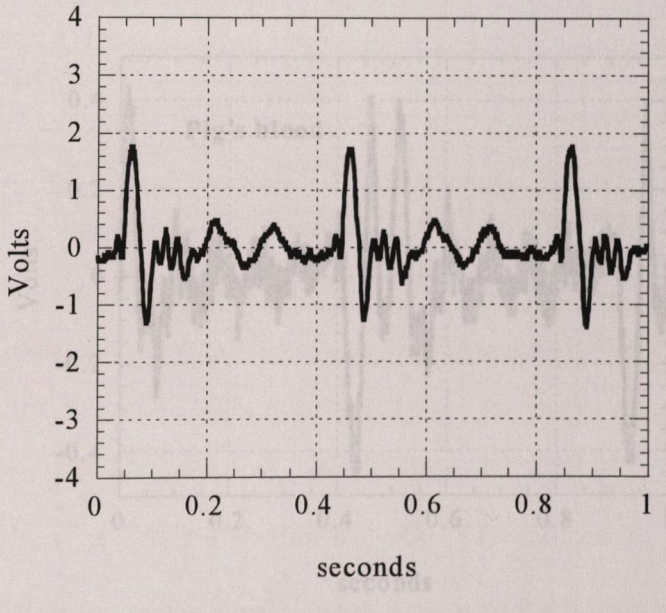


Figure 5.30. Signal obtained from a flat carbonated soft drink.

As the gas is released, the liquid phase becomes more predominant and the signal starts showing the features observed for water flow (Figure 5.30).

The device is also sensitive to biological fluids such as milk and blood as illustrated in Figures 5.31 and 5.32.

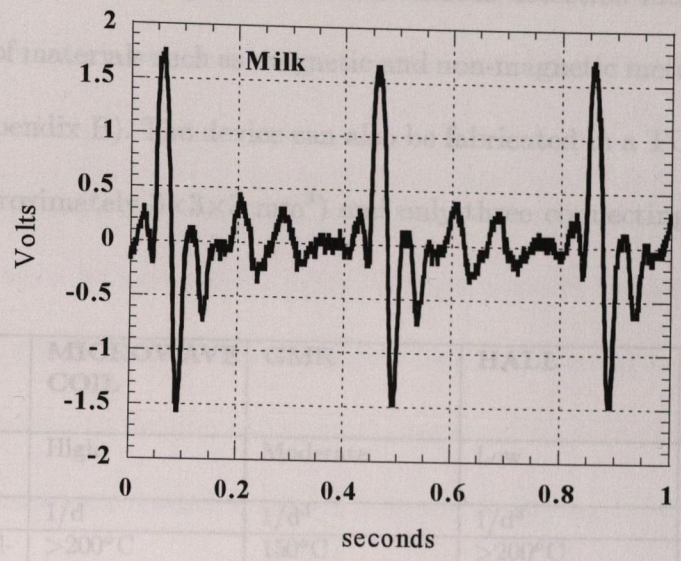


Figure 5.31. Signal for peristaltic flow of milk.

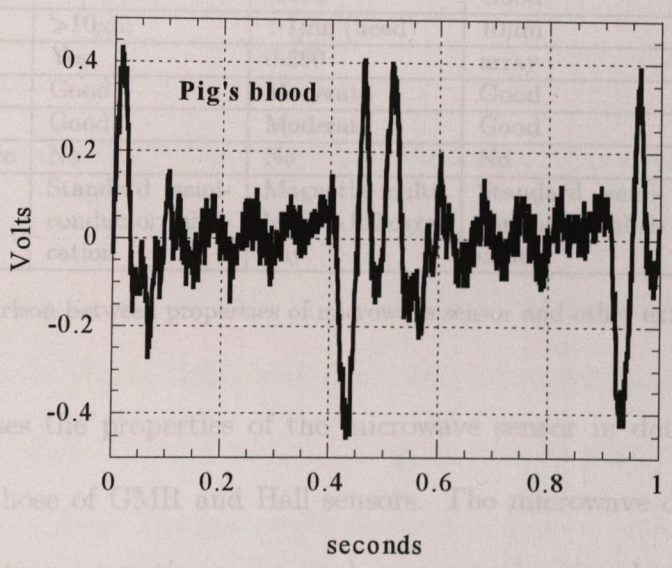


Figure 5.32. Peristaltic flow of pig's blood.

5.4 Discussion

The microwave sensor presented here, represents a new concept in position and motion sensing. Because the coil is sensitive to χ'' and χ''_e through a change in the quality factor,

it is a very versatile device that operates in simultaneous detection modes and is capable of detecting a variety of materials such as magnetic and non-magnetic metals, plastics, ceramics and liquids (see Appendix B). The device can also be fabricated in a TO18 chip with a small packaging size (approximately $3\times3\times3$ mm^3) and only three connecting leads: power, earth and output.

	MICROWAVE COIL	**GMR**	**HALL**	**VARIABLE RELUC-TANCE**
Signal/noise	High	Moderate	Low	Speed dependent
Sensitivity falloff	1/d	$1/d^3$	$1/d^3$	1/d
Temperature tolerance	>200°C	150°C	>200°C	>200°C
Biasing magnet	No	Yes	Yes	No
Size	On chip (no magnet)	Chip+magnet	Chip+magnet	Large
Life/ageing/failure	Good	Good	Good	Good
Spatial precision	>10μm	>1μm (head)	10μm	10μm
Position	Yes	0-360	array	No
Corrosion	Good	Moderate	Good	Good
Shock	Good	Moderate	Good	Good
Speed dependence	No	No	No	Yes
Manufacturing	Standard semiconductor fabrication	Magnetic multilayer + lithography	Standard semiconductor fabrication	Coil + magnet + magnetic circuit

Table8.Comparison between properties of microwave sensor and other existing technologies

The table summarises the properties of the microwave sensor in detection of mechanical parts compared to those of GMR and Hall sensors. The microwave device has some clear advantages over existing magnetic sensors such as a superior signal to noise ratio plus the ability to perform most of the functions available in existing devices. The high signal to noise ratio is an intrinsic characteristic of this oscillator that is not changed by the presence of an amplifier at the control circuit since the noise amplitude is multiplied by the same factor as the signal amplitude. To this we should add the possibility of reliable detection at distances between 2 and 20 mm allowing for more freedom in machine design. Furthermore,

it is compatible with the existing methods of production of semiconductor devices and it does not require a biasing magnet, which can lead to a considerable reduction in production cost. The main disadvantage of the microwave sensor is its inhability to sense the direction of rotation of the mechanical parts which can be easily overcome by an encoding configuration. Thornton et al. [19] have demonstrated a practical application in the automotive industry by modifying the distributor of a V8 Mercedes engine. A circuit similar to the one presented in this study (where instead of the flat coil a small copper wire solenoid is used) was installed in the distributor in order to control the ignition spark timing function. The control of this function can be switched between the common variable reluctance system and the high frequency sensor. The signal obtained from the latter is clearly superior due to its speed independence and sharp definition of the timing pulses.

We have also proved the ability of the sensor to detect liquids. Liquid sensing is desirable in any industrial, chemical, biological and medical contexts. In areas as diverse as meteorology, chemical processing, pharmaceutics, brewing, food processing, medical diagnosis, lubrication, oil extraction, hydroponics and agriculture it is desirable to sense and characterise liquid flows, including liquid mixtures, fluids with liquid or solid contaminants and slurries. Some examples were given above of the detection of liquids with diferent dielectric constants as well as flow inhomogeneities. The microwave sensor combines an imediate response to flow changes with a small device size and simplicity of operation.

A commonly used method for monitoring fluid flow is optical observation using single or multiple wavelenght sources and detectors, and based on absorption, reflection or scattering of the light. Wavelenghts commonly used range from ultraviolet to microwaves. The requirement for a source and a detector makes the devices prone to disalignment and contamination

by dirt and dust.

Devices for monitoring the percentage of water in oil (or water-cut) are often based on capacitance measurements. They consisted of two parallel metal plates inside the pipeline with the oil flowing between the two plates. Detection of water is made by measuring the changes in the capacitance of the plates. This is possible for the low water-cut regions where oil (an insulator) is the continuous phase in the fluid. However, for the high water-cut region, water (a conductor) is the continuous phase and in practice short-circuits the device so that no measurement can be considered reliable in this region. This is aggravated by the fact that in most applications the device has to deal with sea water which has an enhanced conductivity due to its high salinity.

Contactless sensors have the advantage that they can be mounted remotely from the liquid stream. Microwave detection is also used in an oscillator load pull configuration [22] which works by measuring the frequency variation at resonance of a high-frequency oscillator. However these devices have a very large size of approximately 8000 cm^3.

For discontinuous flow, the typical shape of the signal is shown in Figure 5.33a). The signal resembles the derivative of a maximum and its integral is shown in Figure 5.33b). Figure b) corresponds to the variation of the filling factor η as a drop of liquid passes the sensitive volume of the coil, and the signal amplitude is proportional to the dielectric constant of the fluid as shown in Figure 5.26. In other words the drop size (through η) scales with the dielectric constant, which can allow an effective monitoring of the drop mass. The detection mechanism in the case of continuous flow is not clearly understood yet. The detection of water in oil or oil in water is due to the difference in electric conductivity and permitivity of the two liquids as shown by equation (81) in Appendix B. The same considerations apply

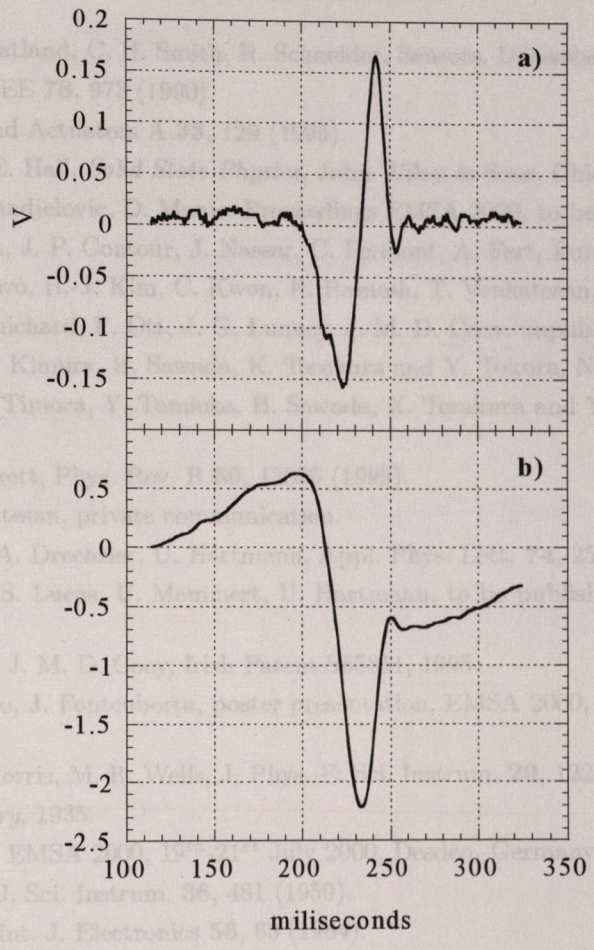


Figure 5.33. a) signal from a water drop, b) integral of the signal shown in a).

for the case of the gas/liquid mixture of Figure 5.29.

References

[1] M. J. Caruso, T. Bratland, C. H. Smith, R. Schneider, Sensors, December 1998.

[2] J. E. Lenz, Proc. IEEE **78**, 973 (1990).

[3] P. Ripka, Sensors and Actuators A **33**, 129 (1996).

[4] J. R. Hook and H. E. Hall, *Solid State Physics*, John Wiley & Sons, Chichester 1991.

[5] R. S. Popovic, Z. Randjelovic, D. Manic. Proceedings EMSA 2000, to be published.

[6] M. Viret, M. Drouet, J. P. Contour, J. Nassar, C. Fermont, A. Fert, Europhys. Lett. **39**, 545 (1997).

[7] J.-H. Park, E. Vescovo, H.-J. Kim, C. Kwon, R. Ramesh, T. Venkatesan, Nature **392**, 794 (1998).

[8] R. P. Borges, W. Guichard, F. Ott, J. G. Lunney, J. M. D. Coey, unpublished.

[9] K. I. Kobayashi , T. Kimura, H. Sawada, K. Terakura and Y. Tokura, Nature **395**, 677 (1998).

[10] K. I. Kobayashi, T. Timura, Y. Tomioka, H. Sawada, K. Terakura and Y. Tokura, Phys. Rev. B. **59**, 11159 (1999).

[11] R. Weht, W. E. Pickett, Phys. Rev. B **60**, 13006 (1999).

[12] Munuswamar Venkatesan, private communication.

[13] Y. Xu, V. Dworak, A. Drechsler, U. Hartmann, Appl. Phys. Lett. **74**, 2513 (1999).

[14] Y. Xu, V. Dworak, S. Lucas, U. Memmert, U. Hartmann, to be published in J. Phys. D: Applied Physics, 2000.

[15] M. Viret, L. Ranno, J. M. D. Coey, Irish Patent S65851, 1995.

[16] Ll. Balcells, E. Calvo, J. Fontcuberta, poster presentation, EMSA 2000, Dresden, Germany 19^{th}-21^{st} July 2000.

[17] J. F. Gregg, I. D. Morris, M. R. Wells, J. Phys. E: Sci. Instrum. **20**, 1223 (1987).

[18] *Wireless World Diary*, 1935.

[19] Poster presentation, EMSA 2000, 19^{th}-21^{st} July 2000, Desden, Germany.

[20] F. N. H. Robinson, J. Sci. Instrum. **36**, 481 (1959).

[21] F. N. H. Robinson, Int. J. Electronics **56**, 63 (1984).

[22] http://www.phasedynamics.com

Appendix A

Proof that $\delta\left(\frac{1}{Q}\right) = \eta\chi'' = \eta\chi''_e$

The quality factor of a circuit is given by

$$Q = \frac{\omega \times \text{stored energy}}{\text{rate of energy dissipation}} \tag{46}$$

For an LRC circuit as the one described above the rate of energy dissipation is given by $\frac{1}{2}RI_0^2$ and the stored energy is given by

$$\frac{1}{2}LI^2 + \frac{Q^2}{2C} = \frac{1}{2}LI_0^2 \sin^2 \omega t + \frac{1}{2C\omega^2} I_0^2 \cos^2 \omega t \tag{47}$$

where I_0 is the maximum current amplitude. The oscilation frequency in the LRC circuit is

$$\omega = \sqrt{\frac{1}{LC} - \frac{R^2}{4L^2}} \tag{48}$$

In the present case $R^2/4L^2 \sim 10^{14}$ and $1/LC \sim 10^{19}$ so that

$$\omega^2 = \frac{1}{LC} \tag{49}$$

and the stored energy becomes

$$\frac{1}{2}LI_0^2 \tag{50}$$

and the quality factor is given by

$$Q = \frac{\omega L}{R} \tag{51}$$

An inductor of inductance L_0 when embedded in a medium of relative permeability μ has its inductance changed to

$$L = \mu L_0 = (1 + \chi) L_0 \tag{52}$$

where χ is the magnetic susceptibility of the medium. This is also valid in the case where the coil is wound around a magnetic specimen, or in the case of the flat coil, when a magnetic specimen is placed in the proximity of the coil. Because in the two latter cases not all the magnetic field of the coil permeates the material, the inductance variation should include a normalising factor η, the filling factor, as

$$L = L_0(1 + \eta\chi) \tag{53}$$

The impedance of the coil can be written as

$$Z = i\omega L + R \tag{54}$$

where R is the resistance of the inductor. For a magnetic material in the vicinity of the coil this becomes

$$Z = i\omega L_0(1 + \eta\chi) + R \tag{55}$$

and writing χ in terms of its real and imaginary parts

$$\chi = \chi' - i\chi'' \tag{56}$$

and we get

$$Z = i\omega L_0(1 + \eta\chi') + \omega L_0\eta\chi'' + R \tag{57}$$

The imaginary part of the susceptibility has introduced a real term in the impedance. In other words, a magnetic specimen in the vicinity of the coil causes it to appear as a changed inductance in series with an increased resistance. The losses in the coil can be quantified in

terms of the quality factor Q defined as

$$Q = \frac{\omega L}{R} \tag{58}$$

If Q_0 is the natural quality factor of the coil, corresponding to an equivalent series resistance of

$$R = \frac{\omega L_0}{Q_0} \tag{59}$$

then, since the effect of the specimen is to add a further resistance δR

$$\delta R = \omega L_0 \eta \chi'' \tag{60}$$

we see that the inverse Q is increased by

$$\frac{1}{Q} = \frac{1}{Q_0} + \eta \chi'' \tag{61}$$

or

$$\delta \left(\frac{1}{Q} \right) = \eta \chi'' \tag{62}$$

If instead of the inductance we consider the capacitance of the circuit a similar result can be obtained. Here we do not refer to the capacitance of any specific component but the total capacitance of the circuit due to stray electric fields. An estimate of these electric fields between the two ends of the coil can be given by considering that each capacitor C drops approximately 6 V. The gap between them is approximately 2 mm so that the stray field is 3 kVm^{-1}. A capacitance C_0 is changed to

$$C = (1 + \eta \chi_e) C_0 \tag{63}$$

where χ_e is the electric susceptibility. By using the same treatment as above for the magnetic

susceptibility we find that the real component of the impedance of the circuit

$$Z = \frac{1}{i\omega C} + i\omega L + R \tag{64}$$

is changed by a a factor

$$\delta R = \frac{\eta \chi_e''}{\omega C_0} \tag{65}$$

so that

$$\delta\left(\frac{1}{Q}\right) = \frac{\delta R}{\omega L} = \frac{\eta \chi_e''}{\omega^2 L C_0} = \eta \chi_e'' \tag{66}$$

given that $\omega^2 = \frac{1}{LC_0}$.

Appendix B
Electromagnetic losses in a continuous medium

A simple analysis of Maxwell's equations will give an idea of the effect of the microwave electric and magnetic field on the material under observation. The four Maxwell equations are

$$\nabla \times \overrightarrow{H} = \frac{\partial \overrightarrow{D}}{\partial t} + \overrightarrow{j} \tag{67}$$

$$\nabla \times \overrightarrow{E} = -\frac{\partial \overrightarrow{B}}{\partial t} \tag{68}$$

$$\nabla . \overrightarrow{B} = 0 \tag{69}$$

$$\nabla . \overrightarrow{D} = \rho \tag{70}$$

where

$$\overrightarrow{j} = \sigma \overrightarrow{E} \tag{71}$$

$$\overrightarrow{D} = \varepsilon \overrightarrow{E} \tag{72}$$

$$\overrightarrow{B} = \mu \overrightarrow{H} \tag{73}$$

Here we consider the general case of plane waves in a material with conductivity σ. By applying the curl operator to both sides of equation (68) and using equation (67) we get

$$\nabla^2 \overrightarrow{E} = \varepsilon\mu \frac{\partial^2 \overrightarrow{E}}{\partial t^2} + \mu\sigma \frac{\partial \overrightarrow{E}}{\partial t} \tag{74}$$

An equation with exactly the same form can be obtained for $\overrightarrow{H}$. A general solution can be found for this equation but for simplicity we are going to consider the case of an electromag-

netic wave travelling parallel to the z axis so that all derivatives $(\partial/\partial x)$ and $(\partial/\partial y)$ vanish and both E_z and H_z are zero. This is the simple case of a purely transverse wave. Considering a plane polarized wave with $\overrightarrow{E}$ parallel to the x axis the field equations (67) and (68) reduce to

$$\frac{\partial E_x}{\partial z} = -\mu\left(\frac{\partial H_y}{\partial t}\right) \tag{75}$$

$$-\frac{\partial H_y}{\partial z} = \varepsilon\left(\frac{\partial E_x}{\partial t}\right) + \sigma E_x \tag{76}$$

Another simplification should be introduced by considering that the electromagnetic waves travel with a single frequency ω and E_x and H_y depend on time and position as

$$\exp\left[i\omega\left(t - \mathbf{n}z/c\right)\right] \tag{77}$$

where $\mathbf{n}$ is the complex refractive index and c the speed of light. The equations become

$$i\omega(\mathbf{n}/c)E_x = i\omega\mu H_y \tag{78}$$

$$i\omega(\mathbf{n}/c)H_y = (i\omega\varepsilon + \sigma)E_x \tag{79}$$

The intrinsic impedance of the medium, Z, is defined as E_x/H_y so that

$$Z = \left(\frac{\mu}{\varepsilon - i\sigma/\omega}\right)^{\frac{1}{2}} \tag{80}$$

The real part of Z is given by

$$Z_r = \frac{1}{\sqrt{2}}\left(\frac{1}{\varepsilon^2 + (\sigma/\omega)^2}\sqrt{(\mu\varepsilon)^2 + (\sigma\mu/\omega)^2} + \frac{\mu\varepsilon}{\varepsilon^2 + (\sigma/\omega)^2}\right)^{1/2} \tag{81}$$

The real part of the impedance introduces a decrease in the amplitude of the microwave, i.e. it is responsible for electromagnetic losses. This complex expression illustrates an important point about the device: the simultaneous modes of operations refered to above are not distinct and can not be separated, i. e., one can not make a device for detection of only

dielectric or magnetic materials since the losses depend only on the impedance of the medium. The electromagnetic losses are related to both the electric and magnetic susceptibilities since $\mu = 1 + \chi$ and $\varepsilon = 1 + \chi_e$.

Appendix C
Tuning the circuit

The process of finding the values for each circuit component is a trial and error one. The example below illustrates how it can be achieved for a particular application. The relevant circuit equations are

$$R \leqslant \frac{g_m}{\omega^2 \gamma^2} \tag{82}$$

and

$$\omega^2 = \frac{1}{LC^*} \tag{83}$$

where $1/C^* = 2/\gamma + 2/C$.

Suppose we need an application requiring a coil with 500 μm diameter and we want to keep the oscillation frequency at a value of $f = 3$ GHz. The inductance of a coil with this diameter is $L = 1$ nH. Using this value in equation (83) we get $C^* = 2.5$ pF. This value of the total capacitance can be obtained with $C = \gamma = 10$ pF. Substituting the value of γ in equation (82) we get $R \leqslant 0.125\ \Omega$.

The dimensions of the coil can now be calculated in order to match the desired resistance and writing

$$R = \rho \frac{l}{S} = \rho \frac{2\pi r}{wt} \tag{84}$$

where r is the radius of the coil, w is the width the coil track and t the thickness. If a copper coil is used, where $\rho = 1.67 \times 10^{-6}\ \Omega$cm, the resistance value above can be obtained with $t = 10\ \mu m$ and $w = 20\ \mu m$.

Chapter 6

Conclusions and further work

6.1 Conclusions

The aims of this study were (i) to study the magnetic and transport properties of ferromagnetic oxides $(La_{0.7}Sr_{0.3})MnO_3$ and A_2FeMoO_6 (A=Ca, Sr, Ba) in ceramic and thin film form, (ii) to optimise the physical, magnetic and transport properties of these materials and establish the feasibility of their use in the fabrication of electronic devices and (iii) fabricate a device based on one of these materials.

The manganese perovskite system has been extensively studied over the last ten years for ceramic, single crystal and thin film samples. In Chapter 3 we studied the properties of $(La_{0.7}Sr_{0.3})MnO_3$ thin films deposited by PLD and the search for the optimum deposition conditions of $(La_{0.7}Sr_{0.3})MnO_3$ films is described. There is a narrow window of values of the deposition parameters over which good quality films can be obtained. We found that the best films are obtained with a laser fluence of 2 Jcm^{-2}, oxygen background pressure of 0.3 mbar and a substrate temperature of 680°C. The films do not require annealing after deposition given that the film oxygen content is determined by the reaction of the ionic species in the plume with the background oxygen.

Once the deposition conditions were optimised we studied the isolated influence of substrate temperature on the structural, magnetic and transport properties of these films. We found that a deviation from the optimal substrate temperature of 680°C results in the formation of granular films. The granular nature of the films is confirmed by the x-ray patterns and by an increase in the film resistivity together with a large low field magnetoresistance.

We tried to address the problem of the decay of spin polarisation in LSMO based tunnel junctions by depositing a series of six thin films with thicknesses ranging from 1 to 60 nm. The films were deposited under the optimal deposition conditions described above. All films are well textured and the surface roughness in the range 0.5 to 1.5 nm. In particular, a 2 nm film shows a peak to valley roughness of 0.5 nm over an area of 1700×1800 nm proving that this film is essentially continuous. The 1 nm shows a similar roughness value and its continuity is not certain. The conductivity of the films decreases with decreasing thickness and it can be fitted with a two layer model considering a metallic bulk plus an insulating inteface layer with a total thickness of 4 nm. The electric dead layer may be associated with structural disorder at least at the level of the substrate interface due to the large lattice mismatch between LSMO and MgO. The electrical dead layer is likely to be also present at the free surface because the Mn atoms there are missing up to half their Mn-O neighbours, which will decrease the e_g bandwidth. Since the thickness of the interface layer is constant we could in fact see a decrease in the total conductance of the film as the thickness of the good layer decreases. This electric dead layer works as a tunnel barrier for spin dependent tunnelling across grain boundaries.

The magnetisation data obtained for these films can be interpreted by the existence of magnetic dead layers of equal thickness at both film interfaces. The total thickness of the magnetic dead layer is approximately 20 nm and it is formed of non colinear spins. Magnetic and electric dead layers combine to form three distinct areas in the thin films: a ferromagnetic and metallic bulk, a metallic magnetic dead layer responsible for the loss of polarisation of the carriers and an insulating magnetic dead layer that forms a tunneling barrier. This picture is in good agreement with results obtained by other authors and can explain the

poor performance of magnetic tunnel junctions based on LSMO. Besides the relatively low Curie temperature of this material, the existence of dead layers adds a further obstacle to its use in the area of spin electronics.

The need for half metals with high Curie temperatures has led to a surge of interest in the double perovskite family. We studied ceramics of double perovskites of the form A_2FeMoO_6 with A=Ca, Sr and Ba. The preparation of samples with different compositions under the same conditions gives rise to very different microstructures. This is reflected in the different resistivity and magnetoresistance behaviour of each sample. There is an increase of the magnetoresistance with resistivity. The room temperature resistivity value varies by five orders of magnitude between 1 mΩ cm for Ca_2FeMoO_6 and 4.5×10^5 mΩ cm for Sr_2FeMoO_6. The Ca_2FeMoO_6 bulk sample shows no magnetoresistance at either room temperature or 77 K. Ba and Sr compounds with much higher resistivities show magnetoresistance values of 13 % and 16 % respectively at room temperature and 1.2 T. Furthermore, the Sr_2FeMoO_6 ceramic exhibits a 1 % MR at room temperature in only 20 mT. Magnetoresistance was also measured in cold pressed powders of the Ca and Sr compounds. The MR increases (decreases) compared to that of the bulk ceramics if the resistivity of the powder is higher (lower) that the bulk resistivity.

Magnetisation curves at 5 K show that none of the compounds reaches the full saturation value of 4 μ_B/f.u. The magnetisation values of 3.63, 3.51 and 3.85 μ_B/f.u. for the Ca, Sr and Ba compounds are in good agreement with the 6, 7 and 2 % anti-site defect concentration deduced from Mössbauer measurements on the the same samples.

Thin films of Sr_2FeMoO_6 were fabricated by PLD. The formation of a good phase requires deposition in vacuum and high substrate temperatures. Good quality films were obtained

with a fluence of 2 Jcm^{-2}, a pressure of 10^{-6} mbar and a substrate temperature of 950°C. Deposited films of Sr_2FeMoO_6 on $SrTiO_3$ (100) substrates that have (220) orientation to mimic the cubic structure of the substrate and minimise lattice mismatch. For films deposited at a substrate temperature of 900 and 950°C the resistivity decreases with decreasing temperature to a minimum at around 100 K after which it increases to values similar to room temperature. The film deposited at 770°C shows semiconducting behaviour. No magnetoresistance could be measured in any of the films at either 77 K or room temperature which suggests few grain boundaries. This is the expected behaviour for a good quality crystalline film since the range of temperature in which magnetoresistance is measured is well below T_C where there is little spin fluctuations. The saturation magnetisation of films deposited at 900 and 950°C is 3.5 μ_B/f.u. at 20 K.

Thin films of Sr_2FeMoO_6 where also deposited on MgO substrates using the same conditions described above for films deposited on $SrTiO_3$. The magnetic properties are poor for the range of deposition conditions studied with maximum saturation values of only 2.4 μ_B/f.u. Furthermore, the films with best magnetisation values show large L-shaped holes on the surface which represent a serious obstacle to the fabrication of multilayers necessary for most device applications. Good quality films deposited on MgO might require higher deposition temperatures than 950°C.

SFMO thin films are extremely sensitive to water or solvents which creates difficulties for any patterning procedure. This can be overcome by depositing a thin cap layer of gold to protect the material from chemical attack. Films with a cap layer and etched by ion beam milling show the same resistance behaviour as before etching.

A new type of microwave position and motion sensor was invented and described in Chapter

5 combining the use of ferromagnetic oxides with microwave electronics. Initially thought to make use of the narrow hysteresis loop of LSMO, it was found that the circuit is capable of performing the detection function on its own. Detection takes place when an object enters a sensitive volume around the coil where magnetic and electric fields are present. In a similar implementation to the one described in this work, it was shown that the use of a LSMO bulk ceramic can indeed enhance the output signal when detecting magnetic objects.

The detection is based on a change in the quality factor of a single turn flat coil patterned on an LSMO thin film. The sensitivity to changes in Q makes the device very versatile. Here we proved its capability to monitor the position and angular velocity of mechanical parts made of magnetic and non magnetic metals as well as plastics. The device is also capable of detecting fluid flow where the output signal is proportional to the dielectric constant of the liquid. We proved its ability to detect continuous and discontinuous flow of a variety of liquids such as water, acetone, milk and blood.

This type of device offer some more advantages over other types of magnetic sensors in that it has a very high signal to noise ratio, it is compatible with the fabrication standards of the semiconductor industry and it does not require a biasing magnet.

6.2 Suggestions for further work

i) More systematic studies have to be undertaken in order to fully understand the properties of double perovskites. The influence of B cation anti-site disorder could be studied by growing and characterising single crystals with different degrees of cation disorder. The influence of the microstructure could also be studied by synthesis and characterisation of a batch of ceramic samples with different grain sizes.

ii) Systematic studies of the magnetic properties as a function of composition and stoichiom-

etry are necessary. This could be achieved by progressive substitution by Mn, Cr or Ni at the Fe site and Re or W at the Mo site. Sr_2CrMoO_6 and Ca_2FeReO_6 have T_C of 473 K and 530 K respectively but both compounds are insulating.

iii) The existence of magnetic or electric dead layers in double perovskite thin films should be checked by neutron diffraction or using the method presented in Chapter 3 for LSMO thin films.

iv) A basic requirement for device application of any material at industrial level is its compatibility with silicon and therefore growth of good quality SFMO films on silicon substrates should be attempted. The lattice parameter of silicon is $a = 5.4305$Å and the resulting lattice mismatch with the lattice parameter $a = 5.573$Å of SFMO is only 2.6%.

v) Magnetic tunnel junctions should be fabricated using SFMO as the junction electrodes. The deposition of an oxide tunnelling barrier could be a problem given the impossibility of obtaining the SFMO phase in the presence of oxygen. It should be possible to obtain a good tunnelling barrier by vacuum deposition of Al over the first electrode followed by a well controlled oxidation until Al_2O_3 is obtained. Once this is obtained the second SFMO electrode can be deposited in vacuum.

vi) The device shown here should be carefully tested for oil and water emulsions with varying percentages of both liquids as well as slurries.

vii) Scale down the device for detection of small particles in liquids. Develop some of the concepts presented in the patent such as a linear integrated array for monitoring the concentration of solid impurities in a fluid.

List of Publications

- Field induced transition in the paramagnetic state of $(Sm_{0.65}Sr_{0.35})MnO_3$ associated with magnetic clusters
  R. P. Borges, F. Ott, R. M. Thomas, V. Skumriev, J. M. D. Coey, J. I. Arnaudas, L. Ranno, Phys. Rev B **60**, 12847 (1999).

- Magnetic properties of the double perovskites A_2FeMoO_6, A= Ca, Sr, Ba
  R. P. Borges, R. M. Thomas, C. Cullinan, J. M. D. Coey, R. Suryanarayanan, J. Phys.: Condens. Matter **11**, L445 (1999).

- Ferrimagnetic order in Ca_2FeMoO_6
  L. Pinsard-Gaudart, R. Surynarayanan, A. Revcolevschi, J. Rodriguez-Carvajal, J.-M. Greneche, P. A. I. Smith, R. M. Thomas, R. P. Borges, J. M. D. Coey, J. Appl. Phys. **87**, 7118 (2000).

- Interface magnetism of $(La_{0.7}Sr_{0.3})MnO_3$ thin films studied by neutron reflectometry
  F. Ott, M. Viret, R. P. Borges, R. Lyonnet, E. Jacquet, C. Fermon, J.-P. Contour, J. Magn. Magn. Mater. **211**, 200 (2000).

- A versatile motion sensor
  R. P. Borges, M. Bari, J. M. D. Coey, M. Thornton, J. F. Gregg, W. Allen, to be published in the Proceedings of the 3^{rd} European Conference on Magnetic Sensors and Actuators.

- Magnetic and electric dead layers in $(La_{0.7}Sr_{0.3})MnO_3$ thin films
  R. P. Borges, W. Hasch, J. G. Lunney, J. M. D. Coey, F. Ott, submitted to J. Appl. Phys.

- Liquid sensor, J. M. D. Coey, J. F. Gregg, R. P. Borges, Irish patent S20000674